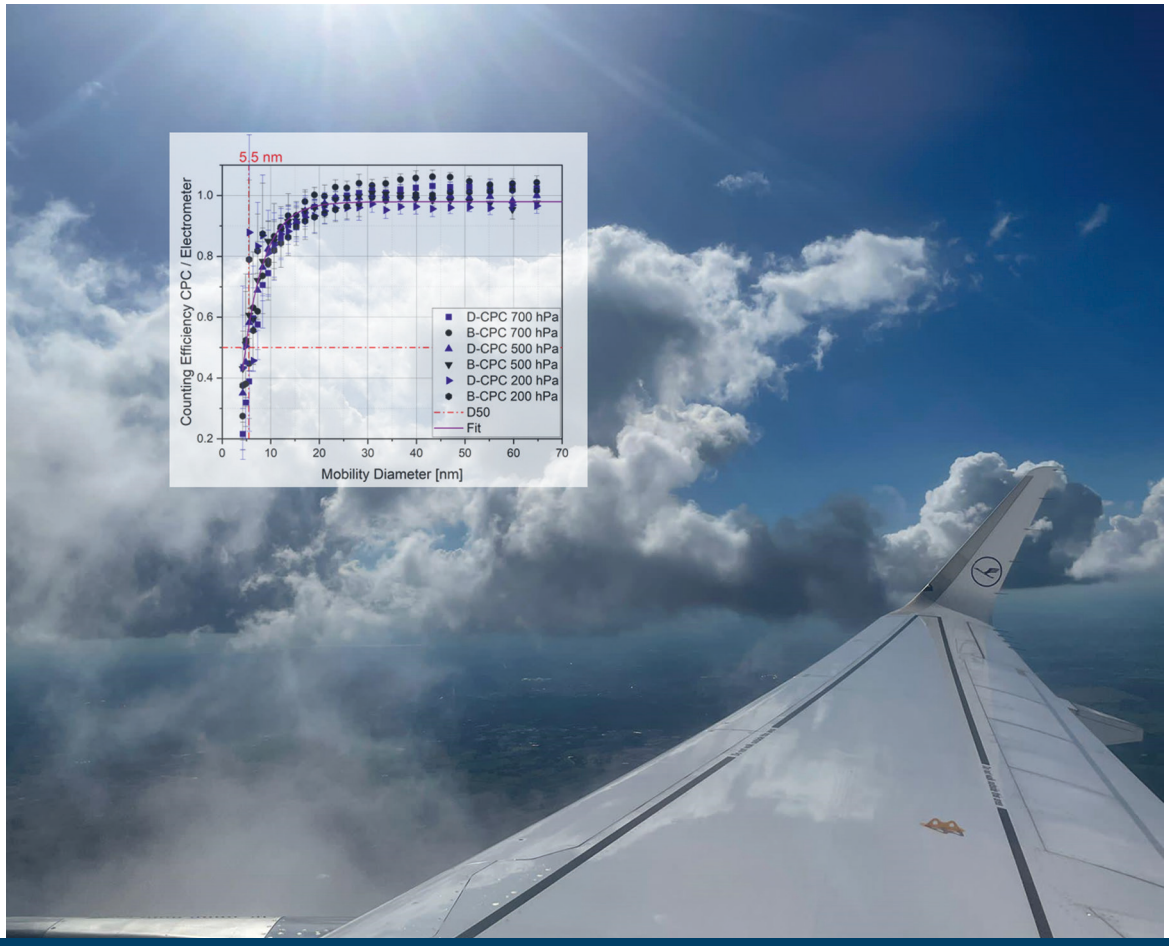

On a multi-spectral method for measuring aerosol properties, suitable for operation on iagos passenger aircraft

Patrick Weber

Energie & Umwelt / Energy & Environment
Band / Volume 625
ISBN 978-3-95806-746-2

Mitglied der Helmholtz-Gemeinschaft

JÜLICH
Forschungszentrum

Schriften des Forschungszentrums Jülich
Reihe Energie & Umwelt / Energy & Environment Band / Volume 625

Forschungszentrum Jülich GmbH
Institut für Energie- und Klimaforschung (IEK)
Troposphäre (IEK-8)

On a multi-spectral method for measuring aerosol properties, suitable for operation on iagos passenger aircraft

Patrick Weber

Schriften des Forschungszentrums Jülich
Reihe Energie & Umwelt / Energy & Environment Band / Volume 625

ISSN 1866-1793 ISBN 978-3-95806-746-2

Bibliografische Information der Deutschen Nationalbibliothek.
Die Deutsche Nationalbibliothek verzeichnet diese Publikation in der
Deutschen Nationalbibliografie; detaillierte Bibliografische Daten
sind im Internet über http://dnb.d-nb.de abrufbar.

Herausgeber und Vertrieb:	Forschungszentrum Jülich GmbH Zentralbibliothek, Verlag 52425 Jülich Tel.: +49 2461 61-5368 Fax: +49 2461 61-6103 zb-publikation@fz-juelich.de www.fz-juelich.de/zb
Umschlaggestaltung:	Grafische Medien, Forschungszentrum Jülich GmbH
Druck:	Grafische Medien, Forschungszentrum Jülich GmbH
Copyright:	Forschungszentrum Jülich 2024

Schriften des Forschungszentrums Jülich
Reihe Energie & Umwelt / Energy & Environment, Band / Volume 625

D 468 (Diss. Wuppertal, Univ., 2023)

ISSN 1866-1793
ISBN 978-3-95806-746-2

Vollständig frei verfügbar über das Publikationsportal des Forschungszentrums Jülich (JuSER)
unter www.fz-juelich.de/zb/openaccess.

This is an Open Access publication distributed under the terms of the Creative Commons Attribution License 4.0,
which permits unrestricted use, distribution, and reproduction in any medium, provided the original work is properly cited.

Acknowledgements

First and foremost, I would like to thank Prof. Dr. Andreas Petzold for the warm welcome into his working group and for making my dissertation possible. I would also like to thank Prof. Dr. Peter Wiesen for the uncomplicated support during my doctoral thesis.

Next, my thanks go to Dr. Ulrich Bundke, who sometimes only had to enter the room for the elimination of technical problems and supervised and helped on many occasions.

A big thank you goes to Dr. Oliver Bischof for reading and correcting every first draft of papers, abstracts and more.

I would especially like to thank Jannik Schmitt and Marcel Berg for their help in the lab. Without various tips and great teamwork on the projects, many things would not have run so smoothly.

I would like to thank the entire working group once again for their welcome and for the fact that everyone, without exception, responded in a friendly and competent manner to my countless concerns.

I would also like to express my heartfelt thanks to my colleagues Niklas and Benedikt, as well as Marie, Isa, Jacky and Tobi from cologne. Years of friendship with countless game nights have brightened my days.

A deep thanks go to my group of friends Nina, Günther, Bene, Anny and Stefan, that filled many days and hours during lock-down periods with joy.

A big thank you goes to those who support my countless hobbies. The Group of the Red Lily for allowing me to put on my shining medieval armour, Dominik for smithing lessons, Simon and Nils to put my 3D-Printer on good use and Michelle to be my Co-Chair at the Journal Club

Deepest thanks and best wishes for recovery go to my fiancée Alice, as she was able to proofread my thesis again with greatest of efforts.

Finally, I thank my grand-parents Else and Manfred and I would especially like to thank my parents Cathleen and Hartmut, who made my studies possible. They supported me at all times and made every additional burden easier for me.

Abstract

The very need for a ground truth for satellite validations and continuous monitoring of essential climate variables are the motivation of this thesis. An extensive set of property information is needed to improve climate modelling and air quality observation. To address this need, we present a new instrument package for the European research infrastructure IAGOS (In-service Aircraft for a Global Observing System). This new instrument will deliver long-term observations of aerosol optical properties and NO2 as proxies for air pollution, conducted globally on board of instrumented passenger aircraft of the IAGOS fleet.

The new instrument package is designed and optimised for the environmental conditions on board of commercial aircraft cruising in the upper-troposphere-lower-stratosphere (UTLS) region. The operation onboard commercial aircraft requires that the instruments must operate unattended reliably for at least three months and must comply to strict safety requirements. The new instrument package is equipped with the following devices: Four different CAPS (Cavity Attenuated Phase Shift) tubes measure aerosol light extinction at 630 nm and 450 nm wavelength, as well as nitrogen dioxide. One of the CAPS PMex tubes is used for permanent baseline monitoring for NO2 and PM measurements. A modified POPS (Portable Optical Particle Spectrometer) measures aerosol particle number concentration and size distribution for particle diameters ranging from 125 nm to 4 µm. A water-based condensation particle counter (CPC) measures total aerosol particle number concentration.

Continuous developments, improvements and discoveries are the foundation of research. In this thesis, an aerosol optical line was set up to produce aerosol of well-characterised properties as a reference system for aerosol instruments that rely on the aerosol interaction with visible light. By using this line during an extensive instrument evaluation study, the uncertainties for a combined set of instruments measuring aerosol extensive properties and the resulting measurement accuracy for aerosol intensive properties were qualified for a large assembly of aerosol mixtures.

Improving a commercially available water-based condensation particle counter for operation under extreme conditions was a second major achievement of this thesis. The improvement consists of enlarging the operation range of this water-based CPC to pressure levels down to 200 hPa as a requirement for using this particle counter in aircraft-based measurements. This modification was later implemented by the manufacturer in a new instrument product.

Another significant improvement of the operation of condensation particle counters was achieved by introducing Dimethylsulfoxide (DMSO) as a safe working fluid substitute for alcohol-based condensation particle counters. With this new working fluid, the range for originally condensation particle counters are enlarged since it is now safe to use in working environment with strict safety restrictions and even more use cases can be achieved when this substance is mixed with water.

The thesis concludes with the full characterisation of the IAGOS Air Quality instrument which is now ready for certification for operation on commercial passenger aircraft in the framework of IAGOS.

Table of Contents

1 State of intent and work 6
2 List of Contributions to the Scientific Community 7
3 Table of Nomenclature 9
4 Introduction 12
5 Background Knowledge 15
5.1 Aerosol Properties 16
5.1.1 Aerosol Number Concentration and Size Distribution 17
5.1.2 Mechanical Movement of Particles 18
5.2 Aerosol Optical Properties 19
5.2.1 Extensive Aerosol Optical Properties 20
5.2.2 Intensive Aerosol Optical Properties 21
5.3 Aerosol Measurement Techniques 23
5.3.1 Instruments for Particle Counting 24
5.3.2 Instruments for Particle Size Distribution Measurement 25
5.3.3 Instruments for Aerosol Optical Properties Measurements 29
5.4 Nitrogen dioxide 32
6 Air Quality Instrument - Instrument Package 2E 33
7 Qualification of the CAPS Instrument 37
7.1 Aerosol Optical Properties Calibration Set-up 39
7.1.1 Background and used techniques 39
7.1.2 Experimental Approach on Aerosol Optical Properties 40
7.1.3 Optical Instruments and Uncertainties 41
7.1.4 Aerosol Generation for Aerosol Optical Property Measurements 42
7.1.5 Data Treatment, Instrument Corrections and Calibrations 43
7.1.6 Aerosol Optical Property Measurements 45
7.1.7 Summary on uncertainty measurements for aerosol optical properties 63
7.2 CAPS characteristics and LOD estimation 65
7.2.1 Intercomparison Campaign for CAPS NO2 67
8 Flight Simulation Test Stand 68
8.1 FCE Data treatment 69
8.2 Characterisation of the MAGIC CPC 72
8.2.1 Methods and Test-Set-up for CPC low Pressure Calibration 73
8.2.2 Optimisation of pressure dependent control variables for Laser Power and Detector 75
8.2.3 MAGIC low-pressure application summary and recommendations 84
8.3 Particle loss considerations 85
8.4 Portable Optical Particle Spectrometer 86

9 A new Working fluid substituting Butanol 91
9.1 Dimethyl Sulfoxide as A New Working Fluid 92
9.1.1 Introduction to CPC Working Fluid Characteristics 93
9.1.2 DMSO Droplet Size 96
9.1.3 Summary and Results of CPC measurements using DMSO 97
9.1.4 Precautions for using DMSO as a Working Fluid 102
9.1.5 DMSO as a suitable working fluid for low pressure applications 104
10 Conclusions and Outlook 105
11 List of Tables and Figures 110
12 References 115

1 State of intent and work

To my readers, you will experience the condensed matter of over three years of my collected knowledge on a fascinating topic. The journey will take you from the very basics you shall know about aerosols and how to measure them, to the performance of an Instrument Package that combines all of it. We will start with a general overview of aerosols and their interaction with Earth's climate. You will read the key phrases of the recent IPCC report and summaries of state-of-the-art scientific papers. You get an impression of an ongoing research infrastructure with its methods and products. After that introduction is settled, the structure of this work continues with background information about aerosols. Going more into detail, you get an impression of aerosol characteristics, and measurement techniques. Even though there is much more about them, we will focus on the size distribution, number concentration and their interaction with light at a specific wavelength. You learn the requirements for low-pressure applications and solutions for various obstacles we accrued on the way. After that, you get to know the calibration set-up for the instruments and finally, a summit of this work, you read about the performance of the individual devices. We conclude this work with an outlook for future work and the products this package will deliver.

Parts of the laboratory work, machine conversions or programme installations were only possible thanks to the close cooperation within the working group. For this reason, the general "we" is often used in this thesis. Explicit mention of the persons is made in the acknowledgements, but also in the list of co-authors for corresponding publications.

2 List of Contributions to the Scientific Community

Parts of this work were already published in journal articles, conference talks, posters, and other forms of publication.

Paper:

Bischof, O.F., **Weber, P**., Bundke, U. Petzold, A and Kiendler-Schaar, A.: Characterization of the Miniaturized Inverted Flame Burner as a Combustion Source to Generate a Nanoparticle Calibration Aerosol. *Emiss. Control Sci. Technol.* **6**, 37–46 (2020). https://doi.org/10.1007/s40825-019-00147-w

Weber, P., Petzold, A., Bischof, O. F., Fischer, B., Berg, M., Freedman, A., Onasch, T. B., and Bundke, U.: Relative errors in derived multi-wavelength intensive aerosol optical properties using cavity attenuated phase shift single-scattering albedo monitors, a nephelometer, and tricolour absorption photometer measurements, Atmos. Meas. Tech., 15, 3279–3296, https://doi.org/10.5194/amt-15-3279-2022, 2022.

Weber, P., Bischof, O. F., Fischer, B., Berg, M., Hering, S., Spielman, S., Lewis, G., Petzold, A., and Bundke, U.: Characterisation of a self-sustained, water-based condensation particle counter for aircraft cruising pressure level operation, Atmos. Meas. Tech., 16, 3505–3514, https://doi.org/10.5194/amt-16-3505-2023, 2023.

Weber, P., Bischof, O. F., Fischer, B., Berg, M., Schmitt, J., Steiner, G., Keck, L., Petzold, A., and Bundke, U.: A new working fluid for condensation particle counters for use in sensitive working environments, Aerosol Research, 1, 1–12, https://doi.org/10.5194/ar-1-1-2023, 2023.

Conference contributions

ICCPA 2019 (International Conference of carbonaceous particles in the atmosphere): Assessing Multi-Spectral Measurement Methods for Aerosol Optical Properties by an Extensive Closure Study for Different Aerosol Types; **P. Weber**, U. Bundke, O. F. Bischof, B. Fischer, M. Berg, A. Petzold; Poster presented by P. Weber

EAC 2019 (European Aerosol Conference) Goteborg: Multi-spectral aerosol optical properties of different types of light absorbing and light scattering aerosols; **P. Weber**, U. Bundke, O. F. Bischof, B. Fischer, M. Berg, A. Petzold; Oral Presentation presented by A. Petzold

EAC 2020 (European Aerosol Conference) Aachen: Adaption of a portable optical particle counter for aircraft measurements; B. Fischer, **P. Weber**, U. Bundke, O. F. Bischof, R.S. Gao, A. Petzold; Oral Presentation presented by P. Weber

Cambridge Particle Meeting 2021: On the accuracy of multi-wavelength intensive aerosol optical properties; **P. Weber**, U. Bundke, O. F. Bischof, M. Berg, A. Freedman, T. Onasch, A. Petzold; Oral Presentation presented by P. Weber

EAC 2021 UK: On the accuracy of multi-wavelength intensive aerosol optical properties – A Closure Study; **P. Weber**, U. Bundke, O. F. Bischof, M. Berg, A. Freedman, T. Onasch, A. Petzold; Oral Presentation presented by P. Weber

IAC 2022 (International Aerosol Conference) Athens: A First Laboratory Characterization of the Air Quality Package for airborne observations on passenger aircraft; **P. Weber**, A. Petzold, O. F. Bischof, J. Schmitt, M. Berg, B. Fischer, A. Freedman, T. Onasch, R.S. Gao, U. Bundke; Poster presented by P. Weber

Nanoparticle Conference 2023 ETH Zurich: A New Working Fluid for Condensation Particle Counters with Proprietary Benefits; **P. Weber**, O. F. Bischof, B. Fischer, M. Berg, J. Schmitt, G. Steiner, L. Keck, A. Petzold, and U. Bundke; Oral Presentation presented by P. Weber

EAC 2023 Malaga: A new working fluid for condensation particle counters at various pressure conditions; **P. Weber**, O.F. Bischof, B. Fischer, M. Berg, J. Schmitt, G. Steiner, L. Keck, A. Petzold, U. Bundke; Oral Presentation presented by P. Weber

Pending Application

P. Weber and U. Bundke: Nutzung von nicht brennbaren und nicht toxischen Sulfoxiden oder […] zur Vergrößerung von Aerosolpartikeln: G69610 / PT 0.3349

3 Table of Nomenclature

Constants and Symbols

$C_C(D_P)$	Slip Correction Factor
C_c	Cunningham correction factor
D_P	mobility equivalent size of the particle
F	Force
I	Light intensity
I_0	Incident light intensity
Q_A	Aerosol flow
Q_{Sh}	Sheath Flow
Q_{abs}	Absorption efficiency
Q_{scat}	Scattering efficiency
d_g	Geometric standard deviation
d_k	Kelvin diameter
d_s	Particle / droplet diameter
e_0	Elementary charge
n_i	Number of elementary charges on particle
p	Vapour Pressure
p_s	Saturated vapour pressure
r_a	Outer radius
r_i	Inner Radius
σ_R	Rayleigh scattering cross-section
σ_{a_gas}	Light absorption of a span gas
σ_{ap}	Light absorption coefficient on particles
σ_{ep}	Light extinction coefficient on particles
σ_{ext}	Light extinction coefficient
σ_l	Surface tension of a liquid
σ_{scat}	Light scattering coefficient
σ_{sp}	Light scattering coefficient on particles
σ_{sp_gas}	Light scattering coefficient of a span gas
k	Imaginary refractive index
m	Complex refractive index
n	Real refractive index
x	Size parameter
ξ	Diffusion coefficient
χ	mean free path length
A	Area
M	Molecular weight
N	Number
R	General gas constant
T	Temperature
U	Voltage
V	Volume
Z	Electronical mobility
dp	Particle diameter
$\vec{d}p$	Arithmetic mean diameter
f_a	Air flow rate
f	Frequency
i	Number of molecules
l	Length of a tube
v	Velocity of the particle
δ	Density
η	Viscosity
λ	Wavelength of light
μ	diffusion parameter
σ	Standard Deviation
φ	Phase

Abbreviations

AAE	Absorption Ångström exponent
ACTRIS	Aerosol Clouds and Trace Gases Research Infrastructure
AQ	Aquadag
AS	Ammonium sulphate
BC	Carbon Black
BIPM	Bureau International des Poids et Mesures
CAPS PMex	Cavity attenuated phase shift Particle light extinction Monitor
CLAP	Continuous Light Absorption Photometer
CLAW	Charlson; Lovelock; Andreae; Warren (Authors)
CLD	Chemiluminescence detection
CMD	Count Median Diameter
CMIP	Coupled Model Intercomparison Project
CO	Carbon monoxide
CO_2	Carbon dioxide
CPC	Condensation Particle Counter
DM	Differnential Method
DMA	Differential Mobility Analyser
DMSO	Dimethyl Sulfoxide
DWD	Deutsche Wetterdienst
EAE	Extinction Ångström exponent
ECV	Essential climate variables
EPA	Environmental Protection Agency
EQ	Equation
ERF	effective radiative forcing
ESA	European Space Agency
FCE	Faraday cup electrometer
GHG	Green House Gasses
GHS	Globally harmonized system
GSAT	Global mean surface air temperature
HEPA	High-efficiency particle absorbing
IAGOS	In-service Aircraft for a Global Observing System
IPCC	Intergovernmental Panel on Climate Change

Laser	Light amplification by stimulated emission of radiation
LED	Light emitting diode
Lidar	Light imaging, detection and ranging
MAAP	Multi-Angle Absorption Photometer
MAGIC	Moderated Aerosol Growth with Internal water Cycling
MB	Magic Black
MFC	Mass flow controller
NaCl	Sodium Chloride
NO_2	Nitrogen dioxide
NOAA	National oceanic and atmospheric administration
O_3	Ozone
OPC	Optical particle counter
PDF	probability density function
PID	proportional-integral-derivate controller
PM	Particulate Matter
PMT	Photomultiplier tube
POPS	Portable optical particle spectrometer
PSAP	Particle Soot Absorption Photometer
Q	Efficiencies
SAE	Scattering Ångström exponent
SMPS	Scanning mobility particle sizer
SO_2	Sulfur dioxide
SSA	Single Scattering Albedo
TAP	Tricolor Absorption Photometer
VOC	Volatile organic compounds

4 Introduction

Aerosol is an artificial word with the ancient Greek word for air and the Latin word for solution composed together. This indicates its physical appearance, as it describes particle matter being suspended in the medium air. Usually, those particles can be purely liquid, solid, or a mixture of both and are in size range of a few nanometres to several hundred micrometres. Aerosols got more public attention with the start of the covid pandemic and the realisation of possible infection ways via aerosol transmission [1]. An essential step in education and information to the general public was done by the Gesellschaft der Aerosolforschung in their position paper [2]. An important parameter for most of the microphysical processes associated with aerosols is the size of the particle. This property influences a range of different attributes like e.g. the sedimentation velocity, and the particle activation process for cloud formation and thus is essential e.g. for the overall particle lifetime in the atmosphere and influences cloud and precipitation formation and thus the direct and indirect climate effects.

To quote the IPCC (Intergovernmental Panel on Climate Change): “Over the historical period, changes in aerosols and their effective radiative forcing (ERF) have primarily contributed to a surface cooling, partly masking the greenhouse gas-driven warming.“ [3]. The effective radiative forcing describes the direct and indirect effects of change of the radiative budget the earth experiences [4], which then leads to a response of the global surface temperature. This means aerosols can influence the overall amount of energy the earth and its climate gain from the sun. Aerosols are not unique with this feature. A lot of so-called (essential) climate variables (ECV) like the Green Houses Gasses (GHG) ozone, nitrogen oxide, carbon dioxide or water vapour can do so, but aerosols have a net cooling effect. This is summed up in Figure 1.

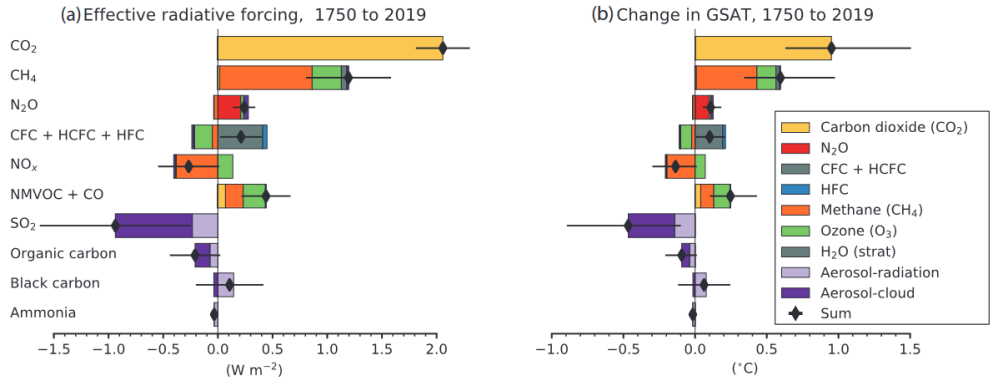

Figure 1. Effective radiative forcing changes from 1750 to 2019 (a) and global mean surface air temperature (GSAT) changes (b) from different climate variables according to CMIP6 model [3, 5].

By masking the warming effect of greenhouse gases, aerosols have a strong cooling effect on the Earth’s climate. With the beginning of clean air regulations for human health around 1970, the overall amount of anthropogenic aerosols in the northern hemisphere decreased contributing to the rapid rise in global surface temperature in recent decades [6]. Publications shows clear evidence of reduced aerosol radiation effects by direct and indirect means in recent years [7]. This

links that the overall cooling effect of aerosols is reduced due the decreasing concentration of aerosols.

A second thought to consider is the various adverse health effects aerosols can cause or worsen. Here the size of an aerosol is of importance since it influences the ability to enter the respiratory system [8]. This transmission ability can be used for medical applications such as inhalers. Air pollution in term of air quality contribute greatly to critical environmental issues [9]. Air quality consists of species such as e.g. nitrogen oxides, CO, tropospheric Ozone, SO_2 and aerosols.

A good overview of the interaction and feedback for climate variables and air quality is provided by Schneidemesser [10] in Figure 2. It shows the central role of aerosols summarised in particulate matter (PM) for which black carbon [11], organic aerosols or sulphate aerosols are important to name, as well as ozone and its precursors, like nitrogen oxide and nitrogen dioxide as air quality parameters.

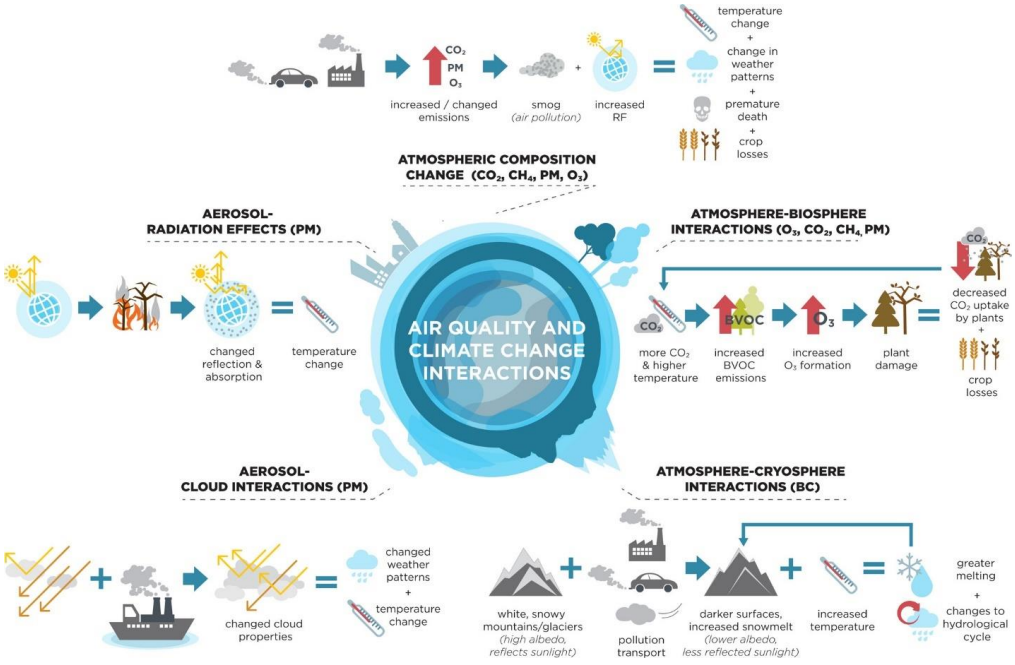

Figure 2. Overview of the main categories of air quality and their interaction with climate [10].

This thesis is about an instrument package that can measure aerosol properties relevant to those interaction effects. Stationary measurement stations give vital information and data to feed models and trend analysis. The continuous operation of measurement instruments on a global scale is necessary for widespread coverage and analysis. There are various research infrastructures with hundreds of organisations and platforms. These aim to collect, analyse and interpret measurement data. ACTRIS (Aerosol Clouds and Trace Gases Research Infrastructure) is one of the largest European research infrastructures with over 100 research performing organisations with the goal to perform observations of short-lived climate forcers and more atmospheric relevant parameters on the highest quality. Another research infrastructure combines aviation measurement with worldwide coverage and continuous with a scientific

institution. This infrastructure is called IAGOS. IAGOS is an acronym for In-service Aircraft for a Global Observing System. As the name implies, this infrastructure utilises long-haul passenger aircrafts as a measurement platform for global coverage [12]. The overall flight pattern and the cooperating airlines are visible in Figure 3.

Figure 3. IAGOS Flight routes since 2011; source: iagos.org.

By bringing instrument packages onto passenger aircraft, it becomes possible to measure in-situ the vertical profiles at the take-off and landing phases and at cruising altitudes of 9-13 km of various climate variables, such as water vapour, CO_2, O_3 or aerosols [13]. Since remote sensing techniques need to be calibrated using in situ instruments, a ground truth measurement is required. The research infrastructure IAGOS is providing in situ measured profiles of atmospheric aerosol extinction during the take-off and landing of in-service aircraft regularly. Those instrument packages have a variance of capacity on their measured climate variables. There are already packages in service that can measure nitrogen oxides and one that can measure aerosol number concentration and aerosol size distributions.

To close the gap for remote sensing techniques and to get a full picture of air quality parameters, it is necessary to develop an instrument package that combines existing, improved and novel measurement techniques. This instrument must withstand the harsh conditions of varying environmental pressure and meet the safety requirements for passenger aircraft. This instrument not only has to measure nitrogen oxides with high accuracy and fast response, but also aerosol optical properties, number concentrations and size distributions.

5 Background Knowledge

The abundance of aerosols can be described as widespread. In Table 1, an estimation of global emissions of aerosol mass is shown. The atmospheric lifetime of aerosols is limited, ranging from few hours to days depending on the size of the aerosol [14]. Aerosols large in size are sedimented or washed out frequently [15]. Nevertheless, as aerosols are generated frequently and influence weather and climate, which was already shown in Figure 2. Sulphate aerosols, which can be generated by volcanic eruption, decreases the global surface temperature by over half degree Celsius [16].

Table 1. Main Aerosol types in order by their magnitude of emission [17, 18].

Aerosol type	Emission (in megatons per year)
Sea-salt aerosol	500-2000
Formed by gaseous the phase	345-2080
Dust	7-1800
Anthropogenic aerosol	181-396
Aerosol from combustion	5-150
Biological aerosol	80
Volcanic Aerosol	4-90

The mass of aerosols is important, but also their size distributions. The size of an aerosol determines a set of properties, which are deeper described in section 5. A summary and illustration of the size classification of aerosols are given in Figure 4, which is an overview created by the U.S. EPA (Environmental Protection Agency).

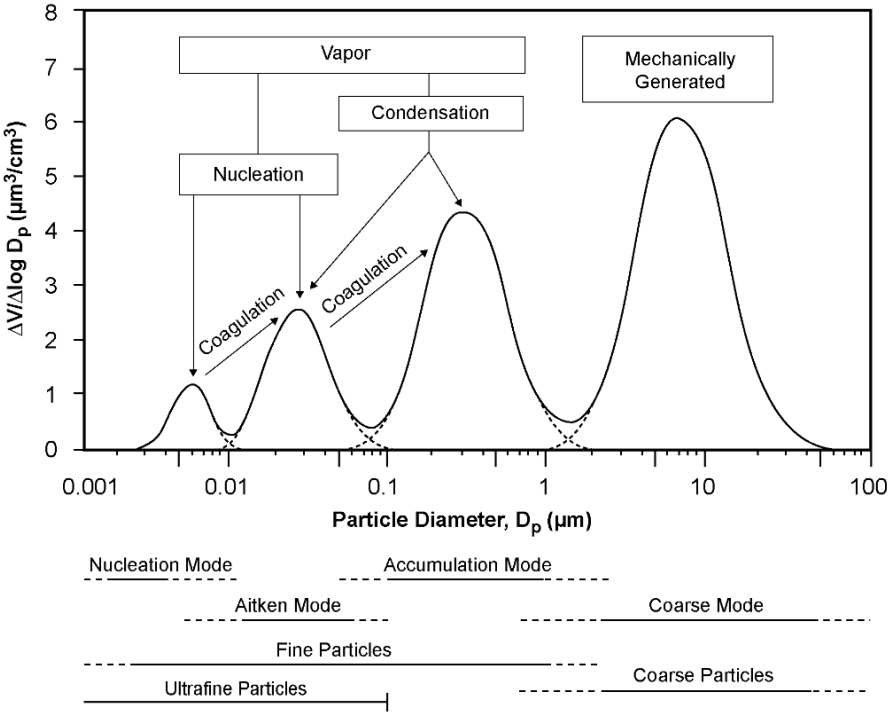

Figure 4. Size distributions of naturally occurring aerosols with their relative volumetric number density [19].

To start with the smallest size category, the nucleation mode contains particles freshly formed from the gas phase (Gas to particle conversion) with less than 10 nm in diameter. The Aitken mode represents atmospheric particles between 10 and 100 nm. Those particles are likely formed by heterogeneous condensation or growth of smaller particles and coagulation. The accumulation mode is formed by coagulation of smaller particles to particles in the sub micrometre range Those modes are primarily generated through vapour condensation and subsequently growing processes. Mechanic processes like rub-off or grind-down procedures typically form coarse particles lager 1 µm in diameter [20-22].

5.1 Aerosol Properties

This chapter is dedicated to a set of physical aerosol parameters relevant for this thesis like general background on aerosol characteristics and measurement techniques. This might be a mere fraction of all aerosol parameters, but the most appropriate for air quality are represented here.

5.1.1 Aerosol Number Concentration and Size Distribution

The number concentration is an essential property of aerosols. It describes the number of particles per volume. However, on its own, it gives only limited information about the aerosol and estimates for aerosol mass and air quality are insufficient. The size of a particle is another important parameter characterising its microphysical behaviour [23]. An aerosol size distribution (of one source) can be approximated by a log-normal distribution as a function of the particle size. In nature several log-normal modes normally sum up the total aerosol.

The probability density function (PDF) of a Gaussian normal function with respect to the particle diameter d_p is given by

$$df = \frac{1}{\sigma\sqrt{2\pi}} \exp\left(-\frac{(d_p - \bar{d}_p)^2}{2\sigma^2}\right) dd_p \quad \text{EQ 1}$$

with $\bar{d}_p$ as the arithmetic mean diameter and the standard deviation σ given by

$$\sigma = \frac{\sum n_i (d_i - \bar{d}_p)^2)^{1/2}}{N} \quad \text{EQ 2}$$

After logarithmic variable transformation of the particle size, the curve will show symmetric behaviour. This is shown in Figure 5. The most used logarithm for this issue is the natural logarithm[23].

The logarithm of σ is replaced by the geometric standard deviation (GSD) and is given by

$$ln\sigma_g = \frac{\sum n_i (lnd_i - \ln d_g)^2}{N - 1} \quad \text{EQ 3}$$

The GSD is always greater than 1.0 and dimensionless.

As for the number distribution, the median geometrical diameter is the same as the median of the Count Median Diameter (CMD). The PDF as a function of d_p using $d_g = CMD$ as an independent parameter, and by using the proportion $d \ln d_p = \frac{1}{d_p} dd_p$ this results in the following PDF:

$$df = \frac{1}{\sqrt{2\pi}\, d_p ln\sigma_g} \exp\left(-\frac{(\ln d_p - \ln CMD)^2}{2(\ln \sigma_g)^2}\right) dln\, d_p \quad \text{EQ 4}$$

95% of data lies between d±2σ in case of normal distribution. Similarly, 95% of particles of the lognormal number concentration lie between: $\exp(\ln CMD \pm 2 \ln \sigma_g)$, CMD/σ_g^2 and $CMD \cdot \sigma_g^2$. For σ_g=2, this corresponds to the fact that 95% of all particles can be found between a quarter and four times of the median of the count rate distribution.

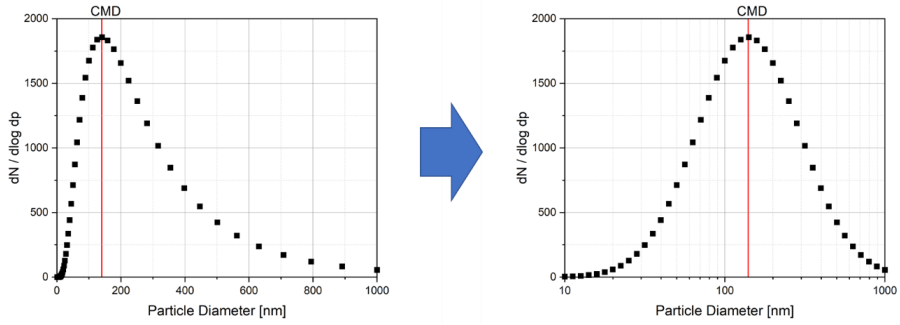

Figure 5. Illustration of the size distribution of a single source aerosol. With normal scale (left) and logarithmic scale (right) forming a gaussian distribution.

With this type of analysis, a fundamental basis of aerosol characterisation and physics can be described.

5.1.2 Mechanical Movement of Particles

Aerosol sampling is an important task and must be planned ahead to cover a total range of aerosol properties and size ranges. Particles can be lost in the sampling line by impaction, gravimetric settling or diffusion. For very small particles, the diffusion is the most important mechanism for particle losses. Those can be illustrated by diffusion losses in a cylindrical tube under laminar flow [23, 24]. The first thing to recognise is Stokes`s Law. This fundamental force F describes the total resisting force a spherical particle experiences by moving through a medium.

$$F = 3\pi\eta v d \qquad \text{EQ 5}$$

Here, η is the viscosity of the medium, v the velocity of the particle (relative to the surrounding medium) and d the diameter of the particle. The Cunningham correction Cc factor must correct an important assumption of this force. The assumption of the Stokes`s Law is, that the relative velocity of the gas at the surface of the sphere is zero This assumption becomes an issue for small particles in the range of the mean free path of “air” molecules.

$$F = \frac{3\pi\eta v d}{C_c} \qquad \text{EQ 6}$$

The Cunningham correction factor can be calculated using the mean free path length χ by

$$C_c = 1 + \frac{\chi}{d}\left[2.514 + 0.8\, exp\left(-0.39\frac{d}{\chi}\right)\right] \qquad \text{EQ 7}$$

Then the diffusion coefficient ξ for laminar flow can be calculated considering the temperature T by

$$\xi = \frac{1.38 \cdot 10^{-23}[\frac{J}{K}] \cdot T \cdot C_c}{3\pi\eta d} \quad \text{EQ 8}$$

With this, the dimensionless diffusion parameter μ can be calculated with the length of the tube l and the air flow rate f_a.

$$\mu = \xi \frac{l}{f_a} \quad \text{EQ 9}$$

Finally, the loss fraction P can be described by

$$P = 0.819e^{-11.5\mu} + 0.0975e^{-70.1\mu} + 0.0325e^{-179\mu} \quad \text{EQ 10}$$

This final product has to be multiplied by the particle concentration at the calculated particle diameter to get the number of particles that reach the measurement instrument [23].

5.2 Aerosol Optical Properties

Optical properties of aerosol particles depend on their size distribution, shape, morphology, chemical composition, and relative humidity of the air they are dispersed in [25]. Those can be divided into extensive aerosol optical properties and intensive aerosol optical properties. Extensive aerosol optical properties are correlating with the number concentration of the aerosol describing one property of the aerosol, whereas intensive parameters are independent of the amount of aerosol [4]. The most relevant pioneer of aerosol optical properties is Gustav Mie. He solved the Maxwell equations for spherical particles for his work on colloid silver nano particles [26]. Gustav Mie provided us with a theory to calculate light scattering and absorption properties for spherical particles. The incident plane wave and the scattered electromagnetic field inside and outside a sphere are described using a series of spherical wave functions, which satisfy the Maxwell equations. When boundary conditions are applied, transverse fields at the sphere's surface are matched to obtain outgoing spherical wave Mie coefficients. With these coefficients it is possible to determine the light extinction and scattering efficiencies Q_{ext} and Q_{scat} [26].

Purely light scattering aerosols are particles that only show scattering but no absorption. In other words, their imaginary part of the refractive index k equals zero. On the other hand, light absorbing particles are characterised by k > 0 [27].

For small particles in the Rayleigh scattering regime (x<<λ, λ = wavelength of the incident radiation)), the power series of spherical harmonics can be approximated by using only the first two terms. Leading to the known Rayleigh scattering equation (see EQ 11 below). The main particle properties needed are the complex refractive index $m = n + ik$ and the size parameter $x = \frac{\pi d_p}{\lambda}$. Light scattering efficiency is wavelength dependent. In the Rayleigh regime scattering intensity is proportional to λ^{-4}.

$$\sigma = \frac{8\pi d^6 x^4}{3} \cdot \left(\frac{(\frac{n_2}{n_1})^2 - 1}{(\frac{n_2}{n_1})^2 + 2} \right)^2$$ EQ 11

Particles of the size of the wavelength require the full solution of the Mie power series [23].

$$Q_{scat} \cong \frac{8}{3} x^4 \left| \frac{m^2 - 1}{m^2 + 2} \right|^2 \quad and$$ EQ 12

$$Q_{abs} \cong 4\, x\, Im\left\{ \frac{m^2 - 1}{m^2 + 2} \right\}$$ EQ 13

The equation shows that the scattering and absorption efficiencies Q have different dependencies on the light wavelength and particle size d_p.

In an oversimplified matter, a scattering particle could be idealised as a sphere in its geometrical size. This sphere redirects incoming radiation into new directions, attenuating the transmitted radiation. This process can be described formally in analogy to a shadow behind the particle downstream following the incident light. Here the size of this shadow can be described as an effective cross-section and is measured as an area (m^2). This effective cross-section can be larger or smaller than the geometrical cross section of the particle. That proportional factor is described by the scattering efficiency Q_{scat} calculated by Mie theory. When a certain number of particles are given in a given volume of interest, the sum of all effective particle cross sections determines the scattering coefficient $\sigma_{sp.}$ Essentially this is the cross-section per volume, or volumetric cross section, and is given in the unit of inverse meters or m^{-1}. This can be viewed in EQ 14 in Section 5.2.1.

5.2.1 Extensive Aerosol Optical Properties

The extensive parameters for aerosol light interactions are extinction, scattering and absorption. Analogue to the introduced scattering coefficient the absorption coefficient is defined as the sum of the effective absorption cross sections. The extinction coefficient is defined as the sum of scattering- and absorption-coefficients (see EQ 12), which is required by the conservation of energy:

$$\sigma_{ep} = \sigma_{sp} + \sigma_{ap}$$ EQ 14

where σ_{ep} is the extinction coefficient, σ_{sp} the light scattering coefficient and σ_{ap} the coefficient for light absorption by particles. The unit of all these parameters is often given in Mm^{-1} ("inverse Mega meters"; 1 Mm^{-1} = 10^{-6} m^{-1}).

Solving the equation for σ_{ap} , it is possible to derive the absorption coefficient using measurements of the extinction- and scattering coefficients. In the following this will be called the Differential Method (DM).

The extinction coefficient describes the intensity I of a beam of incident light I_0 passing a specific medium with the length L, by absorption and scattering of light by means of the Beer-Lambert Law[24]:

$$I = I_0 \cdot e^{-\sigma_{ext} \cdot L} \quad \text{EQ 15}$$

$$for\ which\ is\ true\ \sigma_{ext} = \sigma_{scat} + \sigma_{abs} + \sigma_{sp_gas} + \sigma_{a_gas} = ln\frac{I}{I_0}/L$$

L is the length of the light path, I is the intensity of light (I_0 intensity of incident light) and $\sigma_{sp_gas} + \sigma_{a_gas}$ is the Rayleigh scattering and absorption of the medium air. The Scattering signal is composed out of Rayleigh scattering and scattered light of particles. Therefore, the overall light extinction is made by aerosol particles and gas molecules in the medium air. Using $Q_{ext} = Q_{scat} + Q_{abs}$ for the efficiency parameter. Rayleigh scattering is usually subtracted by the measured baseline determined using particle free air sample [28].

$$\sigma_{ext}(\lambda, m) = \int_{-\infty}^{\infty} \left[Q_{scat}(d_p, \lambda, m) + Q_{abs}(d_p, \lambda, m)\right] \cdot \frac{\pi d_p^2}{4} \cdot \left[\frac{dN}{d \log d_p}\right] d \log d_p \quad \text{EQ 16}$$

Both the scattering efficiency Q_{scat} and the absorption efficiency Q_{abs} of each particle depend on the light wavelength, particle size, shape, and the complex refractive index. In addition, σ_{ext} also depends on the size distribution $\left[\frac{dN}{d \log d_p}\right]$, while the term $\frac{\pi d_p^2}{4}$ describes the particle cross-section[27].

The efficiencies for light extinction, scattering and absorption (Q_{ext}, Q_{sp}, Q_{abs}) can be calculated by Mie Theory for spherical particles or e.g. using T-Matrix calculations for more complex shapes.

The direct radiative effect depends on the light extinction coefficient $\sigma_{ext}(\lambda, z)$ or its vertical integral, the AOD (aerosol optical depth) $\delta(\lambda)$, in which z represents the altitude and is often measured by remote sensing techniques.

$$\delta(\lambda) = \int \sigma_{ext}(\lambda, z)\, dz \quad \text{EQ 17}$$

5.2.2 Intensive Aerosol Optical Properties

Intensive aerosol parameters like the Single Scattering Albedo (SSA) or the Ångström exponents are often calculated from multiple instrument datasets, which can lead to an increase in errors and uncertainties with regards to this parameter. The importance of reliable intensive parameters is undisputable, especially, when their use is required for an experiment or sensitive climate-related modelling. The Ångström exponents are widely used to adjust extensive parameters to a desired wavelength [29],[30] for instrument comparison and more importantly for aerosol characterisation [31] like the refraction index calculation of mineral dust [32] or black carbon [33], or source identification of mineral dust [34]. The scattering Ångström exponent (SAE) is particle size-dependent and, therefore, is used to indicate the size distribution of aerosols in the

investigated medium. An SAE value of 4 indicates either a gaseous medium or a medium with nanometre-sized particles, whereas a value of zero indicates coarse particles [35].

The absorption Ångström exponent (AAE) depends on the aerosol's chemical composition. A value of 1 indicates an aerosol which absorbs light strongly across the entire visible spectral range and is composed of nanometre-sized spheres [36]. This behaviour is characteristic e.g. for fresh soot or black carbon agglomerates [37, 38]. AAE values higher than unity indicate the presence of brown carbon [33] or mineral dust, which are characterised by a stronger absorption in the blue and ultraviolet compared to the red spectral range. The extinction Ångström exponent (EAE) is often used for aerosol classification by remote sensing methods such as Lidar (light imaging, detection and ranging) and depends on the size distribution and chemical composition [39, 40]. Combining those exponents in a cluster plot is a reliable method for classifying aerosol sources [31].

The SSA of an aerosol is the crucial parameter for its direct or semi-direct impact on the climate [41]. It describes the ratio of scattering to total extinction of a medium. The value of 1 indicates that light extinction relies exclusively on light scattering. In contrast, low SSA values indicate an aerosol with a large fraction of light-absorbing components, which may cause atmosphere heating. The intensive parameters are only available through multiple-instrument approaches at different wavelengths, which requires a detailed analysis of measurement uncertainties [42].

The Single Scattering Albedo (SSA), is defined by:

$$\mathrm{SSA}(\lambda) = \frac{\sigma_{sp}(\lambda)}{\sigma_{ep}(\lambda)}$$

Particles as small as 100 nm or smaller cannot scatter visible light efficiently because of the strong dependence of Q_{scat} on d_p to the power of 4, whereas Q_{abs} depends only proportional to the particle diameter. Therefore, nanometre-sized particles (d_p<100 nm) with a large imaginary refractive index show smaller SSA values while particles of similar chemical composition but larger in size, show larger SSA values which can be viewed in Figure 6.

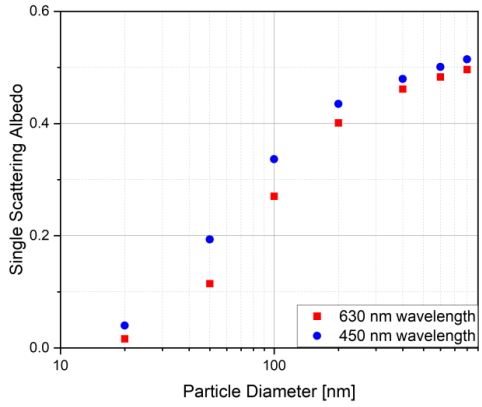

Figure 6. Calculated Single Scattering Albedo of a mono-modal aerosol determined at two different wavelengths. using a complex refractive index of 1.75+i0.63.

The Ångström exponents (AE) describe the strength of the wavelength dependence of the aerosol optical coefficients. Usually, the extensive parameters of the aerosol light extinction (ep), scattering (sp) and absorption (ap) increase with the frequency of the light.

$\sigma_{xp}(\lambda) \propto \lambda^{-AE}$; with $\sigma_{xp} = \{\sigma_{ep}, \sigma_{sp}, \sigma_{ap}\}$ EQ 18

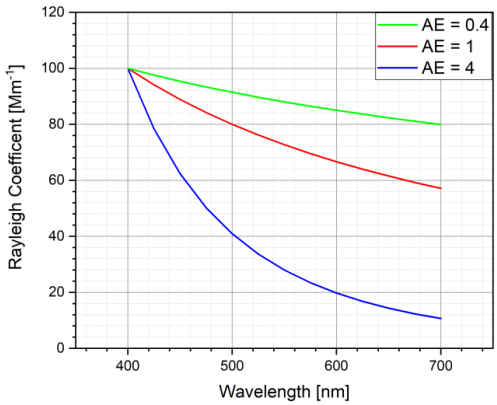

Figure 7. Illustration of the wavelength dependency of the aerosol Rayleigh scattering coefficients with different Ångström exponents.

The Ångström exponents AE are calculated starting from the ratio $\frac{\sigma_p(\lambda 1)}{\sigma_p(\lambda 2)}$ using EQ 20 for two different wavelengths $\lambda 1$, $\lambda 2$ and solving this for the AE:

$$AE = -\frac{\log\left(\frac{\sigma_p(\lambda 1)}{\sigma_p(\lambda 2)}\right)}{\log\left(\lambda 1/\lambda 2\right)}$$ EQ 19

By solving AE for $\sigma_{xp}(\lambda 1)$ as a function of the Ångström exponent and the attenuation coefficient $\sigma_{xp}(\lambda 2)$ the resulting equation is used for wavelength adjustments

$$\sigma_{xp}(\lambda 1) = \sigma_{xp}(\lambda 2) \cdot \left(\frac{\lambda 1}{\lambda 2}\right)^{-AE}$$ EQ 20

Substituting σ_{xp} in EQ 20 with σ_{sp}, σ_{ep} or σ_{ap} we obtain the absorption Ångström exponent (AAE), extinction Ångström exponent (EAE) and scattering Ångström exponent (SAE), respectively.

5.3 Aerosol Measurement Techniques

There are many aerosol instruments with an even more comprehensive range of applications. They are not exclusively used for air pollution and climate measurements but also for an increasing number of controlled and monitored aerosol processes [24]. This work will focus on

aerosol instruments for measuring optical parameters, explicitly the scattering-, absorption- and extinction coefficients, as well as on particle counting and sizing methods. In this section the associated measurements techniques are introduced, and the underlying principles are discussed.

5.3.1 Instruments for Particle Counting

When it comes to aerosol particle counting, one instrument family is omnipresent for submicrometer particle measurements: the Condensation Particle Counter (CPC). A pump draws continuously a controlled sample flow including the dispersed particles in the air into the apparatus. Inside the instrument, they are first led into a temperature-controlled saturation chamber (e.g. 35°C for the working fluid Butanol) to expose particle to an atmosphere saturated with the working fluid vapour. Downstream, the mixture enters a condensation section where the sample is cooled down (e.g. 10° C for Butanol). There, the working fluid vapour gets supersaturated and condenses onto the particles as described by the Kelvin-Köhler theory [23]. The supersaturation is governed by the temperature difference between the saturator and the condenser.

The temperature difference must not exceed a certain value in order to avoid homogenous condensation. This process effectively grows the particles to a size in the order of 10 µm, independent of their initial size.

Consequently, the particles are large enough to be directly detected by laser light scattering in an optical detector. By growing the particles to an optically detectable size, a CPC is not able to differentiate between different particle sizes and can only be used for determining the total number concentration of particles [43]. The instrument components are illustrated in Figure 8.

The laser optic can detect single particles in a concentration range from 1 to 100,000 particles per cubic centimetre, depending on the instrument model used. If higher particle concentration are intended to be measured, the aerosol should be diluted first [44].

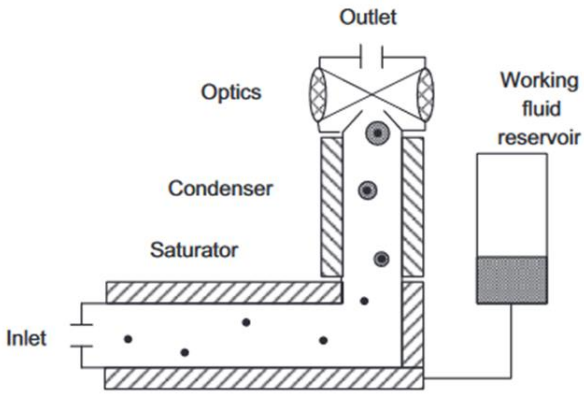

Figure 8. Schematic of the basic set-up for the alcohol-based condensation particle counter [45].

Depending on the model, a CPC is suitable for accurately measuring particles starting from ~3 nm or 27 nm. The design of the CPC is therefore of importance.

The supersaturation of the working fluid vapour at the condenser determines the smallest possible particle size which will be activated (critical diameter) to grow, and thus, will be detected by the optical unit. For pure liquids this ratio p/p_s can be expressed through the Kelvin equation [23, 46] ,where the following parameters are used: The surface tension of the liquid σ_l, the molecular weight M, the density δ, the general gas constant R, the absolute temperature T and the Kelvin diameter d_k:

$$\frac{p}{p_s} = \exp\left(\frac{4\sigma_l M}{\delta R T d_k}\right) \quad \text{EQ 21}$$

The Kelvin diameter shows at which saturation ratio p/p_s the droplet is in equilibrium with its surrounding gas phase and the droplet neither starts to grow nor shrink to due condensation processes or evaporation.

When a soluble nucleus is considered, the particle growth can be initiated by a mere percentage needed for a pure liquid. A given mass of a salt reduces the given vapor pressure at the droplet surface. The relationship between the kelvin ratio and the particle size with dissolved matter is given by [23]:

$$\frac{p}{p_s} = (1 + \frac{6imM}{M_s \delta \pi d^3})^{-1} \exp\left(\frac{4\sigma M}{\delta R T d_s}\right) \quad \text{EQ 22}$$

Where m is the mass of the dissolved material and M_s the molecular weight. The constant i is the number of molecules the salt will dissolve into. This equation can then be solved for a particle size d_s when the maximal supersaturation ratio is known. For vapour pressure calculations the empirical Antoine equation can be used [47]:

$$log_{10} p = A - \frac{B}{C + T} \quad \text{EQ 23}$$

For which A, B and C are component-specific constants, p is the vapour pressure and T the Temperature. When solved for two different temperatures, the ratio of those will be the supersaturation for this calculated temperature difference [48].

5.3.2 Instruments for Particle Size Distribution Measurement

5.3.2.1 Differential Mobility Analyser

The second most common device to support the aerosol scientist is a device, that separates monodisperse sized particles from a polydisperse sample.

Ultrafine (smaller than 0.1 µm) and fine particles (0.1 to 1 µm) can be size-classified according to their electrostatic mobility in an electrical field in a Differential Mobility Analyser (DMA). Particles larger than 1 µm will be removed from the sample by a pre-impactor, because those would harm

the instrument because of flashover, since a voltage over 10 kV would be needed to analyse those. After passing through the inlet, the particles enter a charger in front of the DMA. This charging stage is crucial to achieving a well-defined charge distribution on the particles. The separation of polydisperse aerosols into monodisperse sizes takes places inside the DMA with the help of an electric field, which is applied between an inner and an outer electrode. Particle are injected in a laminar sheath-flow close to the outside rod. Negatively charged particles are accelerated towards the inner rod by means of their electrostatic mobility. Thus, only particles of a certain electrostatic mobility will be separated entering a small slit located at the inner rod. A schematic of this principle is shown in Figure 9. A DMA can be operated stepwise to determine a particle size distribution, or it can be kept on the same voltage level to create a monodisperse aerosol for a long time. The length of the column and the voltage determine the maximum classification ability of the device.

Charged particles can be directed in an electrical field. For the electrical mobility of the particles in an electrical field this formula applies [49]:

$$Z = \frac{n_i e_0 C_C(D_P)}{3\pi\eta D_p} \qquad \text{EQ 24}$$

With the n_i number of elementary charge on particle, Here e_0 denotes the elementary charge, D_p the mobility equivalent size of the particle, Z the electronical mobility, η the dynamic viscosity, $C_c(D_P)$ the slip correction factor.

The DMA separates particles using electrical mobility while neglecting diffusion effects by:

$$Z = \frac{Q_{Sh}}{2\pi LU} \ln\left(\frac{r_a}{r_i}\right) \qquad \text{EQ 25}$$

With the sheath-flow Q_{Sh}, the DMA length L, the DMA voltage U, the outer radius r_a and the inner radius r_i.

The full width at half maximum of the particle electrical mobility distribution is determined via the following ratio and describes the size resolution of the instrument:

$$\Delta Z = \frac{Q_A}{2\pi LU} ln\left(\frac{r_a}{r_i}\right) = \frac{Q_A}{Q_{Sh}} Z \qquad \text{EQ 26}$$

With the aerosol flow Q_A [50].

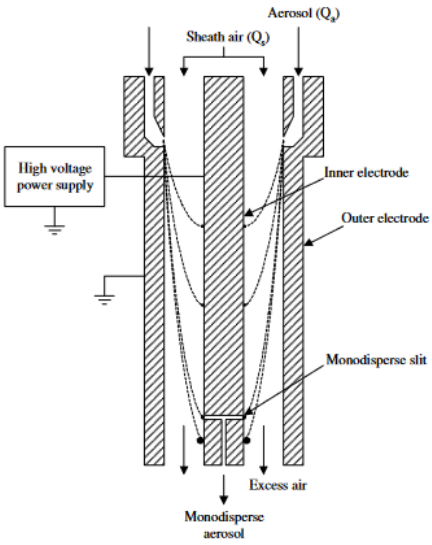

Figure 9 . Illustration of the functional part of the Differential Mobility Analyzer [51].

Particles of different sizes could enter the slit, as the mobility diameter, can be equivalent for particles with multiple charges and a higher particle size and mass.

5.3.2.2 Optical Particle Counter

An optical particle counter (OPC) can be used for both sizing and counting. This technique uses the intensity of light scattered by a particle for determining the size. A commercially available optical particle counter can have different specification mostly depending on applied wavelength of the used laser. Depending on the settings, a device with a laser of 650 nm wavelength has multiple size channels for particle size classification ranging from 0.25 to 3.2 µm. This is visible in Figure 12. In an OPC, the sample is led via a nozzle into the measuring zone of the device where airborne particles are detected by scattering of light. A basic illustration of the measurement principle is shown in Figure 10. The particles scatter the incident light. The scattered light intensity is measured by means of a detector either measured directly or collected by a spherical mirror to broaden the scattering angle range to smoothen the signal response curve.

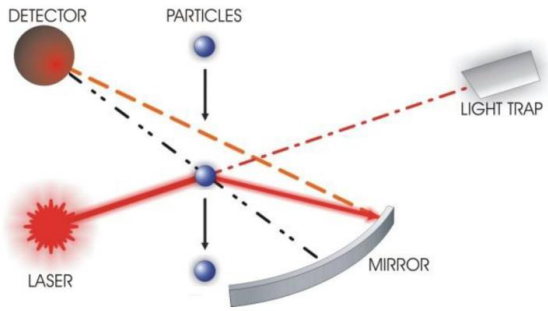

Figure 10. The basic principle of optical particle detection and sizing [52].

The measured scattered light intensity varies with particle size, which enables us to measure the particle size distribution. A concave mirror leads the scattered light towards a photodetector which converts it into an electrical signal. The OPC then determines the particle size distribution by relating the signal peak height of the detected intensity to calibration data using spherical polystyrene latex beads (PSL) particles of known size and chemical composition i.e. refractive index. This results in the measured particle size being equivalent to the PSL diameter [53].

The particle number density is determined by the ratio of the particle counts and the volume flow rate. Additionally, it is essential to mention that the intensity of light scattering depends on factors other than the particle size, e.g. the shape of the particles, their morphology and the refractive index. The signal is integrated over a slight range of scattering-angle to suppress variations of the scattering signal. However, at a detection angle of 90°, uncertainties can be minimized[24].

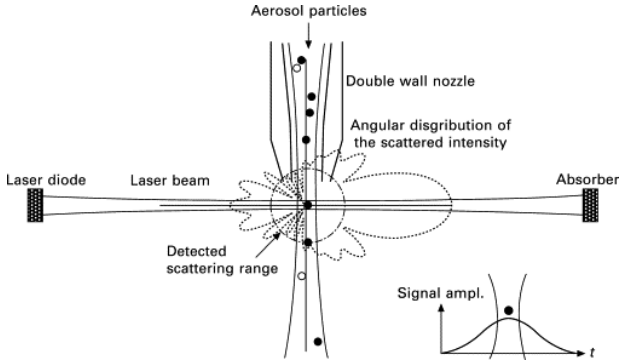

Figure 11. Principle of optical particle spectrometers superimposed with a typical scattering profile of an aerosol. [54]

Figure 11 shows the measurement principle in more detail and illustrates the angular distribution of the scattered light with its intensity. The shape and intensity vary with specific characteristics of the particle, such as its size parameter and refractive index.

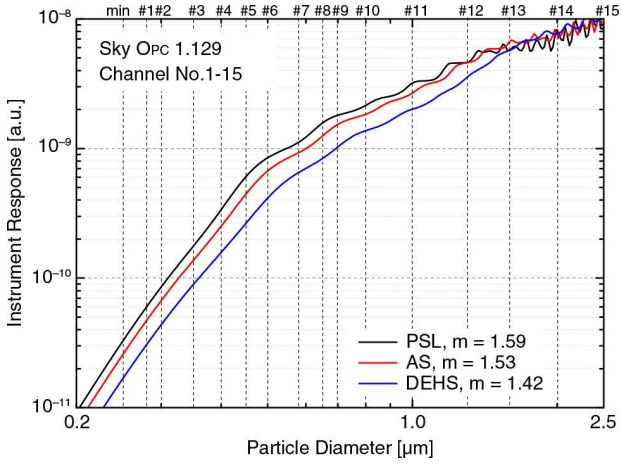

Figure 12. Calculated scattering intensity curves for different particle types (PSL; polysterene latex, AS; ammonium sulphate and DHES diethylhexylsebecat) [55].

5.3.3 Instruments for Aerosol Optical Properties Measurements

There is a vast number of instruments to choose from for aerosol optical properties. A small selection is presented here, chosen because those were used during the thesis. A central instrument, that was used excessively in this thesis, delivers the aerosol light extinction coefficient.

The Cavity Attenuated Phase Shift (CAPS PM_{ex}) device is a light extinction monitor, which detects a phase shift through a cavity ring-down process. The LED light source emits a square wave signal at a steady frequency. At both ends of the cavity are highly reflective mirrors, as shown in Figure 13. Under this given condition, the cavity will be loaded with the light of the LED. Turning off the LED, the trapped light will be discharged by extinction and by losses at the mirrors (total loss). The amount of light loss by particles (PM_Loss) is directly proportional to the extinction coefficient of the medium within the cavity. When there are particles inside the cavity the amount of loaded light will decrease much faster. This time delay is described as a phase shift and used to calculated the aerosol light extinction coefficient [56] as it is shown in Figure 14. The losses by the mirrors are estimated by particle free baseline measurements regularly taken during the experiments.

The particle loss PM_loss is calculated by subtraction of the baseline loss from the total loss signal.

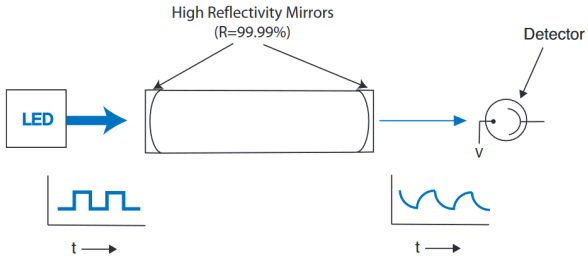

Figure 13. Schematic of signal generation of the cavity attenuated phase shift monitor [57].

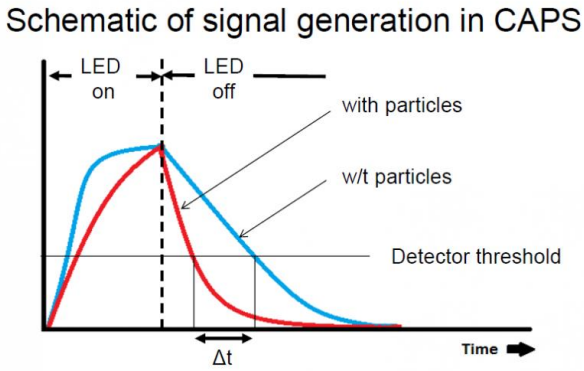

Figure 14. Illustration of the primary mechanism to derive the light extinction coefficient [58]. The same mechanism applies for the use of nitrogen dioxide as specimen instead of particles.

The relation between phase shift ($\phi - \phi_0$) and the extinction coefficient can be described by

$$\sigma_{ext} = \frac{2\pi f}{c} \cdot (cot\varphi - cot\varphi_0) \qquad \text{EQ 27}$$

A version of this instrument is able to deliver the aerosol light extinction coefficient and the aerosol light scattering coefficient. This instrument type is called CAPS PM_{SSA}. An integrating sphere is placed in the middle of the cavity and a transparent narrowing is used central of the steel cavity to let scattering light into the integrating sphere.

As f is the frequency of the square wave signal of the LED, c is the speed of light and ($\phi - \phi_0$) describes the amount of phase shift, where ϕ_0 is the phase of the particle-free probe measured as a baseline [58].

This extinction measuring method is absolute and needs no calibration. Some corrections are still applied, that are linked to the sheat-flow, that is used to protect the mirrors from pollution [59]. To perform a baseline measurement, the airflow is directed through an integrated filter to measure particle free air[60].

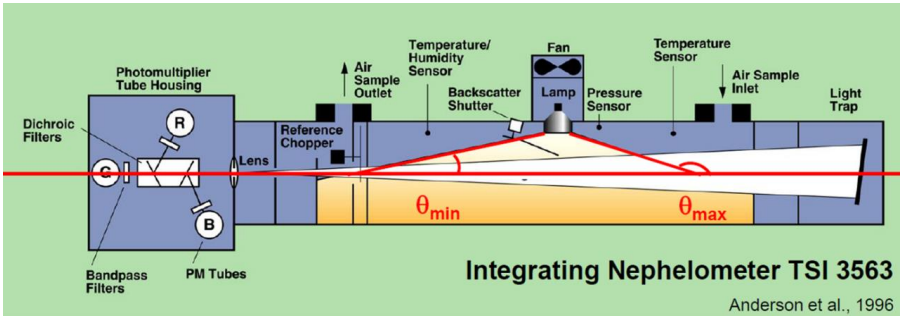

Figure 15. Schematic of an integrating nephelometer (© TSI)

The integrating nephelometer is a generally accepted reference device for light scattering. It typically measures one to three different wavelengths (λ = 450, 550, 700) to determine the behaviour of scattering in the visible light spectrum. The inner walls are completely black to avoid backscattering and molecular scattering is subtracted after measurement of HEPA-filtered air, so only the scattering coefficient of airborne particles is measured.

Furthermore, there is an instrumental dependent truncation error, because the measurement has a geometric limit of the measured scattering-angle range of 7 to 170° instead of 0 to 180°. The truncation error correction depends strongly on the particle size. Thus, for measuring atmospheric aerosol the size-distribution has to be assumed or measured / approximated for this data correction. The truncation error has been investigated to correct the measurements for scattered light missed in direct forward 0°-7° and backward direction 170°-180° which cannot be measured directly by the nephelometer for technical reasons. A correction factor for the missing truncation error can be calculated using the scattering Ångström-exponent [61]. The Scattering Ångström exponent is used, as an indicator for the size distribution, which cannot be measured with the Nephelometer, but would be more accurate for calculations of the truncation error.

Aerosol light absorption measurements were done with an absorption photometer. The Tricolour Absorption Photometer has eight sample spots, which will be loaded on a glass-fibre filter, one after another, and two spots for reference. Three different LED`s are installed with wavelengths of 467, 528 and 652 nm to cover the visible light spectrums. The TAP device has its roots in the NOAA Continuous Light Absorption Photometer (CLAP) and follows the same physical properties.

To calculate the absorption coefficient σ_{abs} is given for any filter-based method by this equation:

$$\sigma_{TAP} = \frac{A}{V} \ln\left(\frac{I_0}{I}\right) \qquad \text{EQ 28}$$

With the sample spot area A , V the air volume that is drawn trough the filter during the sampling time and $\left(\frac{I_0}{I}\right)$ is the ratio of light transmitted through the sample spot and reference spot [62].

The correction for particle absorption photometers is implied in the software [63]. The equation is given by:

$$\sigma_{abs} = \frac{1}{1.2369\,Tr + 0.8135}\sigma_{TAP} \qquad \text{EQ 29}$$

With the transmission Tr, which is 1 for unloaded filter, σ_{TAP} is the absorption coefficient measured and σ_{abs} the correct value for the absorption coefficient.

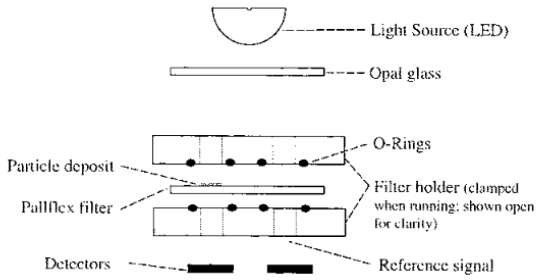

Figure 16. *Setup for a Particle Soot Absorption Photometer (PSAP). The same principle is true for the TAP. Particles are deposited on the filter and a second particle free spot is set as a reference spot as light is transmitted through the filter onto the detectors* [62].

5.4 Nitrogen dioxide

Chemiluminescence detection (CLD) is widely used for the observations of NO and NO_2 in laboratory and field studies, and long-term monitoring [64, 65]. Briefly, the NO_x mixing ratios for NO2 and NO are determined by switching on and off a converter. The converter could be consistent of a heated catalytic surface or photocatalytic. If the converter is switched off or bypassed, NO is titrated with O_3 added in the reaction chamber and the subsequent chemiluminescence signal is detected by a photomultiplier tube (PMT) as per the following reaction:

$$NO + O_3 \rightarrow NO_2^* + O_3$$
$$NO_2^* + M \rightarrow NO_2 + M$$
$$NO_2^* \rightarrow NO_2 + h\nu$$

Most of the excited NO_2 returns to the ground state by collisional quenching with either other atmospheric molecules (typically N_2 or O_2) or through the emission of photons, the emission of which take place in the wavelength range of 590-3000 nm with a peak at 1200 nm [66].

By switching the converter on NO_2 is catalytically reduced to NO and then detected as described before. The NO_2 mixing ratio is then calculated by the difference of the measurements with PLC switched on and off respectively [67, 68]. CLDs equipped with photocatalytic converters have also been shown to be subject to interferences as the thermal decomposition of peroxyacetyl nitrates within the photolysis cell can positively bias the NO_2 measurements [69].

The CAPS System can also be used for nitrogen dioxide measurements, since this species strongly absorbs light at this regime, with little to no interference of other atmospheric widespread gases. This requires the CAPS monitors to consist of a blue light emitting diode (LED) as the light source, a sample cell with two reflective mirrors and a vacuum photodiode detector. The working principle is based upon a phase shift in modulation (as described in section 4.3.3) when a square wave modulated LED light is input into the first reflected mirror and is distorted in terms of the waveform after passing through the absorption cell in comparison to the initial modulation. The amount of phase shift then corresponds to the concentration of NO_2. Knowing the absorption cross section of NO_2 the number concentration can be directly calculated, and no calibration is required [68, 69].

6 Air Quality Instrument - Instrument Package 2E

This section describes the new device for measuring air quality parameters for the research infrastructure IAGOS. The instrument package consists of several devices for measuring aerosol properties and nitrogen dioxide mixing ratio.

The very first prototype design of package 2e by Ulrich Bundke was equipped with fewer measurement instruments than the final product. This, however, was a proof of concept. The later adaptations, installations and qualifications were done as part of my PhD. The first results with this instrument prototype package showed promising results, but with some limitations. Those limitations are based on the number of aerosol measuring devices. The original plans for P2e included two CAPS tubes. One tube was operated for aerosol light extinction measurements and the second tube was designed for nitrogen dioxide measurements. The aerosol particle counting, and sizing was operated by an optical particle counter with a wavelength of 650 nm. The original design can be viewed in Figure 17.

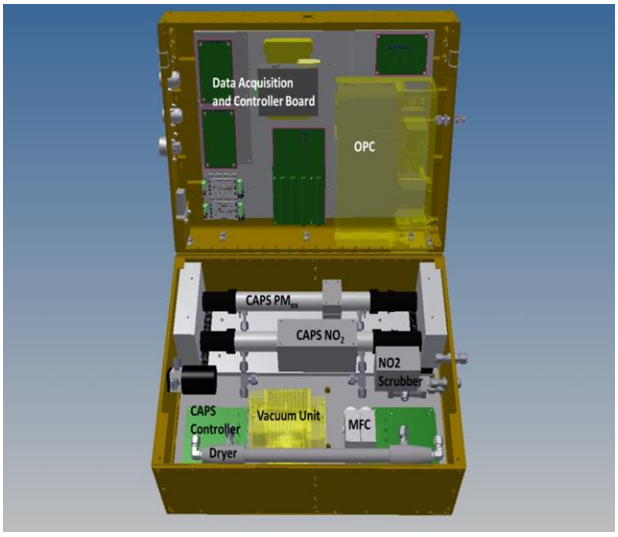

Figure 17. First concept of the air quality package [70].

In Figure 18 a list of all measuring instruments for the final product is provided with the cooperation partners we actively exchange information with. This includes Aerodyne Research Inc. With their help, we manufactured the multiple CAPS instruments inhouse. The cooperation with aerosol devices helped to extend their instrument water-based CPC (MAGIC CPC) operation range to pressures down to 200 hPa, which is now commercially available. The package consists of a modified Portable Optical Particle Spectrometer (POPS [71] originally developed by NOAA) which measures the particle size distribution in the diameter range from 125 nm to 4 µm; four Cavity Attenuated Phase Shift (CAPS [58, 72] Aerodyne Research Inc., Billerica, MA, USA) instruments to measure the particle extinction coefficients at different wavelengths as well as the NO_2 concentration.

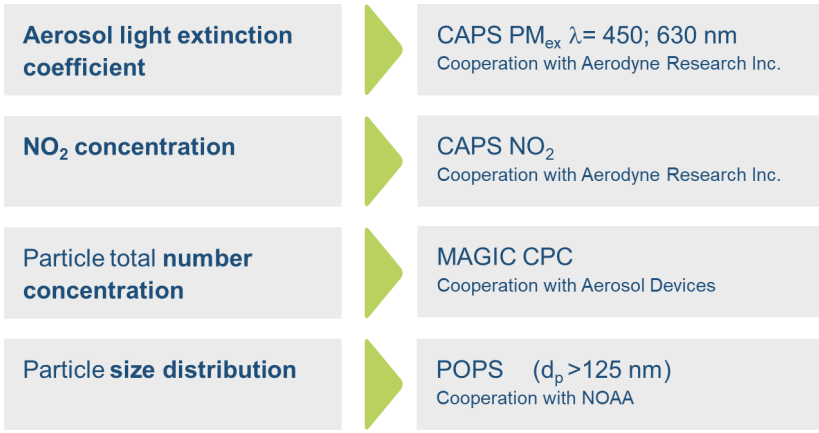

Figure 18. List of instruments and corresponding cooperation partners.

For a quick overview, a plumbing plan is provided in Figure 19. Without going into detail, it gives impressions about the overall density of the instrument package. Multiple low delta P mass flow controllers were needed for a stable sample volumetric flows for all operational pressure conditions and as quality parameters a set of pressure sensors, heating devices and aerosol filters are provided. This is needed, to keep the measured parameters in good quality. Heating devices are needed, to keep the instruments at a stable temperature, as the CAPS response or the laser output can change with the temperature. Aerosol filters are added to provide an aerosol-free sheath air flow for several devices.

To counter cross sensitivity for light absorbing gaseous species, a third CAPS tube for aerosol light extinction is installed with a particle filter in front of the tubing. With this, a permanent baseline is set, to correct the aerosol light extinction of the main CAPS PMex permanently. As the optical detectors of the aerosol 450nm CAPS-PMex are far less sensitive than the CAPS NO_2 detectors, we do not expect to have a high cross-sensitivity of gaseous media, that absorbs light at 450 nm. A permanent baseline enables to correct those cross-sensitivities and more important also short-term pressure changes, that could affect the measurements. If this third tube is not needed for permanent baseline corrections, a green wavelength could be installed, which then could help to identify e.g. mineral dust showing a strong shift of the Ångström exponent between 630 nm to 550 nm and 550 nm to 450 nm.

Another focus was the installation of an automatically turn on and off the auto-baseline of the CAPS instruments during ascent and decent of the aircraft. Vertical profiles are important products of the instrument package. To fully measure them, the auto-baseline must be turned off during landing and take-off. A Virtual instrument (VI) was installed, that checks the pressure changes inside the package. If the standard deviation exceeds a certain threshold (lower 5 hPa) during a short period of time, the auto-baseline is disabled. We tested this with recorded flight data and the auto-baseline only was enabled during cruising altitudes.

All measured parameters are time synchronised saved in one TDMS file, located at the main CPU and an SD-Card. The Data Transfer can be done via SFTP using an ethernet connection or by an automated USB-Stick download.

Several instrument comparison measurements were done, to the check internal behaviour and correction factors, and implied into the initial files of the devices. During multiple measurements, it became clear, that the instrument package delivers stable measurement data output with a slope of 1.0 ±0.05 compared to their counterparts of the instrument lines. We checked the instrument particle loss, by replacing the MAGIC-CPC inside the instrument package multiple times as well with measurements done with side-by-side measurements.

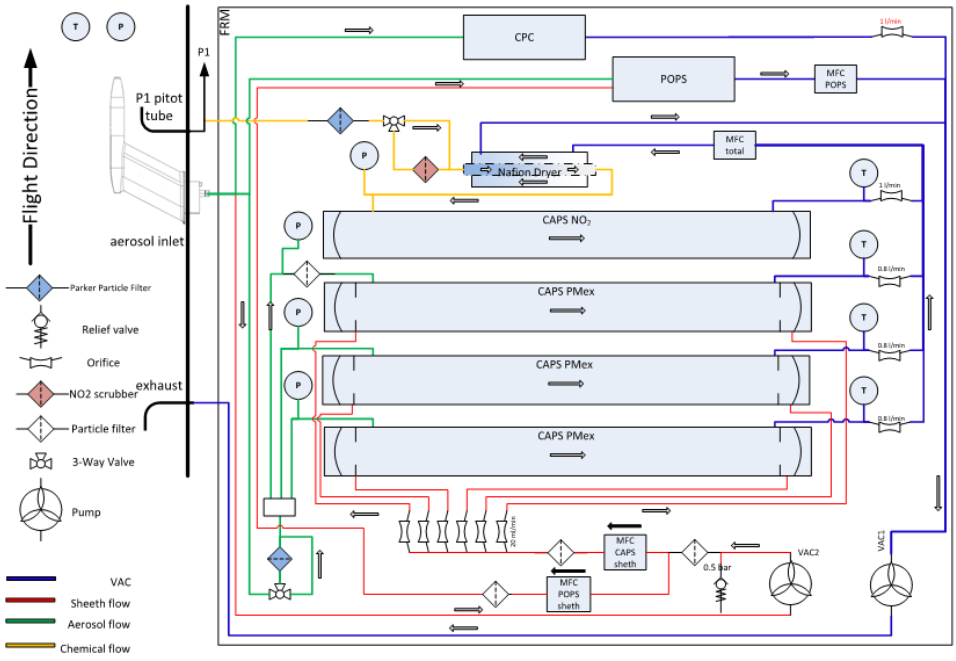

Figure 19. Detailed flow chart of P2e for aircraft operation [73].

Without going into detail, sample air is distributed via the Vac 1 pump. The sample air is then distributed into several individual volume flows. These then lead to the individual measuring instruments. A three-way valve controls the mode for the baseline of the aerosol CAPS

instruments. Another three-way valve is used for the Nafion dryer and scrupper. The MFCs are used to maintain a constant volume flow.

On operation the instrument package is connected to the outer air by a dedicated aerosol intake and pitot type chemical Teflon coated inlet. The aerosol intake transmits particles up to 3.5 µm. The first stage of the inlet is a devertor reducing the velocity of the air flow resulting in an increase of ram pressure of about 60 hPa [74, 75]. Afterwards the aerosol is iso-axial and isokinetic sampled by a pinhole nozzle while the main airstream exits the probe at the aft. The aerosol inlet is connected to the instrument by a conductive sample line of appr. 1 m length. Inside the instrument the aerosol flow is then divided into six separate streams by means of sharp-edged dedicated aerosol flow splitters. Those were guided as sample flows towards the three CAPS aerosol light extinction tubes, the MAGIC CPC the POPS and as source of the particle filtered sheath flows for the CAPS tubes and POPS. The NO_2 CAPS System has its own sample flow from the chemical pitot type inlet. This is because the aerosol devices are connected with a conductive rubber or stainless steel, which would influence NO_2 concentration significantly.

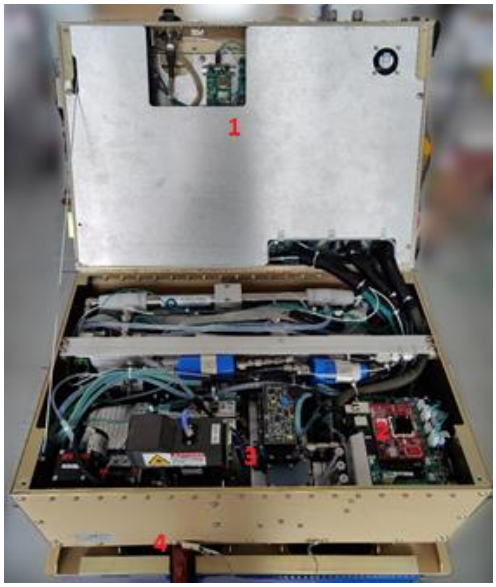

Figure 20. Picture of the full assembled instrument package. With (1) shielded Main Board and electronics, (2) CAPS boards, (3) Ventilation between the MAGIC CPC and POPS and (4) the main ventilation.

Figure 20 shows the package in its final stage as it was assembled in our laboratory. All tubes, cables and instruments are built up and connected. The main electronic components are shielded with a metal plate, but the instrument picture gives an impression of the compactness of the set up. There is almost no space left, which required to carefully assemble all parts.

An additional problem is the heat development, that was solved by the external ventilation and two ventilators dedicated to the heatsink of the MAGIC Peltier elements and the CAPS electronics. The system was tested with four thermistor elements at critical positions, like the main board or near the condensation particle counter.

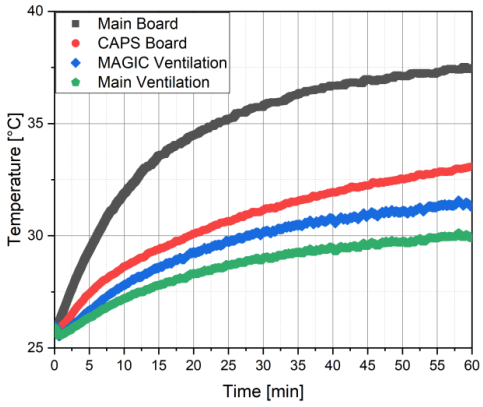

Figure 21. Heat development inside the Instrument Package 2e at different locations.

Figure 21 shows the temperature of four different zones inside the P2e package during the first hour of operation. The different temperature zones reached their plateau after 60 min. It is essential, that the temperature around the MAGIC device stays below 33°C, since the internal Pelletier based cooling system can only provide a temperature difference of around 30°C. It is possible to increase all temperature setpoints of the MAGIC-LP by 3 K, without changing the activation efficiencies.

A detailed characterisation of each individual instrument device and the whole system will be described in the coming sections. Additionally, the reference systems and instruments are described.

7 Qualification of the CAPS Instrument

Laboratory experiments were largely conducted on a measurement set-up, that has to be intensively characterised and controlled. For the laboratory study as well for the ambient measurements, an immersive number of parameters were recorded including housekeeping data: For each instrument this were at least five parameters, that served to ensure good data quality. These parameters range from temperature to internal flow control. To sum it up, for each experiment conducted, over 70 parameter timeseries are stored with a time resolution of one hertz. To exclude errors and to avoid misinterpret data, all parameters are controlled to stay within their predefined ranges. To name a few examples: temperature settings of the Condensation particle counters, flow control parameters and baseline values. This standard was already looked at and applied during the experimental run, so the amount of dataset, that must be excluded is minimised.

In this section the laboratory setup of the test stand for optical particle properties is introduced in detail. Starting with the particle production, process treatment, data processing, correction as well as data inversion. The steps for error analysis are stated and finally the main results for the

laboratory set up and measurement uncertainties are unfolded. Later on, the flight simulation test stand is described in detail and the characterisation of a water-based condensation particle counter.

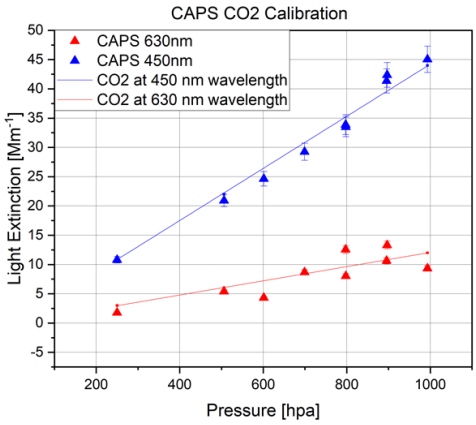

Figure 22. Calibration of the CAPS instruments with a high span gas.

The first check-up for the CAPS instruments was a calibration with CO_2. It is known that CO_2 has a scattering coefficient of 71.83 Mm^{-1} below standard conditions and at 450nm wavelength and "standard" air with no particles a scattering coefficient of 27.61 Mm^{-1}. This results in an difference of 44.2 Mm^{-1} that is to be achieved for 1013 hPa, when a baseline is done with filtrated air [61]. The CAPS PMex equipped with a wavelength of 630 nm had high variance. This can be explained, since the mirrors of the red CAPS were unfortunately highly polluted during these measurements.

The second calibration can be done with polysterene latex particles and Mie calculations using size distribution by means of an OPC which can also be called as a closure study. Those calibration measurements were performed with a variation of different particle- sizes and particle-concentrations. Several of those measured aerosol light extinction values are compared against calculated values, with the particle number concentration measured by an optical particle counter (SKY-OPC; Grimm). Those measurements were performed for both CAPS PMex wavelengths and compared with a second set up of instruments in the optical aerosol line. As can be seen in Figure 23, the CAPS PMex agree with the Mie calculated aerosol light extinction coefficients with a slope of 1.01 ±0.03.

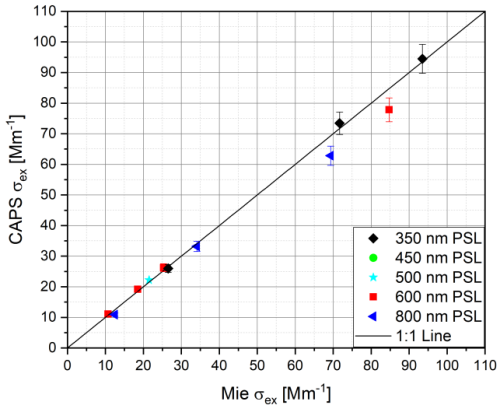

Figure 23. Intercomparison of aerosol light extinction coefficient measured by the CAPS PMex and Extinction coefficients derived by Mie theory using Size distribution measurements of the OPC. (Closure study)

The CAPS calibration should always be done with multiple approaches to approve the geometric correction factor that has to be applied in the instrument software or as a post calibration factor.

7.1 Aerosol Optical Properties Calibration Set-up

This chapter is based on the publication by Weber, et al. published in the Atmos. Meas. Tech. journal (2022).

The article shows the importance of multiwavelength characterisations and the robustness of the measurement of the aerosol light extinction by the CAPS and the derived parameters such as the extinction Ångström exponent. In addition, even when optical closure can be obtained, the need for a light absorption measurement is an indispensable parameter for the calculation of the absorption Ångström exponent. The focus was on the accuracies and uncertainties of the individual coefficients for aerosol light extinction, scattering and absorption. Furthermore, the single scattering albedo and the Ångström exponents were examined. All these parameters were obtained by a single instrument approach or by a set of instruments. Later, it became clear, that the Ångström exponent for aerosol light absorption has the largest uncertainties and should only be obtained by a single instrument approach to reduce errors.

7.1.1 Background and used techniques

The precise determination of aerosol optical properties is crucial for the provision of reliable input data for chemistry transport models, climate models, and radiative forcing calculations [76]. This applies, in particular, to light-absorbing particles like black carbon [11], which are produced by

incomplete combustion processes and absorb visible light very efficiently. Aerosol light absorbing properties are also relevant for source appointment studies and the determination of anthropogenic influences on atmospheric aerosols [77]. There are two common methods to generate aerosol light absorption values for long-term and short-term monitoring, each with its own disadvantages. One method is a filter-based technique, which operates by deriving light absorbing values from the attenuation of light through particle-loaded filters [78]. A disadvantage of all filter-based methods is linked to artifacts like multiple scattering inside the filter matrix, shadowing of light-absorbing particles in highly loaded filters, and humidity effects on the filter substrate [79]. Widely deployed filter-based light absorption instruments include the Particle Soot Absorption Photometer (PSAP [62]), the Tri-color Absorption Photometer (TAP), the Continuous Light Absorption Photometer (CLAP [80], the Aethalometer [81], and the Multi-Angle Absorption Photometer (MAAP) [82]. The PSAP, TAP, CLAP, and Aethalometer share their measurement principle, utilize a reference spot technique, and require complex correction algorithms [83-85]. The MAAP utilizes a different approach, a two-stream radiative transport model, made possible by its measurement of both direct transmission and back scatter from the particle loaded filter substrate. Another method for deriving aerosol light absorption is the differential method, based on the subtraction of light scattering from extinction. This method is commonly conducted by comparing measurements from two separate instruments which results in large precision errors particularly for low light absorption and/or high single scattering albedo (SSA) values. In laboratory studies, however, the differential method is widely used as a reference technique because the applied light scattering and extinction instruments make measurements on freely floating particles (i.e., no filter-based artifacts) and are well characterised [62, 63, 86]. A significant improvement of aerosol measurement capacities is achieved by the recently developed Cavity Attenuated Phase Shift particle monitor for single scattering albedo (CAPS PM_{SSA}) [56], which is able to measure light extinction and scattering simultaneously and is the focus of recent studies [87 60].

Our study contributes to this topic with a detailed optical closure study, in which we deploy standard and advanced instrumentation for measuring aerosol optical properties and sample mixtures of light absorbing and scattering aerosol to assess method uncertainties and precision errors.

7.1.2 Experimental Approach on Aerosol Optical Properties

A schematic of the experimental setup is shown in Figure 24. Briefly, aerosol flows, generated using two nebulizers or an inverted flame generator, are dehumidified (generally to below 7%) using diffusion driers filled with silica gel and sent to a mixing chamber to ensure homogeneous mixing, prior to being sampled using a suite of optical instruments. In order to avoid particle losses caused by electrostatic forces, all tubing and chambers are constructed of either stainless steel or conductive silicone tubing. The individual optical instruments are connected using an iso-axial orientated and isokinetic operated nozzle located in the centreline of the supply line. As shown in Figure 24, aerosol production was controlled by multiple Mass Flow Controllers (MFC, Bronkhorst High-Tech B.V., Ruurlo, Netherlands). A Labview based program controlled the complete measurement system and centrally recorded all data from the individual instruments.

Pressures in the aerosol delivery lines were always maintained at that of the ambient atmosphere. Aerosol flow rates to the individual instruments were provided at their specified levels (0.6 - 3.0 lpm) except for that of the TSI nephelometer. Given the limitations of the aerosol supply system, the flow to the nephelometer was reduced from 20 lpm to 2.2 lpm, causing the physical response time of that instrument to be increased to ten minutes. Complete details of the generation of aerosols are provided in the following section.

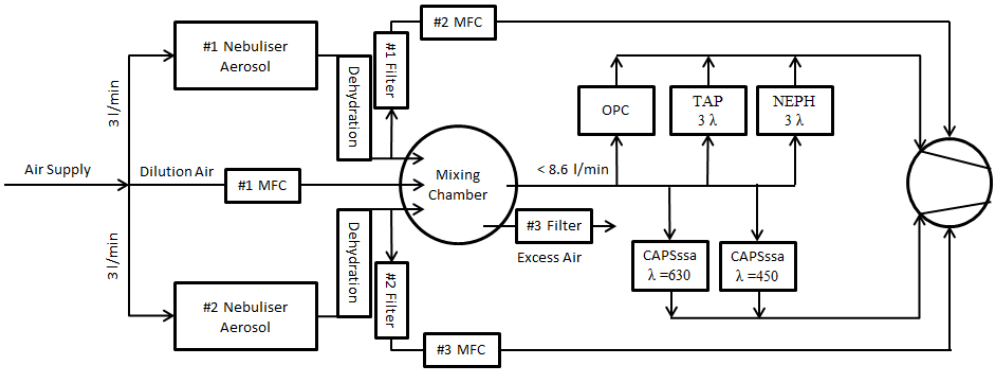

Figure 24. Experimental setup for the measurements. Flame soot measurements were done with a combustion flame source replacing #2 Nebuliser.

The generated aerosol size distributions were characterized and monitored with either a Scanning Mobility Particle Sizer (SMPS) composed of the combination of a Differential Mobility Analyzer (DMA 5.400, Grimm Aerosol Technik GmbH Co & KG Germany) and a Condensation Particle Counter (CPC 5.411, Grimm Aerosol Technik) system in a sequential mode of operation or a Grimm optical particle size spectrometer (SKY-OPC, model 1.129, Grimm Aerosol GmbH & Co. KG, Ainring, Germany).

7.1.3 Optical Instruments and Uncertainties

The suite of optical instruments used in this study included the following instruments. The particle scattering coefficient, σ_{sp}, was measured with an integrating multi wavelength nephelometer (NEPH, Model 3563, TSI Inc., Shoreview, MN, USA; [88] and with the scattering channel of the CAPS PM_{SSA} monitor [89] (CAPS PM_{SSA}, Aerodyne Research Inc., Billerica, MA, USA) which is derived from a measurement of the total extinction and single scattering albedo. For the particle light absorption coefficient, σ_{ap}, we used the Tricolor Absorption Photometer (TAP (Brechtel Inc., Hayward, CA, USA), which is based on the well-known Particle Soot Absorption Photometer (PSAP, ARM Research) and the Continuous Light Absorption Photometer (CLAP) developed by NOAA [90]. The particle light extinction coefficient, σ_{ep}, was directly measured with the phase shift channel of the CAPS PM_{SSA} monitor.

The light extinction channel of the CAPS instrument has an uncertainty of 5% and a precision of 2% and a scattering uncertainty of 8% and 2% precision, respectively [89]. The TAP has an uncertainty of around 8%, with a precision of 4% ([90, 91], while the NEPH has an uncertainty of less than 10% and a precision of about 3% [92] [93]. These literature-derived uncertainty estimates for measurement accuracy will be used in this study for instrument closure, either directly or via error propagation. Individual point averages will be shown with corresponding precision variances.

7.1.4 Aerosol Generation for Aerosol Optical Property Measurements

Table 2 provides a complete list of all aerosol types used in the study. Solutions of known concentrations of Aquadag (AQ, Aqueous Deflocculated Acheson Graphite; Acheson Industries, Inc., Port Huron, MI, USA), Cabot Black (BC) and Magic Black (MB), an acrylic based paint, were prepared on a daily basis by ultra-sonication before nebulization in a Constant Output Atomizer (Model 3076, TSI Inc.). The count median diameter (CMD) and geometric standard deviation (GSD) of the ammonium sulphate nebulized by the constant output atomizer depends on the concentration of the salt solution and the flow through the atomizer. Use of constant flow rates and particle concentrations produced constant size distributions [94]. The inverted flame soot generator (Argonaut Scientific Corporation, Edmonton, AB, Canada) was operated with a pre-determined propane to oxidation air ratio of 7.5 litre per minute air to 0.0625 litre per minute propane so that the flame produced a stable and low organic carbon soot. It has previously been shown that at least 30 min were necessary for the Argonaut flame to reach stable aerosol concentrations [95, 96].

Initially, pure aerosol types were generated independently and measured to quantify their size distributions and optical properties. The main part of the study was focused on making external mixtures of ammonium sulphate and each of the absorbing particle types, separately. These mixtures were controlled to provide a stable aerosol with varying intensive optical properties.

Table 2. Overview of aerosol types used

Substance	Aerosol type	Acronym	Shape
Ammonium Sulphate	salt	AS	spheroidal
Aquadag	colloidal graphite	AQ	compact aggregates
Cabot Black (Regal 400R)	powder	BC	compact agglomerates
Flame Soot	combustion aerosol	Soot	fractal agglomerates
Magic Black (Acrylic paint)	organic pigments	MB	unknown

7.1.5 Data Treatment, Instrument Corrections and Calibrations

The CAPS PM_{SSA} instrument extinction channel was calibrated using polystyrene latex beads (PSL) particles as a reference standard and Mie theory using a BHMIE Python code derived from Bohren & Hoffman (1983) [27]. Additionally, the 450 nm wavelength CAPS PM_{SSA} calibration was validated using measurements of CO_2 Rayleigh scattering. The scattering channel of the CAPS PM_{SSA} was internally adjusted to the extinction channel using ammonium sulphate as a light-scattering aerosol, assuming a single scattering albedo of 1.0. A truncation error correction was not necessary regarding the size of the aerosols used [97], since all the aerosols used had median diameter smaller than 200 nm. The CAPS PM_{SSA} monitor, which is subject to baseline drift as the system heats up, stabilized after 30 min of operation [98].

The integrating Nephelometer (NEPH) was calibrated using CO_2 [60, 92]. Truncation corrections were made using the approaches developed by Anderson and Ogren [92] for purely scattering aerosols and by Massoli [93] for aerosol mixtures containing light absorbing particles. The truncation corrections applied were always equal to or less than 5%. Because of the reduced air flow, the NEPH needed at least 15 minutes to reach a stable plateau after changing aerosol generation settings.

A new filter spot for the TAP was selected for each measurement in order to minimize measurement uncertainties due to particle loaded filters. The first correction regarding truncation is done by the included software. The software has the capability to choose the Ogren [92] correction scheme based on the filter type used (Quartz Fibre, BT-TAP-FIL100, ENVILYSE). Further corrections were made according to Virkkula [84, 99].

Table 3. List of instruments and used properties.

Instrument	Manufacturer	Properties	λ (nm)
CAPS PM_{SSA}	Aerodyne Research Inc.	σ_{ep}; σ_{sp}	450; 630
NEPH	TSI Inc.	σ_{sp}	450; 550;700
TAP	Brechtel Inc.	σ_{ap}	467; 530; 660

Aerosol Optical Properties derived from primary measurements

The extensive parameters for aerosol light interactions are extinction, scattering and absorption. When two of them are known, the missing one can be calculated with the help of this equation:

$$\sigma_{ep} = \sigma_{sp} + \sigma_{ap} \quad \text{EQ 30}$$

where σ_{ep} is the extinction coefficient, σ_{sp} the light scattering coefficient and σ_{ap} the coefficient for light absorption by particles. The unit of all these parameters is Mm^{-1} ("inverse Mega meters"; 1 Mm^{-1} = 10^{-6} m^{-1}). When solving EQ 30 for σ_{ap}, it is possible to derive the absorption coefficient by combining CAPS PM_{SSA} extinction measurements with either CAPS PM_{SSA} or NEPH scattering

measurements [σ_{ap}(CAPS, CAPS) or σ_{ap}(CAPS, NEPH)] for comparison. In the following, this will be called the Differential Method (DM).

To calculate the Single Scattering Albedo (SSA), the particle light scattering must be divided by the particle light extinction:

$$SSA(\lambda) = \frac{\sigma_{sp}}{\sigma_{ep}} \quad \text{EQ 31}$$

The Ångström exponents (AE) are calculated from:

$$xAE = -\frac{\log\left(\frac{\sigma_{xp}(\lambda 1)}{\sigma_{xp}(\lambda 2)}\right)}{\log\left(\lambda 1/\lambda 2\right)} \quad \text{EQ 32}$$

By solving EQ 32 for $\sigma_p(\lambda 1)$ and assuming a valid Ångström exponent the resulting equation EQ 33 is used for wavelength adjustments

$$\sigma_{xp}(\lambda 1) = \sigma_{xp}(\lambda 2) \cdot \left(\frac{\lambda 1}{\lambda 2}\right)^{-AE} \quad \text{EQ 33}$$

For the particle coefficient σ_{xp}, the corresponding σ_{sp}, σ_{ep}, or σ_{ap} can be put into calculations EQ 32 to obtain the absorption Ångström exponent (AAE), extinction Ångström exponent (EAE) and scattering Ångström exponent (SAE), accordingly.

The error propagation is determined by Gaussian error propagation:

$$SSA(\lambda, \sigma_{sp}, \sigma_{ep}) = \frac{\sigma_{sp}}{\sigma_{ep}} \xrightarrow{yields} \Delta\text{SSA}\,(\lambda, \sigma_{sp}, \sigma_{ep}) = \sqrt{\left(\frac{1}{\sigma_{ep}} \cdot \Delta\sigma_{sp}\right)^2 + \left(\frac{\sigma_{sp}}{\sigma_{ep}^2}\Delta\sigma_{ep}\right)^2} \quad \text{EQ 34}$$

$$SSA(\lambda, \sigma_{sp}, \sigma_{ap}) = \frac{\sigma_{sp}}{\sigma_{ap+\sigma sp}} \xrightarrow{yields} \Delta\text{SSA}\,(\lambda, \sigma_{sp}\sigma_{ap}) = \quad \text{EQ 35}$$

$$\sqrt{\left(\frac{\sigma_{sp}}{(\sigma_{ap+\sigma_{sp}})^2} \cdot \Delta\sigma_{sp}\right)^2 + \left(\frac{\sigma_{ap}}{(\sigma_{ap+\sigma_{sp}})^2} \cdot \Delta\sigma_{ap}\right)^2}$$

$$AE = -\frac{\log\left(\frac{\sigma_{xp}(\lambda 1)}{\sigma_{xp}(\lambda 2)}\right)}{\log\left(\lambda 1/\lambda 2\right)} \xrightarrow{yields} \Delta AE = \quad \text{EQ 36}$$

$$\sqrt{\left(\frac{-1}{\log\left(\lambda 1/\lambda 2\right) \cdot \sigma_p(\lambda 1)} \cdot \Delta\sigma_{xp}(\lambda 1)\right)^2 + \left(\frac{1}{\log\left(\lambda 1/\lambda 2\right) \cdot \sigma_{xp}(\lambda 2)} \cdot \Delta\sigma_p(\lambda 2)\right)^2}$$

where $\sigma_{xp} = \{\sigma_{ep}, \sigma_{sp,}\sigma_{ap}\}$

Those equations can be expanded, if the instruments are not calibrated properly, as Sherman [100] proposed, but the equations are in accordance with the BIPM (Bureau International des Poids et Mesures)

Data Averaging

For each experiment run, a different aerosol mixture was generated with different optical properties and allowed to reach steady state, including a waiting period of approximately 15 minutes due to the slow time response of the low flow NEPH. At steady state conditions, we measured that the size and optical properties fluctuating less than 2% over time with the OPC, CAPS PM_{SSA}, and NEPH. All instruments recorded data at a 1 second rate. Reported data points

are given as averages of 100 seconds of stable aerosol production. This value was chosen to obtain a minimum in data precision and detection limits as determined from Allan Standard Deviation plots by Massoli [57] for the CAPS extinction measurements and Ogren [90] for filter-based absorption measurements. Averaging for longer periods would only increase variances due to transmission (TAP) and baseline drift (CAPS).

7.1.6 Aerosol Optical Property Measurements

Pure aerosol types

The measured size parameters and calculated intensive parameters of the pure aerosol types are summarized in Table 4. The errors reported in Table 4 are calculated from error propagation. The size distributions of the different aerosol types were measured with a Grimm SMPS and are shown in Figure 25 are set to 1000 particles per cubic centimetre. The Ångström exponents for the pure substances fall within typical ranges for these types of aerosols and size distributions reported in literature. For example, the SAE decreases from a value of 3.22 for 40 nm AS particles which is close to the SAE value of 4.0 for air molecules with increasing particle diameter. Thus, the SAE drops to 0.76 for 130 nm compact AQ particles but increases to 0.99 for 140 nm fractal agglomerate soot. The shape of AQ is assumed to be more compact than the soot agglomerates, such that their scattering and electrical mobility behaviours are dependent mainly upon their physical diameters. In contrast, the scattering behaviour of the fractal soot agglomerates is due mainly to the distribution of primary particles, whereas their electrical mobility diameter is more dependent upon the major axis of the agglomerate. As expected by EQ 33, the SSA increases with decreasing wavelength [27]. The AAE for fractal combustion soot is close to 1.0 as reported for the mini-CAST soot generator [101].

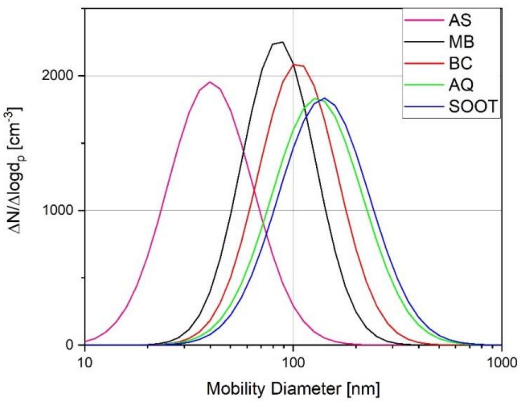

Figure 25. Measured size distributions by SMPS for the pure aerosol types used, set to an assumed total concentration.

Table 4. Overview of the measured intensive optical properties of the pure aerosol types.

	AS	MB	BC	AQ	Soot
Count Median Diam.	40 nm	85 nm	105 nm	130 nm	140 nm
Geometric Standard Deviation	1.60	1.50	1.55	1.65	1.65
SSA 630 (NEPH, CAPS)	1.0	0.85 ± 0.02	0.26 ± 0.03	0.37 ± 0.03	0.20 ± 0.02
SSA 450 (NEPH, CAPS)	1.0	0.92 ± 0.07	0.32 ± 0.04	0.44 ± 0.02	0.26 ± 0.08
SAE (630/450) (NEPH)	3.22 ± 0.09	2.16 ± 0.37	1.71 ± 0.13	0.76 ± 0.06	0.99 ± 0.08
AAE (630/450) (TAP)	-	1.34 ± 0.12	1.16 ± 0.03	0.44 ± 0.02	1.08 ± 0.02
EAE (630/450) (CAPS)	3.21 ± 0.08	2.03 ± 0.38	1.43 ± 0.65	0.52 ± 0.10	1.10 ± 0.10

Extensive Parameters of Aerosol Mixtures

First, the extensive parameters must be validated for all instrument combinations to ensure the reliability of the intensive parameters derived from them. We have chosen to use external mixtures of AS and AQ particles for these studies as they are both readily atomized, generating highly stable aerosols for the necessary time periods for averaging. We note that AQ absorbing aerosols are commonly used as a reference material for instrument comparisons [30]. The results for mixtures of AS with the other absorbing aerosol types are included in Table 6 -Table 9.

The two CAPS PM_{SSA} monitors (450 nm and 630 nm wavelengths) measured the extinction coefficient of particles directly with a small precision error of around 2% [60]. In Figure 26, we show scatter plots of these direct extinction coefficient measurements (X-axis) in comparison to the absorption coefficient measured using TAP and the scattering coefficient measured using NEPH combined using Equation EQ 30 in the form: $\sigma_{ep}(NEPH, TAP) = \sigma_{ap}(TAP) + \sigma_{sp}(NEPH)$ (y-axis) for wavelengths of 450 nm (right panel) and 630 nm (left panel).

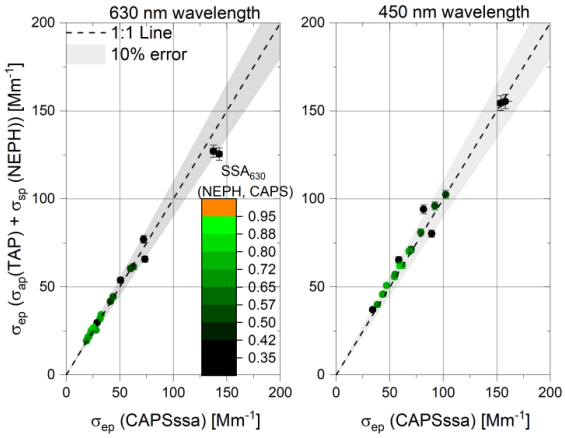

Figure 26. Scatter plots of the extinction coefficients for different AQ-AS external mixtures at 630 nm (left) and 450 nm wavelengths (right). The y-axes show the extinction coefficients derived by combining TAP absorption and NEPH scattering coefficients versus the CAPS PM_{SSA} monitor direct extinction coefficient measurements. The colour code represents the SSA of the analysed mixed aerosol measured at 630 nm wavelength. In addition, an error band of ±10% was added to the 1:1 line.

Here, the measured 630 nm SSA colour code serves as a proxy for the mixing ratio of the external mixtures of nebulized AQ and AS particles. The measured 630 nm and 450 nm extinction coefficients align with the 1:1 line within 10% across a broad range of extinction values as well as SSA values, ranging from 0.3 to close to 1. The 10% was chosen to show the fulfilment of the requirements for monitoring systems [102] for aerosol properties. This shows that the instruments are not sensitive to the SSA of the particle type used at either wavelength of interest.

The measured scattering coefficients at 450 and 630 nm wavelengths are compared using scatterplots for the different techniques in Figure 27. Here, we use the NEPH and the integrating sphere channel of the CAPS PM_{SSA} instrument capable of measuring the scattering coefficient directly. In addition, we calculated the scattering coefficients using a Differential Method (DM), solving EQ 30 for the scattering coefficient by subtracting the absorption coefficient measured by the TAP from the extinction coefficient measured by CAPS PM_{SSA}. The NEPH is used as reference because it has well proven correction functions for light absorption particles, as described in Section 2.4.1.

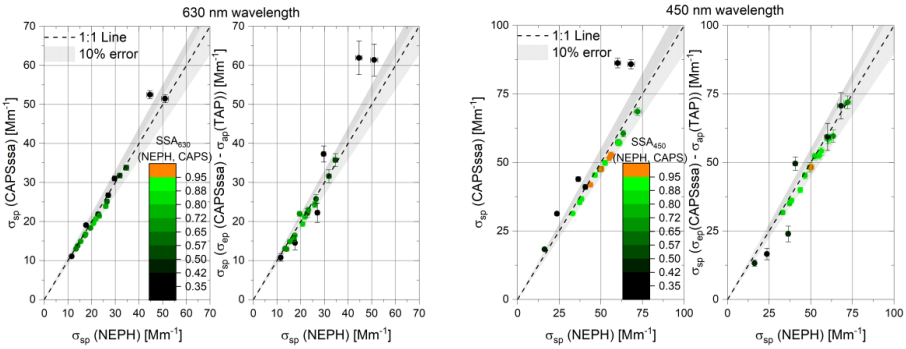

Figure 27. Comparisons of measured light scattering coefficients at 450 nm and 630 nm wavelengths for mixtures of AQ and AS aerosols. The y-axes show the CAPS PM_{SSA} (integrating sphere) or the Differential Method (CAPS extinction minus TAP absorption) scattering versus NEPH scattering measurements at 450 nm and 630 nm wavelengths. The colour code represents the SSA value of the measured aerosol mixture. An error band of ±10% was applied to the 1:1 line. Error bars shown represent instrument precisions (1 σ).

The measured scattering coefficients at both 450 nm and 630 nm wavelengths agree within 10% for the majority of measurements. There is no apparent dependence of measured scattering coefficients with scattering coefficient magnitude (over the range measured) nor with aerosol SSA, an indicator of the external mixing ratio. Several outliers are visible, particularly for points with SSA values around 0.35, indicating nearly pure AQ aerosols. For the scattering coefficients derived using the Differential Method (CAPS extinction minus TAP absorption), some of the scatter may be due to the larger uncertainties associated with the filter-based absorption measurements, as discussed in the Reno Study [63]. The outliers in the CAPS vs NEPH plots, especially at 450 nm wavelength, are currently unexplained and are likely due to apparent stability issues for these points.

Particle light absorption coefficient measurements are the most complicated, as none of our optical instrument techniques directly measure absorption. We have two methods for measuring absorption coefficients: (1) Differential Method following EQ 30, using either $\sigma_{ap}(CAPS,NEPH) = \sigma_{ep}(CAPS) - \sigma_{sp}(NEPH)$ or $\sigma_{ap}(CAPS,CAPS) = \sigma_{ep}(CAPS) - \sigma_{sp}(CAPS)$; and (2) filter-based TAP measurements. As the filter-based method requires the application of multiple, empirical correction schemes, we have chosen $\sigma_{ap}(CAPS,NEPH)$ as the reference for the comparison of the $\sigma_{ap}(TAP)$ and $\sigma_{ap}(CAPS,CAPS)$ values.

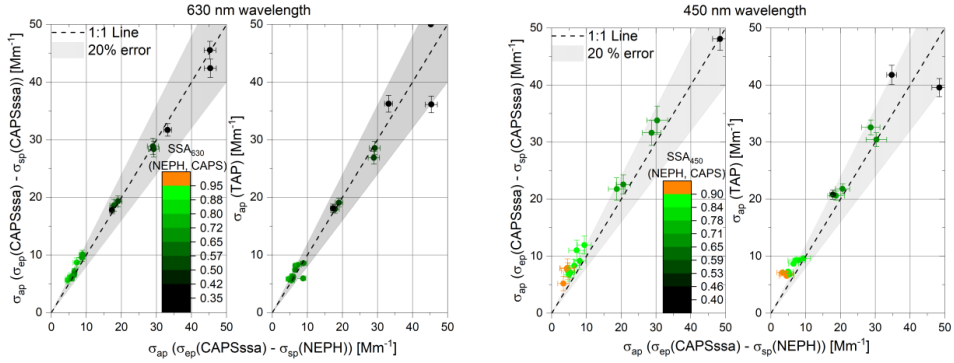

Figure 28. Scatter plots of measured 450 nm and 630 nm wavelength absorption coefficients of external mixtures of AQ and AS for different instrument combinations. The colour code represents the SSA value of the respective data point. An error band of ±20% was applied to the 1:1 line, which is required for monitoring systems [102] for light absorption measurements. Error bars shown represent propagated instrument precisions (1 σ).

In Figure 28, the light absorption measurements at wavelengths of 450 nm and 630 nm are compared. We chose to include 20% error bands for these comparisons, though the overall uncertainty for filter-based absorption measurements is often estimated to be 30% [62]. Most of the data points shown fall within the 20% error band, with some exceptions for aerosols with low absorption and high SSA values.

Table 5. Linear regression results of scattering, σ_{sp} , extinction, σ_{ep}, and absorption, σ_{ap}, for external mixtures of AQ and AS particles, given as slopes (m), Pearson R, and y-axis intercepts (b).

	σ_{sp} (CAPS) vs. σ_{sp} (NEPH)	$\sigma_{sp(CAPS,TAP)}$ vs. $\sigma_{sp(NEPH))}$	$\sigma_{ep(NEPH,TAP)}$ vs. $\sigma_{ep(CAPS)}$	$\sigma_{ap(TAP)}$ vs. $\sigma_{ap(CAPS,NEPH)}$
630 nm				
m	1.07 ± 0.03	1.08 ± 0.05	0.99 ± 0.03	0.92 ± 0.07
R	0.99	0.97	0.99	0.95
b [Mm^{-1}]	-1.84 ± 0.57	-2.15 ± 1.12	0.91 ± 0.93	0.78 ± 0.68
450 nm				
m	0.99 ± 0.05	1.06 ± 0.03	0.98 ± 0.03	1.04 ± 0.08
R	0.97	0.99	0.99	0.96
b [Mm^{-1}]	1.14 ± 2.27	-4.60 ± 1.51	3.37 ± 1.71	2.13 ± 0.64

The high Pearson correlation (R > 0.95) coefficients in Table 5 indicate that the correlations are highly linear. The primary focus for this study was to have most of the experimental runs exhibit light extinctions between 5 Mm^{-1} and 150 Mm^{-1}, representative of atmospheric conditions. The slopes are all close to unity within the expected errors ranges, or at least single instrument uncertainty, indicating closure has been achieved for these optical measurements. Thus, the extensive parameters can be trusted for instrument comparison, especially for the light scattering and light extinction information. We provide regression analyses for all other absorbing aerosol types externally mixed with AS in Table 8 and Table 10.

Excellent agreement (R>0.97) is shown for σ_{sp} measurements of the NEPH and the CAPS PM_{SSA} scattering channel, indicating that the CAPS PM_{SSA} scattering channel can be considered as a substitute for the nephelometer scattering measurement. Trade-offs in the CAPS PM_{SSA} versus NEPH comparison include the three wavelengths and backscatter measurements of the NEPH versus the single wavelength of the CAPS PM_{SSA}, countered by the additional extinction measurement of the CAPS PM_{SSA} allowing for absorption and SSA values to be simultaneously measured.

In addition to regression analyses, where outliers and/or high values can dominate the fitted slope of the regression, another statistical approach is to investigate the ensemble averaged instrumental ratios (σ_{ap} (instrument #1) / σ_{ap} (instrument #2)), which is more sensitive to errors at low values. Resulting 630 nm and 450 nm wavelength absorption coefficient ratios are tabulated in Table 6 and Table 7, respectively. The average ratios are calculated from the points shown in Figure 28 for AQ and AS mixtures and from results obtained for the other absorbing particle types externally mixed with AS particles.

Table 6. Ensemble average ratios of σ_{ap} (TAP) / σ_{ap} (CAPS, NEPH) at 630 nm wavelength. N denotes the number of experiments used for the average.

630 nm wavelength	BC	AQ	SOOT	MB
σ_{ap} (TAP) / σ_{ap} (CAPS,NEPH)	1.22 ± 2.57 (N=36)	0.97 ± 0.22 (N=28)	1.10 ± 1.22 (N=25)	0.88 ± 0.17 (N=8)
σ_{ap} (TAP) / σ_{ap} (CAPS,NEPH) for samples with σ_{ap} >10 Mm^{-1}	1.08 ± 0.19 (N=24)	0.94 ± 0.10 (N=11)	0.86 ± 0.13 (N=6)	-

Table 6 demonstrates that the light absorption values agree for the different methods in general. With an ensemble average for the ratio σ_{ap} (TAP) / σ_{ap} (CAPS,NEPH) of 0.97 ± 0.22, good agreement is confirmed with over 60% of all datapoints for external mixtures of AQ and AS falling within a range of σ_{ap} (TAP) / σ_{ap} (CAPS,NEPH) = (0.8 – 1.2). These results support the linear

regression results in Table 7, though exhibit larger scatter due to the greater sensitivity to small errors at low values.

The average ratios for other externally mixed absorbing aerosol types deviate more from unity than AQ mixtures. Most of this scatter can be ascribed to the greater sensitivity of the ratio to small errors at low values. By filtering these ratios for points with $\sigma_{ap} > 10$ Mm^{-1}, approximately 80% of the data are within the range of 0.8-1.2, The ratios for $\sigma_{ap} < 10$ Mm^{-1} exhibited almost no modal value in the relative frequency distributions, confirming that scatter in low values significantly affects the average ratios.

Table 7. Ensemble average ratios of σ_{ap} (TAP) / σ_{ap} (CAPS, NEPH) at 450 nm wavelength. N denotes the number of experiments used for the average.

450 nm wavelength	BC	AQ	SOOT	MB
σ_{ap} (TAP) / σ_{ap} (CAPS,NEPH)	1.03 ± 1.72 (N=36)	1.06 ± 0.38 (N=28)	0.89 ± 1.05 (N=25)	1.28 ± 2.91 (N=8)
σ_{ap} (TAP) / σ_{ap} (CAPS,NEPH) for samples with σ_{ap} >10 Mm^{-1}	1.08 ± 0.33 (N=24)	1.01 ± 0.13 (N=11)	0.84 ± 0.27 (N=6)	-

Repeating this analysis for 450 nm wavelength, the light extinction and scattering of smaller particles increases compared to the values at 630 nm wavelength. As a result, the errors in calculating the 450 nm wavelength absorption coefficients from the Differential Method also increase. As demonstrated in Table 7, only the variance for the ratio σ_{ap} (TAP) / σ_{ap} (CAPS, NEPH) for compact AQ particles was less than 1 (i.e., <100%), with over 50% of the data being within the range of 0.8-1.2. All ensemble average ratios were close to 1; however, with an associated error of up to ±1.7 (i.e., ±170%), these values are not significant, which means that the ratios scatter widely with no clear modal value. Again, filtering the 450 nm data for σ_{ap} >10 Mm^{-1} greatly improves the results, with ratios σ_{ap} (TAP) / σ_{ap} (CAPS, NEPH) =1.08 ± 0.33 for BC. The best instrumental ratio of 1.01 ± 0.13 is shown for AQ mixtures in Table 6 at 450 nm wavelength.

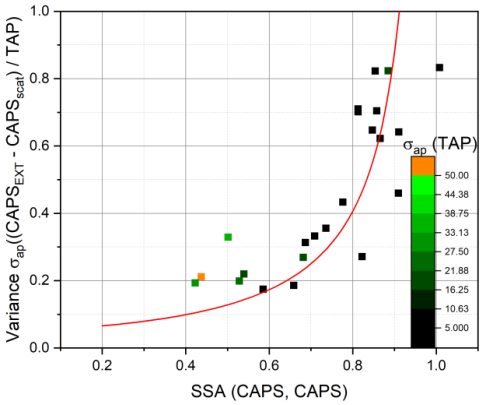

Figure 29. Variance of the measured absorption coefficients [σ_{ap} (CAPS, CAPS)) / σ_{ap} (TAP)] for Differential Method calculations relative to TAP measurements for AQ and AS external mixtures. The ratios are plotted against the aerosol measured SSA values [SSA(CAPS, CAPS)]. The red line represents the calculated relative errors using Gaussian error propagation of the uncertainties of the DM Method with 1 as 100%..

In order to demonstrate the dependency of the uncertainties associated with the Differential Methods for deriving σ_{ap} values on the SSA, the ensemble variance ratios of σ_{ap} (CAPS, CAPS) / σ_{ap} (TAP) are shown as functions of SSA in Figure 29. For SSA values greater than 0.9, light absorption coefficients derived for the DM methods have propagated uncertainties over 100% independently of their load. The experimental data align within these calculated relative uncertainties.

Table 8. Linear regression results of scattering, σ_{sp}, extinction, σ_{ep}, and absorption, σ_{ap}, coefficients for external mixtures of BC and AS particles, given as slopes (m), Pearson R, and y-axis intercepts (b).

BC	$\frac{\sigma_{sp(CAPS)}}{\sigma_{sp(NEPH)}}$	$\frac{\sigma_{sp(CAPS,TAP)}}{\sigma_{sp(NEPH)}}$	$\frac{\sigma_{ep(TAP,NEPH)}}{\sigma_{ep(CAPS)}}$	$\frac{\sigma_{ap(TAP)}}{\sigma_{ap(CAPS,NEPH)}}$
630 nm				
m	1.02 ± 0.03	0.99 ± 0.05	0.94 ± 0.02	0.90 ± 0.02
R	0.98	0.96	0.99	0.99
b [Mm^{-1}]	-0.69±0.7	-2.13 ± 1.01	3.59 ± 0.60	2.57 ± 0.11
450 nm				
m	0.99 ± 0.02	1.06 ± 0.06	0.94 ± 0.03	0.86 ± 0.05
R	0.99	0.95	0.98	0.97
b [Mm^{-1}]	5.36 ± 1.45	-0.59 ± 3.86	0.97 ± 3.17	2.98 ± 0.48

Table 9. Linear regression results of scattering, σ_{sp}, extinction, σ_{ep}, and absorption, σ_{ap}, coefficients for external mixtures of SOOT and AS particles, given as slopes (m), Pearson R, and y-axis intercepts (b).

SOOT	$\frac{\sigma_{sp(CAPS)}}{\sigma_{sp(NEPH)}}$	$\frac{\sigma_{sp(CAPS,TAP)}}{\sigma_{sp(NEPH)}}$	$\frac{\sigma_{ep(TAP,NEPH)}}{\sigma_{ep(CAPS)}}$	$\frac{\sigma_{ap(TAP)}}{\sigma_{ap(CAPS,NEPH)}}$
630 nm				
m	1.06 ± 0.04	0.9 ± 0.20	0.99 ± 0.08	0.76 ± 0.11
R	0.99	0.74	0.97	0.92
b [Mm^{-1}]	0.05 ± 0.56	1.57 ± 3.21	1.80 ± 1.72	3.93 ± 1.68
450 nm				
m	0.81 ± 0.03	0.77 ± 0.07	0.92 ± 0.04	0.70 ± 0.10
R	0.99	0.97	0.98	0.91
b [Mm^{-1}]	1.73 ± 0.45	2.64 ± 0.91	3.26 ± 2.24	1.75 ± 0.82

Table 10. Linear regression results of scattering, σ_{sp}, extinction, σ_{ep}, and absorption, σ_{ap}, coefficients for external mixtures of MB and AS particles, given as slopes (m), Pearson R, and y-axis intercepts (b).

MB	$\frac{\sigma_{sp(CAPS)}}{\sigma_{sp(NEPH)}}$	$\frac{\sigma_{sp(CAPS,TAP)}}{\sigma_{sp(NEPH)}}$	$\frac{\sigma_{ep(TAP,NEPH)}}{\sigma_{ep(CAPS)}}$	$\frac{\sigma_{ap(TAP)}}{\sigma_{ap(CAPS,NEPH)}}$
630 nm				
m	0.96 ± 0.03	1.05 ± 0.03	0.96 ± 0.03	0.57 ± 0.10
R	0.99	0.99	0.99	0.94
b [Mm^{-1}]	0.42 ± 0.79	-0.95 ± 0.53	0.99 ± 0.51	1.06 ± 0.38
450 nm				
m	1.02 ± 0.02	1.00 ± 0.16	0.89 ± 0.11	0.21 ± 0.14
R	0.99	0.95	0.97	0.58
b [Mm^{-1}]	-1.85 ± 0.78	-0.82 ± 6.04	4.58 ± 4.88	3.43 ± 0.91

For 630 nm wavelength results, high Pearson coefficients (R>0.96) with negligible offsets (b<1 Mm^{-1}) and slopes ranging from 0.90 to 1.05 demonstrate good agreement (i.e., closure) for scattering and extinction coefficient measurements. Especially for MB and SOOT, the TAP measurements tend to overshoot the Differential method value by 20-40 %, whereas for BC the difference is only 10%. The reason could be that soot is a fractal agglomerate and in-situ methods as well as filter-based methods give different results as a function of the primary particle size (Sorensen et al., 2010) as well as of the previous mentioned filter-based artifacts, including changes of the slope at higher σ_{ap} (TAP) values. We measured values for BC ranging from 14 to 400 Mm^{-1} for $\sigma_{ep,630nm}$, 1 to 322 Mm^{-1} for $\sigma_{ap,630nm}$, and 12 to 174 Mm^{-1} for $\sigma_{sp,630nm}$. For SOOT, we measured values ranging from 12 to 158 Mm^{-1} for $\sigma_{ep,630nm}$, 1 to 322 Mm^{-1} for $\sigma_{ap,630nm,}$ and 5 to 80 Mm^{-1} for $\sigma_{sp,630nm}$.

For 450 nm wavelength results, similar slopes, Pearson R, and y-offset values are reported. Linear regression slopes for SOOT decrease at the lower wavelength to a value of 0.77 for light scattering and 0.7 for light absorption. This decrease may well be an effect of the primary particles size of agglomeration, since those relationships change with the wavelength. For MB, the light absorption measurements using the DM method shows the highest difference compared to the TAP measurement with a regression slope of 0.21 ± 0.14. The reasons could include different absorption behaviour (i.e., filter-based artifacts) for filter-based method relative to in-situ measurements [103]. Unfortunately, no clear understanding of the MB particle shape, phase, or uniformity could be made during this study.

Intensive Parameters of Aerosol Mixtures

Single scattering Albedo (SSA)

The Single Scattering Albedo (SSA), an important climate parameter, is investigated here as a relative measurement using a number of different methods of derivation to determine if closure between the different methods can be achieved.

The SSA for different combinations of instruments are derived using EQ 31 with the instruments used denoted in parentheses in Equations EQ 37 - EQ 40.

$$SSA(NEPH, TAP) = \frac{\sigma_{sp}(\mathrm{NEPH})}{\sigma_{ap}(\mathrm{TAP}) + \sigma_{sp}(\mathrm{NEPH})} \quad \text{EQ 37}$$

$$SSA(CAPS, TAP) = \frac{\sigma_{ep}(\mathrm{CAPS}) - \sigma_{ap}(\mathrm{TAP})}{\sigma_{ep}(\mathrm{CAPS})} \quad \text{EQ 38}$$

$$SSA(CAPS, CAPS) = \frac{\sigma_{sp}(\mathrm{CAPS})}{\sigma_{ep}(\mathrm{CAPS})} \quad \text{EQ 39}$$

$$SSA(NEPH, CAPS) = \frac{\sigma_{sp}(\mathrm{NEPH})}{\sigma_{ep}(\mathrm{CAPS})} \quad \text{EQ 40}$$

We have chosen to use the SSA(NEPH, CAPS) derived SSA values as a reference for these studies, as this method allows us to test the CAPS measured SSA with an independent, established method [63]. However, a strong argument could be made that the CAPS PM_{SSA} Monitor derived SSA values should be the true reference here, as the CAPS-derived SSA values were obtained by simultaneously measuring the scattering and extinction of same aerosol sample within a single instrument.

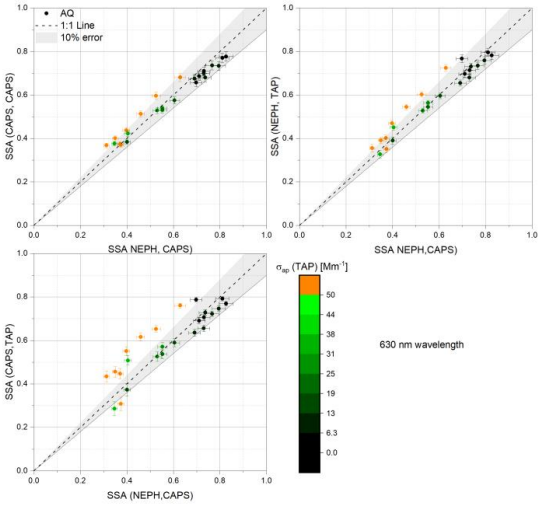

Figure 30. Scatter plots of derived SSA values from various combinations of measurements at 630 nm wavelength obtained for AQ/AS mixtures (y-axis) versus SSA(NEPH, CAPS) as the reference on the x-axis. The colour code indicates σ_{ap}(TAP) values shown in Mm^{-1}.

Figure 30 shows the SSA values obtained by the three combinations of measurements at 630 nm wavelength. The correlations show reasonable results relative to a ±10% error band, with the best correlation obtained for the SSA(CAPS, CAPS) versus SSA(NEPH, CAPS) measurements. In general, the higher the SSA values, the lower the measured absorption coefficients, σ_{ap}, reflecting that there are just fewer particles of Aquadag in the external aerosol mixture. The exception to this trend and the points exhibiting the greatest number of outliers (>10% from 1:1 line) are the points with high absorption coefficients (>50 Mm^{-1}). The largest outliers are observed in the instrument combinations that include the TAP and may be due to a nonlinear response in the TAP under high aerosol loadings.

Similar to the previous section, we calculated the ensemble instrument-to-instrument measurement ratio averages, using the SSA(NEPH, CAPS) values for reference, as another way of examining the correlations. The SSA values for all absorbing aerosol types (externally mixed with AS) are summarized in Table 11. The largest variance deviation is visible with combustion soot for TAP related data. The deviations of the reported mean from 1 are less than the relative uncertainties which range around 0.09.

Table 11. Ensemble instrument-to-instrument measurement ratio averages and standard deviations for different instrument combinations used to derive SSA values at 630 nm wavelength using $SSA(NEPH, CAPS)$ as reference.

Instrument combinations used for SSA calculations	BC	AQ	SOOT	MB
SSA (CAPS, CAPS) $/\, SSA(NEPH, CAPS)$	1.00 ± 0.08	1.01 ± 0.07	1.07 ± 0.07	1.00 ± 0.04
$SSA(NEPH, TAP)$ $/\, SSA(NEPH, CAPS)$	0.96 ± 0.08	1.02 ± 0.08	1.04 ± 0.29	1.00 ± 0.03
$SSA(CAPS, TAP)$ $/\, SSA(NEPH, CAPS)$	0.98 ± 0.16	1.05 ± 0.16	1.07 ± 0.51	1.00 ± 0.03

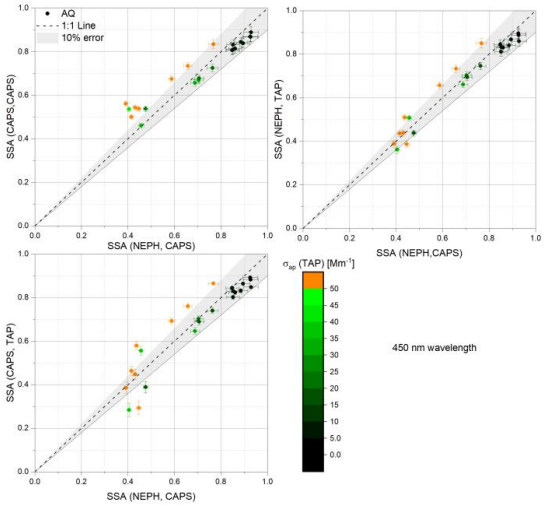

Figure 31. Scatter plots of Differential Method derived SSA values for different instrument combinations at 450 nm wavelength using AQ/AS mixtures versus SSA(NEPH, CAPS). The colour code indicates σ_{ap}(TAP) values shown in Mm^{-1}.

Figure 30 shows the SSA values obtained by the three combinations of measurements at 450 nm wavelength for all AQ/AS external mixtures. Observed patterns are comparable to the 630 nm wavelength results in Figure 30. For absorption coefficients up to 50 Mm^{-1}, all methods agree within 10%. Above 50 Mm^{-1}, the largest outliers are again observed in the instrument combinations that include the TAP instrument.

Table 12. Ensemble instrument-to-instrument measurement ratio averages and standard deviations for different instrument combinations used to derive SSA values at 450 nm wavelength using $SSA(NEPH, CAPS)$ as reference.

Instrument combination used for SSA calculation	BC	AQ	SOOT	MB
SSA (CAPS, CAPS) / $SSA(NEPH, CAPS)$	1.17 ± 0.21	1.04 ± 0.13	1.11 ± 0.13	0.98 ± 0.02
SSA (NEPH, TAP) / $SSA(NEPH, CAPS)$	1.07 ± 0.08	1.02 ± 0.08	0.96 ± 0.19	1.04 ± 0.13
SSA (CAPS, TAP) / $SSA(NEPH, CAPS)$	1.11 ± 0.13	1.03 ± 0.14	0.64 ± 0.38	1.05 ± 0.14

Table 12 summarizes the 450 nm wavelength ensemble instrument-to-instrument measurement ratio averages, using the SSA(NEPH, CAPS) values for reference. The pattern that fractal aerosol optical properties appear to differ most from the reference values as the wavelength decreases is visible here, too. The fresh combustion soot aerosol shows the largest deviation from 1 (0.64 ± 0.38) for SSA (CAPS, TAP) measurements. But, overall, all the instrument-to-instrument ratios are unity within the observed variances.

Ångström Exponents

Ångström exponents are calculated from extensive parameters measured at different wavelengths. Even a small error in the extensive parameter measurements can result in a significant uncertainty in the derived Ångström exponents, considering error propagation. Some of the optical instruments used in the current study are operated at slightly different wavelengths, such that the derived Ångström exponents exhibit slight biases due to these wavelength difference; these biases are small relative to the observed variances and are thus assumed negligible.

The following equations, based on EQ 32, are used to derive the Ångström exponents for extinction, scattering, and absorption using different instrument combinations with their specific wavelengths indicated:

$$x\mathrm{AE}(\mathrm{Instrument1, Instrument\ 2}) = -\frac{\log\left(\frac{\sigma_{xp\lambda1}(\mathrm{Instrument1,Instrument\ 2})}{\sigma_{xp\lambda2}(\mathrm{Instrument1,Instrument\ 2})}\right)}{\log(\lambda1/\lambda2)} \quad \text{EQ 41}$$

$$\mathrm{EAE(CAPS)} = -\frac{\log\left(\frac{\sigma_{ep\lambda1}(\mathrm{CAPS})}{\sigma_{ep\lambda2}(\mathrm{CAPS})}\right)}{\log(450/630)} \quad \text{EQ 42a}$$

$$\mathrm{EAE(NEPH, TAP)} = -\frac{\log\left(\frac{\sigma_{ep\lambda1}(\sigma_{ap}(\mathrm{TAP})+\sigma_{sp}(\mathrm{NEPH}))}{\sigma_{ep\lambda2}(\sigma_{ap}(\mathrm{TAP})+\sigma_{sp}(\mathrm{NEPH}))}\right)}{\log(450/630)} \quad \text{EQ 43b}$$

$$\mathrm{SAE(NEPH)} = -\frac{\log\left(\frac{\sigma_{sp\lambda1}(\mathrm{NEPH})}{\sigma_{sp\lambda2}(\mathrm{NEPH})}\right)}{\log(450/700)} \quad \text{EQ 44c}$$

$$\mathrm{SAE(CAPS, TAP)} = -\frac{\log\left(\frac{\sigma_{sp\lambda1}(\sigma_{ep}(\mathrm{CAPS})-\sigma_{ap}(\mathrm{TAP}))}{\sigma_{sp\lambda2}(\sigma_{ep}(\mathrm{CAPS})-\sigma_{ap}(\mathrm{TAP}))}\right)}{\log(450/630)} \quad \text{EQ 45d}$$

$$\mathrm{AAE(TAP)} = -\frac{\log\left(\frac{\sigma_{ap\lambda1}(\mathrm{TAP})}{\sigma_{ap\lambda2}(\mathrm{TAP})}\right)}{\log(467/652)} \quad \text{EQ 46e}$$

$$\mathrm{AAE(CAPS, NEPH)} = -\frac{\log\left(\frac{\sigma_{ap\lambda1}(\sigma_{ep}(\mathrm{CAPS})-\sigma_{sp}(\mathrm{NEPH}))}{\sigma_{ap\lambda2}(\sigma_{ep}(\mathrm{CAPS})-\sigma_{sp}(\mathrm{NEPH}))}\right)}{\log(450/630)} \quad \text{EQ 47f}$$

Extinction Ångström Exponents (EAE)

The derived EAE(NEPH, TAP) and EAE(CAPS) values are shown in Figure 32 as a scatter plot and in Figure 33 as a ratio versus the 630 nm wavelength SSA(NEPH, CAPS) values. The EAE(CAPS) values were used as the reference measurement. When directly comparing EAE(NEPH, TAP) to EAE(CAPS), the EAE values agree within 10% variance. The highest measured EAE values for the AQ and AS mixtures, around 3, were close to the EAE values measured for the pure AS particles distributions with CMD of 40 nm. The measured EAE(NEPH, TAP) / EAE(CAPS) ratios exhibited no systematic dependence on the σ_{ap}(TAP), or SSA(NEPH, CAPS) values. Measured EAE(NEPH, TAP) / EAE(CAPS) ratios for all absorbing aerosol types (externally mixed with AS) are listed in Table 13.

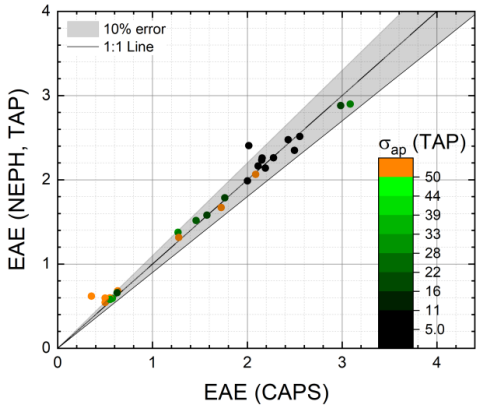

Figure 32. Scatter plot of EAE(NEPH, TAP) measurements compared to EAE(CAPS) measurements for AQ/AS mixtures. An error band of 10% is shown.

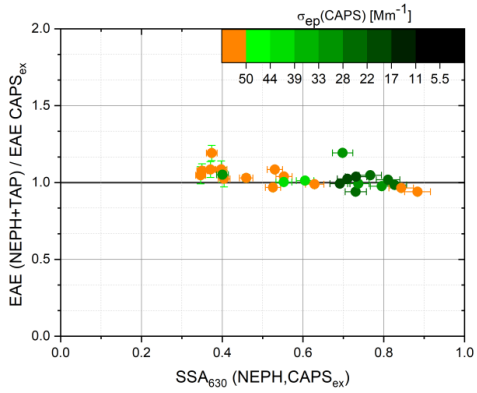

Figure 33. The extinction Ångström exponent EAE(NEPH, TAP) / EAE(CAPS) ratios as a function of 630nm wavelength SSA(NEPH, CAPS) values for AQ/AS mixtures. The 630 nm wavelength light absorption coefficient, σ_{ep}(CAPS), is used as the colour code.

Scattering Ångström exponent (SAE)

The derived SAE(CAPS, TAP) and SAE(NEPH) values are shown in Figure 34 as a scatter plot and in Figure 35 as a ratio versus the 630 nm wavelength SSA(NEPH, CAPS) values. The SAE(NEPH) values were used as the reference measurement. All SAE(CAPS, TAP) and SAE(NEPH) values agree within 10% variance and the measured SAE(CAPS, TAP) / SAE(NEPH) ratios exhibited no systematic dependence on the σ_{sp}(CAPS) for 630 nm wavelength, Figure 34, or SSA(NEPH, CAPS), Figure 35, values. The measured SAE(CAPS, TAP) / SAE(NEPH) ratios for all absorbing aerosol types (externally mixed with AS) are listed in Table 13.

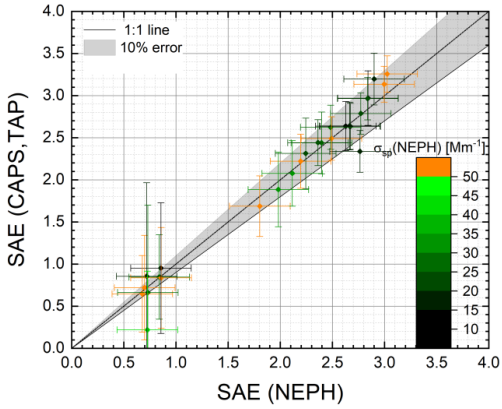

Figure 34. Scatter plot of SAE (CAPS, TAP) measurements compared to SAE(NEPH) measurements for AQ/AS mixtures. An error band of 10% is shown.

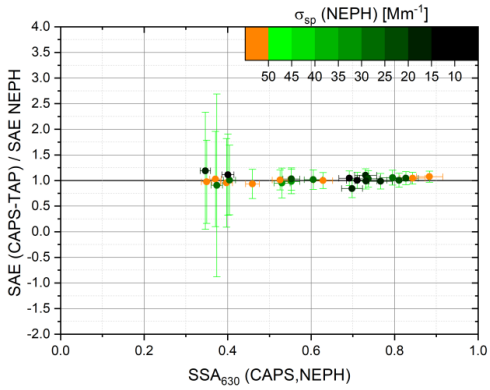

Figure 35. The scattering Ångström exponent ratio, SAE(CAPS, TAP) / SAE(NEPH), as a function of 630nm wavelength SSA(NEPH, CAPS) values for AQ/AS mixtures. The 630 nm wavelength light absorption coefficient, σ_{ap}(TAP), is used as the colour code.

Absorbing Ångström exponent (AAE)

The absorption Ångström exponent (AAE) depends entirely on the absorbing particle type and coatings and should not differ when the light absorbing particles are externally mixed with non-light absorbing particles. Thus, scatter plots of AAE values should exhibit a single point. Figure 36 shows the derived AAE(CAPS, NEPH) values relative to the derived AAE(TAP) values for pure AQ and for AQ/AS external mixtures. The AAE(TAP) values were chosen as the reference measurements here, despite the potential for known filter-based artifacts. The pure AQ measurements in Figure 36 exhibit a compact cluster around AAE of 0.4, indicating a well-defined (i.e., small variance) set of AAE measurements were obtained for both AAE measurements. The measured AAE for pure AQ particles of 0.4 is consistent with the "close to zero" results reported by Wang [104].

The externally mixed AQ/AS results show a significantly different result. For the AQ/AS mixtures, the AAE(TAP) exhibited a similar variance as for the pure AQ aerosols, while the AAE(CAPS, NEPH) values exhibited a much larger variance, including unphysical negative values. One reason for the larger AAE(CAPS, NEPH) variances observed for the externally AQ/AS mixtures relative to the pure AQ is that the mixed AQ/AQ samples were conducted at significantly lower AQ loadings (i.e., lower σ_{ap} values). Another reason is that the pure AQ aerosols exhibited the lowest SSA values (of 0.37 from Table 4) relative to the AQ/AS external mixtures.

Figure 36 shows the ratio AAE(CAPS, NEPH) / AAE(TAP) versus the 630 nm wavelength SSA(NEPH, CAPS) values. As predicted in the propagated error analysis shown in Figure 29, higher SSA values cause higher uncertainties in Differential Method calculated light absorption coefficients, σ_{ap}(DM), and, therefore, the derived AAE(CAPS, NEPH) values. In fact, since the derived AAE(CAPS, NEPH) values depend upon σ_{ap}(DM) measurements at two different wavelengths, the AAE uncertainties will be significantly higher than the corresponding σ_{ap}(DM) uncertainties, especially at high SSA values. Figure 37 indicates that lowering the absorption coefficients below 50 Mm^{-1} or increasing the SSA above 0.5, the derived AAE(CAPS, NEPH) values begin to vary strongly relative to the AAE(TAP) values. For laboratory studies, aerosols with similar low SSA values and high absorbing particle concentrations can be readily achieved, but are rarely present in the ambient atmosphere. Therefore, extreme caution is justified when attempting to derive AAE(CAPS, NEPH) values for atmospheric measurements.

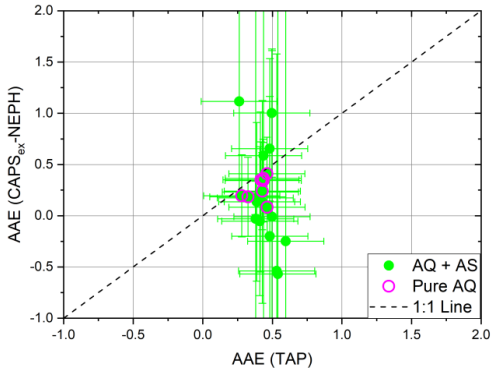

Figure 36. Scatter plot of AAE(CAPS, NEPH) measurements compared to AAE(TAP) measurements for pure AQ and AQ/AS external mixtures. Measured precision error bars are shown for individual AQ/AS externally mixed measurements.

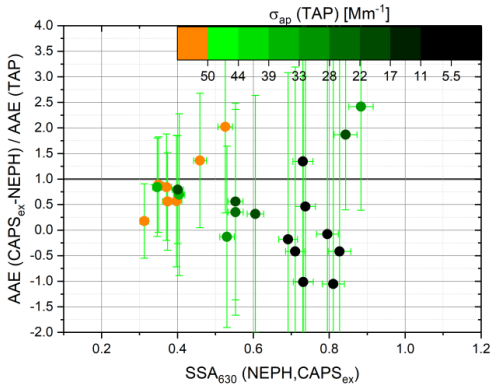

Figure 37. The absorbing Ångström exponent ratio, AAE(CAPS, NEPH) / AAE(TAP), as a function of 630 nm wavelength SSA(NEPH, CAPS) values for AQ/AS mixtures. The 630 nm wavelength light absorption coefficient, σ_{ap}(TAP), is used as the colour code. Measured precision error bars are shown for individual measurements.

Table 13 summarizes the averages and standard deviations of the measured Ångström exponent ratios, EAE(NEPH, TAP) / EAE(CAPS), SAE(CAPS, TAP) / SAE(NEPH), and AAE(CAPS, NEPH) / AAE(TAP). The average Ångström exponent ratios for light extinction (EAE) and scattering (SAE) fall within 10% of unity, with SOOT exhibiting the large variances. The average Ångström exponent ratios for light absorption (AAE) exhibit large deviations from unity with even larger variances. A large deviation for the AAE ratios value is associated with weak absorption coefficients of the aerosol mixtures used. Therefore, the AAE values show the biggest differences within the instrument-to-instrument ratio analysis.

Table 13. Ensemble averages and standard deviations for the instrument-to-instrument ratios of the Ångström exponents (EAE, SAE, AAE) derived from multiple instruments relative to those derived from single instruments as reference.

Ångström ratio	coefficient	BC	AQ	SOOT	MB
EAE(NEPH, EAE(CAPS)	TAP) /	0.92 ± 0.07	1.05 ± 0.15	0.99 ± 0.56	0.97 ± 0.15
SAE(CAPS, SAE(NEPH)	TAP) /	1.13 ± 0.10	0.99 ± 0.15	1.43 ± 0.61	1.09 ± 0.15
AAE(CAPS, AAE(TAP)	NEPH) /	1.72 ± 0.85	0.39 ± 1.70	1.19 ± 0.93	0.91 ± 2.32

7.1.7 Summary on uncertainty measurements for aerosol optical properties

A major goal of this study was to determine if the intensive optical aerosol parameters, single scattering albedo and Ångström exponents, for externally mixed absorbing and non-absorbing aerosols could be measured within reported optical instrument extensive measurement uncertainties (i.e., optical closure). Closure within reported instrument uncertainties was achieved for all measured extensive optical properties (i.e., extinction, scattering, and absorption) and most intensive optical properties (i.e., single scattering albedo, extinction Ångström exponent and scattering Ångström exponent). Unsurprisingly, the measurements with the largest variances were the absorption coefficient measurements derived from the Differential Method (i.e., absorption = extinction minus scattering) and the related absorbing Ångström exponent (AAE). While the absorption coefficient measurements were within reported uncertainties, the derived AAE values exhibited average values and standard deviations far greater than the other Ångström exponent but are within the expected range.

We conducted an instrument intercomparison laboratory study employing several widely used measurement techniques suitable for long-term ambient observations. The optical instrument suite included two CAPS PM_{SSA} monitors measuring extinction and scattering at 450 and 630nm, a TSI integrating Nephelometer (NEPH) measuring scattering at 450, 550, and 700 nm, and a Brechtel Tricolor Absorption Photometer (TAP) measuring absorption at 467, 528, and 652 nm. External mixtures of absorbing (Aquadag, combustion soot from a laboratory flame generator, Cabot carbon black, and acrylic Magic Black paint) particles and non-absorbing ammonium sulphate particles were generated with single scattering albedo (SSA) values between 0.2 and 1.0 and extinction values between 15 – 150 Mm^{-1}, representative of atmospheric aerosols. However, our study does not explicitly address real-world ambient aerosols that can be internally or

externally mixed or both, contain particles with liquid, solid, and/or semi-solid phases, and may contain multiple sources of absorbing material.

Overall, we were able to show that measured extensive optical parameters agree within the limits of uncertainty for the individual or combined instruments. In particular, we report that the scattering coefficient measurement by the CAPS PM_{SSA} agrees with the TSI integrating Nephelometer within 10% relative error (i.e., optical closure). Therefore, The CAPS PM_{SSA} monitor could be considered as a replacement for the TSI Nephelometer, as the NEPH is no longer produced. Trade-offs in the CAPS PM_{SSA} versus NEPH comparison include the three wavelengths and backscatter measurements of the NEPH versus the single wavelength of the CAPS PM_{SSA}, countered by the additional extinction measurement of the CAPS PM_{SSA} allowing for absorption and SSA values to be simultaneously measured.

Measurement differences were observed as a function of absorbing particle type. For light absorbing compact aggregates, we achieved the highest correlations for light extinction, scattering, and absorption coefficients. For fractal-like absorbing combustion soot particles, the correlation for light absorption between the in-situ and filter methods weakened but stayed within instrument uncertainty ranges. These observed differences might be due to the combined effects of small flickers from the inverted flame generator during the experiment, the overall filter correction schemes, and/or the physical behaviour of agglomerates. For more compact particles, the scattering is stronger [105]. For the TAP filtered-based method, changes in the backscattering of light is not considered in the correction schemes, which might be responsible for the disagreement.

Uncertainties increased for intensive optical parameters, especially for the absorption Ångström exponent (AAE) parameter that relied on the differential method to calculate light absorption as the difference between light extinction and light scattering. The intensive parameters for the scattering and extinction Ångström exponent were within 10% relative error (i.e., optical closure), regardless of which instrument combination was used for parameter derivation. In contrast, absorption Ångström exponent (AAE) values required low SSA values (<0.5) and high particulate absorption values (>50 Mm^{-1}) were necessary to reach satisfactory levels of measurement uncertainty. Similar AAE results were recently reported for rural background sampling[106]

Finally, a global analysis study for climate relevant aerosol properties [102] recently stated measurement requirements for GCOS (Global Climate Observing System) applications for attributing and detecting changes to climate feedback. The reported requirements for the climate-critical intensive optical properties, specifically the single scattering albedo (SSA), are measurement techniques with relative measurement uncertainties less than 20%. In our study, SSA values were measured for all instrument combinations of CAPS, TAP, and NEPH within 10% relative error at 630 nm wavelength and within 15% at 450 nm wavelength. Therefore, the measured SSA averages and variances using our optical instrument suite for externally mixed laboratory particles indicates that these instruments meet these proposed requirements.

7.2 CAPS characteristics and LOD estimation

To estimate the lower detection limit of the CAPS-System, an Allan deviation approach was done by using measurement data of an aerosol free air flow [57].

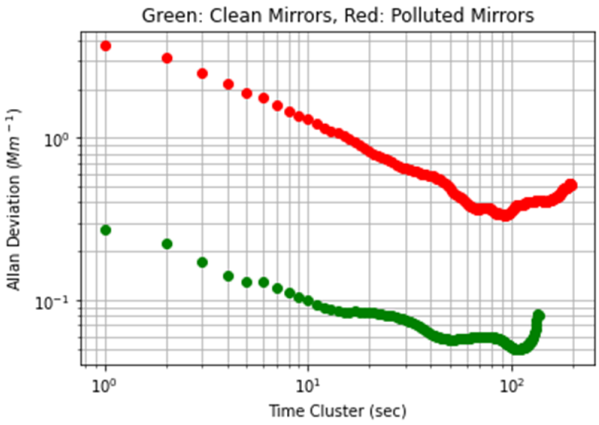

Figure 38. Allan Deviation calculations for fresh cleaned mirrors (LOSS=500, green makers) and dusted mirrors (LOSS=1600, red markers) for the CAPS instrument.

In a self-written Python code using the Jypter Notebook and several libraries like pandas, matlabplotlib and allantools, the Allan Deviation was calculated to estimate the lower detection limit of the instrument response. As an indicator for the "dirtiness" of the mirrors, the instruments deliver the LOSS value. At a value of 500 or below the mirrors are clean and can deliver a lower detection limit of down to 0.05 Mm^{-1}. As soon as a LOSS of over 1600 is reached for clean air, the mirrors are highly dusted, but can still deliver a lower detection limit down to 0.25 Mm^{-1} for 100 s integration time. This is in accordance with previous values visible in Figure 39.

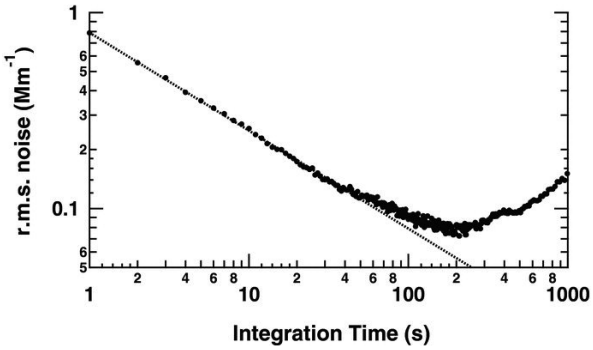

Figure 39. Allan Variance for CAPS measurements obtained by Massoli [57].

As a next step, ammonium sulphate was nebulised and sorted in different electrostatic mobility sizes. The measured number concentrations with their particle sizes were used for Mie calculation to compare those with the light extinction coefficient of the CAPS PM_{SSA}.

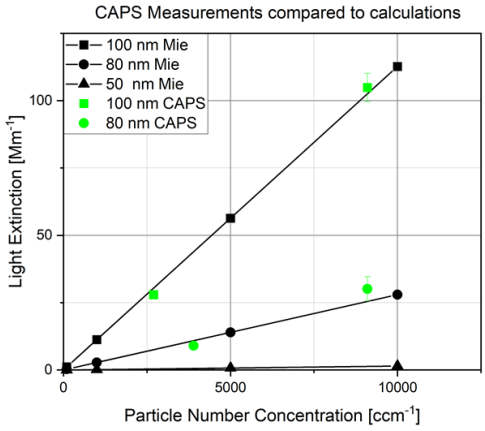

Figure 40. CAPS light extinction measurement compared with Mie Theory as a function of the particle number concentrations separated for 50, 80, 100 nm particles selected by the DMA.

Those ammonium sulphate particles have a refractive index of 1.53 and the extinction coefficient was calculated using Mie theory for different particle sizes, as well as for a range of particle concentrations. The aerosol light extinction is linear towards the particle concentrations, as long as the size distribution is fixed. To show the size dependency, the calculations were done for 450 nm wavelengths CAPS PMex and compared with the instrument response for particle diameters smaller than 100 nm. As it is shown in Figure 40, the aerosol light extinction signal shrinks drastically, at particle diameters lower than half of its wavelength even for large aerosol number concentrations. Even at very polluted conditions, shown here with particle number concentrations of over 10000 1/ml, the aerosol light extinction is close to zero for 50 nm particles. The size dependency for aerosol extinction is strong.

Qualification of the CAPS

The CAPS-module includes one cavity for nitrogen dioxide, two aerosol light extinction tubes for 450 nm wavelength and the last for 630 nm wavelength. The most important ones will be mentioned here, even though the entire set-up was manufactured in the in our workshop. A Light emitting diode provides a square wave modulated radiation at a controlled frequency. The cavity consisting of a 27cm tube and two high reflective spherical mirrors. The cavity is loaded with light as long as the LED is switched on. The cavity is discharged as long as the LED is switched off. On the other side a photodiode measures the amount of light that passes through the high reflective mirrors. Between those parts are multiple apertures and an Pérot-Fabry-Interferometer (etalon). Only radiation of a distinct frequency in resonance to the etalon is transmitted. A detailed setup instruction guide with a stepwise approach has been written for future builds but is not discussed here. The phototube must detect small changes in the light and is therefore provided with an inverter operational amplifier. This device boosts the signal significantly since the negative feedback resistor Rf is a 100 G Ohm component. For the non-inverting amplifier, the amplified Voltage V_{out} reads: $V_{out} = V_{in}\left(1 + \frac{R_f}{R_g}\right)$

7.2.1 Intercomparison Campaign for CAPS NO2

The CAPS NO_2 System was tested during an intercomparison campaign at Forschungszentrum Jülich in 2019. The CAPS directly measures the NO_2 absorption in the electromagnetic spectrum at 450 nm (blue region). In contrast to CLD, there is no chemical conversion in CAPS systems and thus they are free of interference from other nitrogen-containing species such as PAN, nitrate, or HNO3. The CAPS System is compared with two chemiluminescence detectors (CLD). The Eco Physics AG (CLD TR 780, Duernten, Switzerland) was operated by Franz Rohrer, Benjamin Winter and Robert Wegener. Another CLD monitor (Teledyne API T200, San Diego, USA) fitted with a molybdenum converter to convert NO2 to NO was operated by Claus Nordstroem, Jesper Nygaard and Tom Jensen from Aarhus University. In Figure 41 a set of measurement data from November 2019 is plotted. The slope between the Teledyne API T200 and CAPS is 0.99 with a high correlation of $r^2 = 0.99$.

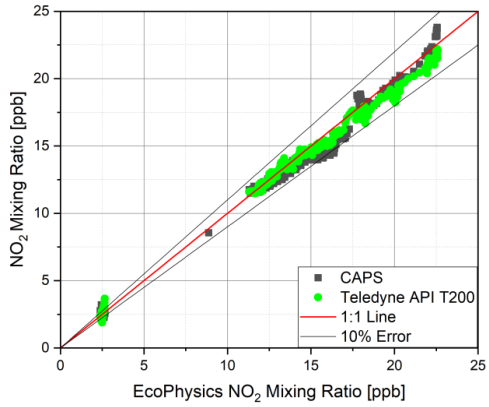

Figure 41. Intercomparison of between two CLD instruments and the CAPS.

In Figure 42 the time series during that day is shown. Prior to the measurements, 14 ppb NO was flushed into the ring line. At minute 90, 14 ppb NO_2 was added as well as 15 ppb Ozone. After that the NO_2 decreased as the time went by. During the intercomparison all instruments were subject to from periodically occurring concentration variations, since all instruments were connected to one ring line and the pressure changed due closing valves of self-calibrating instruments.

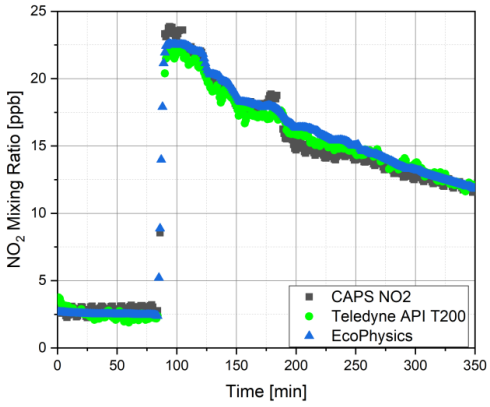

Figure 42. Time Series of the NO_2 intercomparison starting at 10am from the 16th of October 2019.

8 Flight Simulation Test Stand

A schematic diagram of the experimental set-up of the Flight Simulation Test Stand is shown in Figure 43. In order to provide a steady and constant particle production in size distribution and number concentration, a constant output atomizer (Model 3076, TSI Inc.) was used, which nebulizes a constant stream of a salt solution [94]; (TSI Inc. Model 3076 Manual). After the aerosol flow passes through a diffusion dried tube, the relative humidity reaches levels of below 5%. It follows a charging process by passing through a radioactive AM-241 neutralizer and the classification in a monodisperse aerosol takes place by a Vienna-type Differential Mobility Analyzer (DMA, Model M-DMA 55-U, Grimm). This aerosol enters the low-pressure zone by passing through a critical orifice. The aerosol is diluted within the mixing chamber. The pressure is controlled there as well by a LabVIEW program by means of multiple mass flow controller with an PID approach. Furthermore, the relative humidity is actively controlled by mixing a stable humidified saturated air flow into the system through the mixing chamber. The provided aerosol sample flow relative humidity is limited to approximately 30%. After passing the mixing chamber, the aerosol flow is provided to the measuring instruments using individual isokinetic, iso-axial samplers located in the centre of the sample line. Here, a Sky-CPC 5.411 (Grimm) was used as a well characterized butanol condensation particle counter (Bundke et al. 2015). An aerosol electrometer was used as a traceable reference instrument for particle counting measurements (FCE, Model 5.705, Grimm). For fresh flame soot measurements, the nebulizer as well as the dehydration tube were replaced by a Miniature Inverted Flame Soot Generator (Argonaut Scientific Corp., Edmonton, AB, Canada).

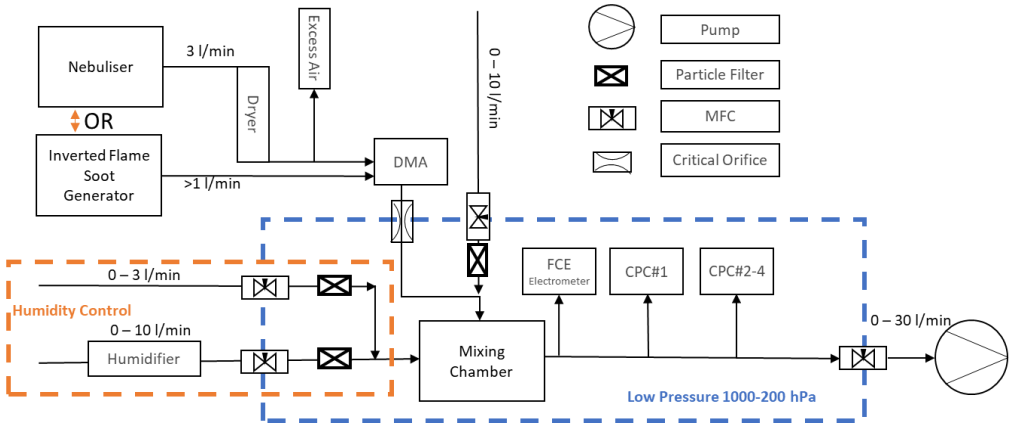

Figure 43. Flight Simulation Test Stand: Flow schematic of the laboratory set-up for the low-pressure characterisation with two aerosol sources. The inline pressure is PID controlled balancing the volumetric in- and out flow via mass flow controllers (MFC) as control elements; the aerosol size classification is ensured with a differential mobility analyser (DMA) and the faraday cup electrometer (FCE) functions as a reference instrument for particle counting).

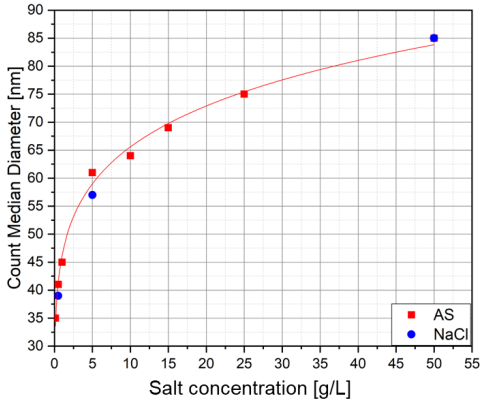

Figure 44. The CMD with the relationship of the concentration of the nebulised salt solution.

The nebuliser generates salt particles in correlation to the salt concentration in solution of the supply bottle as visible in Figure 44.

8.1 FCE Data treatment

A significant issue for the measurement of nanometre-sized particles using a DMA is the presence of multiple charged particles. These have the identical electrical mobility as singly charged particles but are larger in size. This effect leads to a notable difference in the counting rate between a condensation particle counter and an aerosol electrometer as described below. To address this artefact, the correction scheme and routine was used, which was introduced by Bundke [55, 107].

From Bundke et al. (2015) [50]: "Using a diffusion charger in combination with a DMA and using FCE as reference instrument it must be considered that particles passing the DMA may carry multiple charges. If a particle exiting the DMA carries *n* charges the FCE will count these particle *n* times whereas a CPC will register just one particle. Thus, a multi-charge correction must be applied to the FCE data:

$$N_{FEC}(D_{p)} = \sum_{n=0}^{\infty} nN^*(D_p(U,n))\eta(n, D_p(U,n)) \quad \text{EQ 48}$$

For technical reasons – only charged particles will pass the DMA – and as a good approximation we limit the sum to (1≤*n*≤2). Thus, only single and double charged particles are considered. Here, $N^*(D_p)$ denotes the 'true' particle number per time interval as a function of the electrostatic mobility particle diameter $D_p(U, n)$, *U* denotes the DMA voltage and $\eta(n, D_p)$ the normalised charge distribution of particles carrying *n* charges. For the latter, we use the approximation by Wiedensohler (1988) [108]:

$$\eta(n) = 10^{\sum_{i=0}^{5} a_i(n) \log\left(\frac{D_p}{nm}\right)} \quad \text{EQ 49}$$

The approximation coefficients a_i are defined by:

Table 14. Approximation coefficients [108].

	n				
a *i* (*n*)	**−2**	**−1**	**0**	**1**	**2**
a 0	−26.3328	−2.3197	−0.0003	−2.3484	−44.4756
a 1	35.9044	0.6175	−0.1014	−0.6044	79.3772
a 2	−21.4608	0.6201	0.3073	0.48	−62.8900
a 3	7.0867	−0.1105	−0.3372	0.0013	26.4492
a 4	−1.3088	−0.1260	0.1023	−0.1544	−5.7480
a 5	0.1051	0.0297	−0.0105	0.032	0.5059

Thus, $N_{FCE(Dp)}$ joins as:

$$N_{FCE}(D_p) = N \cdot \left(D_p(U, n=1)\right)\eta\left(n=1, D_p(U, n=1)\right) + 2N \cdot \left(D_p(U, n=1)\right)\eta\left(n=2, D_p(U, n=2)\right) \quad \text{EQ 50}$$

Equivalent the number concentration of N_{CPC} of the CPC is given by

$$N_{CPC}(D_p) = N \cdot \left(D_p(U, n=1)\right)\eta\left(n=1, D_p(U, n=1)\right) + N \cdot \left(D_p(U, n=1)\right)\eta\left(n=2, D_p(U, n=2)\right) \quad \text{EQ 51}$$

Using this equation, the ratio N_{CPC}/N_{FCE} gives the correction factor $\xi(D_p)$.

For Using

$$A = N^*\left(D_p(U,n=1)\right)\eta\left(n=1,D_p(U,n=1)\right) \quad \text{EQ 52}$$

And

$$B = N^*\left(D_p(U,n=2)\right)\eta\left(n=2,D_p(U,n=2)\right) \quad \text{EQ 53}$$

ξ can be expressed as

$$\xi = \frac{N_{CPC}}{N_{FCE}} = \frac{A+B}{A+2B} = \frac{1+\frac{A}{B}}{2+\frac{A}{B}} \quad \text{EQ 54}$$

Substituting the expressions of

$$\frac{A}{B} = \frac{N^*\left(D_p(U,n=1)\right)}{N^*\left(D_p(U,n=2)\right)}\frac{\eta\left(n=1,D_p(U,n=1)\right)}{\eta\left(n=2,D_p(U,n=2)\right)} = \mathfrak{C}\,\mathfrak{D}$$

using:

$$\mathfrak{C} = \frac{N^*\cdot\left(D_p(U,n=1)\right)}{N^*\cdot\left(D_p(U,n=2)\right)} \qquad \mathfrak{D} = \frac{\eta\left(n=1,D_p(U,n=1)\right)}{\eta\left(n=2,D_p(U,n=2)\right)}$$

Therefore, the factor $\mathfrak{C}$ is calculated by using the size distribution measurement. Here, the diameters $D_p(U,n=1)$, $D_p(U,n=2)$, are associated with the different DMA voltages U. They are calculated by solving the implicit equation:

$$D_p = \frac{neC(D_p)}{3\pi\mu}\cdot\frac{2\pi LU}{\ln\left(\frac{r_a}{r_i}\right)Q_{Sh}} \quad \text{EQ 55}$$

With n as the number of charges, e as elemental charge of $1.6022*10^{-19}$C, μ as the gas viscosity, L the DMA length, r_a the DMA outer radius, r_i the DMA inner radius and Q_{sh} as the sheath flow and C(Dp) denotes the Cunningham correction factor.

The factor $\mathfrak{D}$ is calculated using the equation EQ 49

Finally, the multiple charge correction can be expressed by

$N^*_{FEC} = \xi(D_p)N_{FCE}$

as N^*_{FEC} as the corrected electrometer number concentration and ξ as the calculated correction factor.

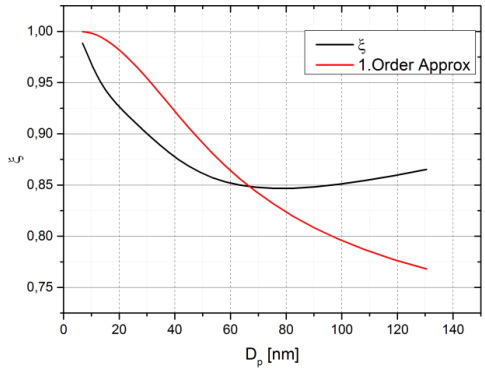

Figure 45. Multi charge correction function adapted from Bundke et al., (2015)[50].

Figure 45 shows the multi-charge correction factor ξ(Dp) as a function of the particle diameter. The red line shows the first order approximation ignoring the actual size distribution by setting $\mathfrak{C} = 1$. The first order approximation deviated significantly (up to 15%) from the ξ (D_p) curve. Thus, the actual size distribution measurement needs to be considered. “

8.2 Characterisation of the MAGIC CPC

This chapter is based on the manuscript: Weber, P., Bischof, O. F., Fischer, B., Berg, M., Hering, S., Spielman, S., Lewis, G., Petzold, A., and Bundke, U.: Characterisation of a self-sustained, water-based condensation particle counter for aircraft cruising pressure level operation, Atmos. Meas. Tech., 16, 3505–3514, https://doi.org/10.5194/amt-16-3505-2023, 2023.

This manuscript provides the characterisation of the Moderated Aerosol Growth with Internal water Cycling CPC (MAGIC, Aerosol Devices Inc., Fort Collins, CO, USA) at low-pressure conditions at cruising altitude as low as 150 hPa and describes the mechanism to improve the hardware control parameters for robust aircraft operations. In Figure 46 the main principle of this kind of CPC is shown. Water-based CPCs have an inverted temperature design. The cooling step is located prior of the warming stage regarding the air flow. The design of the MAGIC added another cooling step, to let water condense on the wick to recycle water.

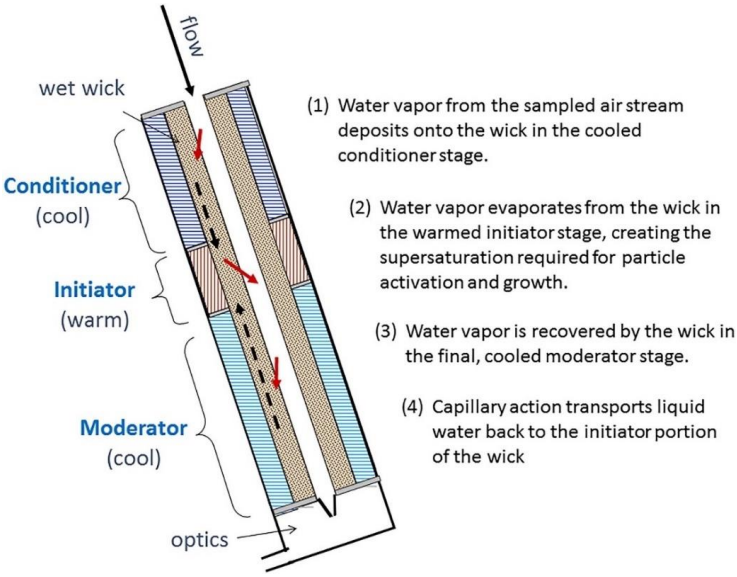

Figure 46. Principle of Operation of the MAGIC-CPC [109].

This study is part of the development of a new air quality instrument for IAGOS in response to flight safety aspects, which prohibits to bring flammable liquids onboard on passenger aircraft. The new water-based condensation particle counter (MAGIC 210-LP; Moderated Aerosol Growth with Internal water Cycling – Low Pressure) for low-pressure applications down to 300 hPa characterised in this study was recently introduced to the market by Aerosol Dynamics Inc. and is based on the standard MAGIC CPC, which contains a pre-humidifier, where the aerosol sampling flow is guided to a continuous wet wick with different temperature zones. The humidified sample flow starts with the cold conditioner region, followed by the warm initiator and a cold moderator zone before finally passing the optics head [109]. The MAGIC 210-LP CPC was subjected to counting efficiency experiments for a pressure range down to 200 hPa and different types of test aerosol particles representing salt particles and non-soluble particles. The conducted experiments were part of the qualification of the individual components of the new IAGOS air quality instrument.

8.2.1 Methods and Test-Set-up for CPC low Pressure Calibration

A schematic of the experimental set-up is shown in Figure 47. We used a nebuliser to atomise an ammonium sulphate (AS) solution to provide a steady and constant particle production in size distribution and number concentration (constant output atomizer, Model 3076, TSI Inc., Shoreview, MN, USA) [94]; (TSI Inc. Model 3076 Manual). After the aerosol flow passes through a diffusion dryer tube, the relative humidity reaches levels below 5%. The sample flow follows a charging process by passing through a radioactive Am-241 source and the classification in a monodisperse aerosol takes place by a Vienna-type Differential Mobility Analyzer (DMA, Model M-DMA 55-U, Grimm Aerosol Technik GmbH & Co. KG, Ainring, Germany). The aerosol enters the low-pressure zone by passing through a critical orifice. The aerosol is diluted in the mixing chamber with aerosol-filtered air. The pressure is controlled by a LabVIEW program through

multiple mass flow controllers with a PID (proportional-integral-derivative controller) approach. At 200 hPa, the measured standard deviation was less than 0.1 hPa with an integration time of 100 s. Furthermore, the relative humidity is actively controlled by adding a stable humidified air flow into the system through the mixing chamber, which is limited to approximately 30% relative humidity. Temperature, inline pressure, and relative humidity are measured in the mixing chamber. Water vapour can be added to test particle activation growth effects for different relative humidity levels. The volume of the mixing chamber is 500 ml with a flow rate of 10 l/min. This leads to a flushing time of roughly 3 sec and an e-folding time of 1.8 sec for 63%. After passing through the mixing chamber, the aerosol flow is guided to the measuring instruments using individual isokinetic, iso-axial samplers located in the centre of the sample line. The diffusion losses are similar for all instruments. The flexible conductive sampling tubing length from the line to the instruments is set to 25 cm for instruments sampling at a flow of 0.6 l/min and adjusted proportionally to instruments with a different sampling flow. A Sky-CPC 5.411 (Grimm) was used as a well-characterized butanol condensation particle counter (Bundke et al. 2015). An aerosol electrometer was used as a traceable reference instrument for particle counting measurements (FCE, Model 5.705, Grimm). The instrument of interest was the newly developed Moderated Aerosol Growth with Internal Water Cycling CPC (MAGIC 210-LP, Aerosol Dynamics Inc, Berkeley CA, USA). For the fresh flame soot measurements, the nebuliser and the dehydration tube were replaced by a Miniature Inverted Flame Soot Generator (Argonaut Scientific Corp., Edmonton, AB, Canada). Prior studies provide greater detail [55, 107].

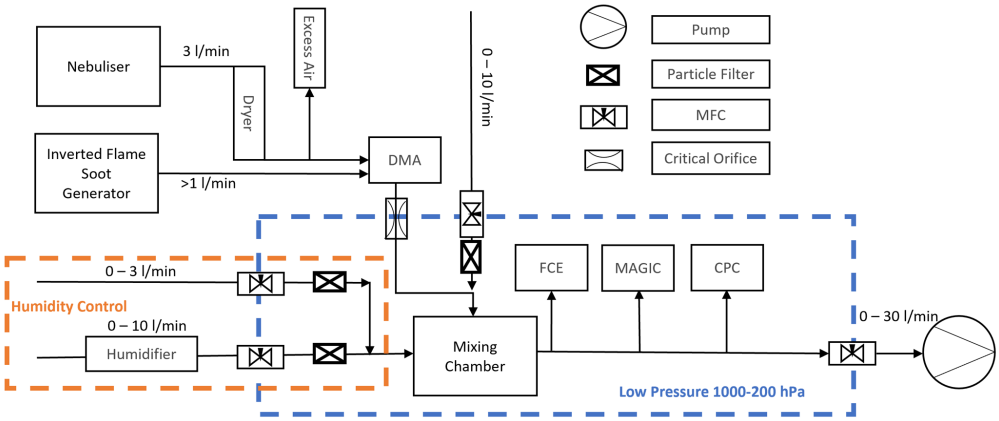

Figure 47. Flow schematic of the laboratory set-up for the low-pressure characterisation with two aerosol sources. The inline pressure is controlled via mass flow controllers (MFC); the aerosol size classification is ensured with a differential mobility analyser (DMA) and the faraday cup electrometer (FCE) functions as a reference instrument for particle counting). Adapted from Figure 43.

The DMA was operated stepwise for 30 seconds for each voltage level corresponding to different particle sizes starting at an upper limit of 140 nm and going down to 2.5 nm. This size limit is set by the fact that we used the 8.8 cm tube and a 6 l/min sheath flow for a high accuracy and low mobility size half-width. To avoid transition effects and to achieve an uniform aerosol inside all

measuring instruments, the first 15 seconds for each particle size setting of the DMA were excluded from the dataset. Earlier experiments have shown that this time is sufficient to flush the system.

The inverted flame soot generator was operated with an oxidation-air-to-propane ratio of 7.5 L/min air to 0.0625 L/min propane. This flow setting ensures stable low organic carbon soot production [95, 96].

An exponential function EQ 56 introduced by Wiedensohler et al. (1997) [110] is used to give quantitative information about the cut-off efficiencies. Here, the revised formulation by Banse [111] provides a more quantitative description of the particle counting efficiency curves compared to the electrometer.

$$\eta = A - B * (1 + \exp\ (\frac{(D_p - D_1)}{D_2}))^{-1} \quad \text{EQ 56}$$

where η is the counting efficiency, D_p is the particle size, and A, B, D_1, and D_2 are fitting parameters of this four-parameter exponential function. The fitting parameter A is the maximum of the function and gives the value of the plateau.

8.2.2 Optimisation of pressure dependent control variables for Laser Power and Detector

Two critical variables for low-pressure measurements automatically control the MAGIC 210-LP CPC counting efficiency. The first variable is the laser power which is adjusted to compensate for variations in droplet size as a function of the operating pressure. With decreasing pressure levels, droplet growth is affected, making the droplets smaller. The laser power automatically increases as the internal instrument pressure decreases to compensate for the smaller droplet size. The second variable is the detection threshold voltage which is adjusted to compensate for variations in background scattered light (i.e., measured light with zero particle counts) as the laser power varies, since the background light scattering on molecules increases with increasing laser power. In the experiments, the MAGIC 210-LP CPC was operated with the temperature settings recommended for low pressures by the manufacturer in the operational manual. During normal (ambient, 1000 hPa) operation, the conditioner is maintained at 18 K below and the initiator at 17 K above the heat sink temperature, typically a few degrees above ambient temperature. The moderator temperature is usually set as a function of input dew point to minimise water usage. The user has the option of changing this temperature or setting fixed temperatures. The manual for the MAGIC 210-LP states, that the conditioner temperature should be kept at 2°C and the moderator at 4°C for low-pressure operations. The initiator is fixed at 45°C to remain below the boiling point when operating at pressures as low as 150 hPa. However, these working points cannot be reached if the heatsink exceeds temperatures of 33°C. During measurement a heatwave occurred, and it became clear that the thermoelectrical devices had reached their limits. It was then observed, that in case the temperatures of the conditioner and the moderator are about 3 K above their recommended values, the counting efficiency decreases by about 20% from 100% to 80% overall counting efficiency at pressure levels 250 hPa and below. This limitation, however, is solvable by maintaining the ΔT between all temperature zones of the sections of the growth tube equally.

The manufacturer's settings were not optimised for operating pressure down to 200 hPa. For 250 hPa, we found, that the required laser power was increased so high by the firmware to compensate for the smaller droplet sizes, thus the electronics could not compensate the baseline voltage correctly. By adjusting the values for the laser power and detector threshold, we solved this issue. Therefore, the MAGIC LP-210 is now able to operate even below 250 hPa. The new settings are applicable for the complete pressure range without change.
Based on this study, Aerosol Dynamics Inc. has updated their low-pressure CPCs to operate down to 200 hPa.
Figure 48 shows an idealized signal from the optics electronics. The analogue signal is compared to the "detector threshold" (normally 250 mV) which produces a digital pulse that increments a counter in the microcontroller.
The "baseline voltage", i.e., the signal with no particles present, could be above or below 0 volts due to imperfection in the optics and electronics, as shown in Figure 49. There is always some stray light that reaches the photo detector, and all operational amplifiers have some non-zero offset. To compensate, a "detector offset" is added to the analogue signal to adjust the baseline voltage to zero.
Since the stray light reaching the photodetector is proportional to the laser power, the firmware automatically adjusts both the laser power and detector offset with pressure. The specific relationship between laser power and detector offset are set at the factory and vary from instrument to instrument.
To operate the MAGIC 210-LP at pressures lower than then it was designed for, voltage offset and detector thresholds had to be determined experimentally below 300 hPa. At 250 hPa, we found that the required laser power was so high that the electronics was incapable of zeroing out the baseline voltage. To compensate, the detector threshold was increased above the factory setting of 250mV (Figure 50).

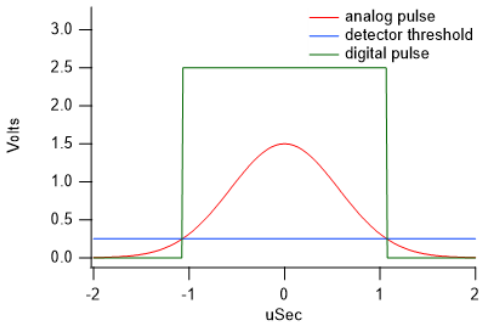

Figure 48. Ideal signal from one particle passing through the optics detector [112].

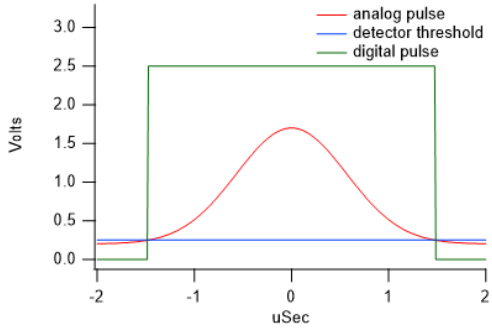

Figure 49. Effect of imperfections in optics and electronics on the baseline voltage.

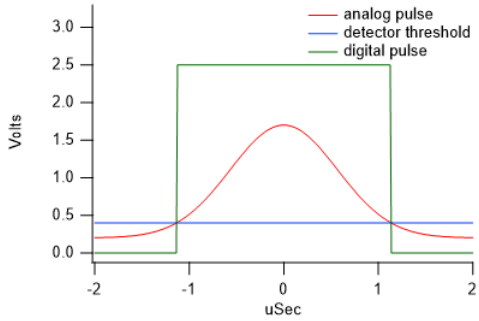

Figure 50. Detector threshold is increased to compensate for inability of the electronics to completely cancel out the baseline signal at lowest pressure.

As the absolute pressure during operation decreases, also the droplet growth is reduced resulting in smaller droplets, which need to be counted. This is compensated by adjusting the laser power and the detector threshold. The instrument firmware makes these adjustments automatically based on a lookup table, and the 1 Hz absolute pressure reading. Concentrations are reported with respect to laboratory conditions of 25°C and 1013 hPa.

The following optimisation step was applied. The MAGIC 210-LP was designed for operation at pressure levels as low as 300 hPa. We were able to extend the range of operation down to 200 hPa by the adjustment of the initial laser power to different pressure levels. In Figure 51 the counting efficiency is expressed as the number concentration measured by the MAGIC instrument divided by the number concentration measured by the G-CPC instrument and is shown at different pressure levels for 100 nm sized particles for a range of initial laser power settings. To compensate the effect that particles grow less efficiently at lower pressures the threshold and the laser power are controlled as a function of the internal measured pressure. Here the laser power is increased, and the offset is lowered with decreasing pressure values. At 250 hPa the adjusted detector threshold reaches 0 V and only the constant parameter of the detector threshold limits the counted signals. The detector offset adjusts for non-ideal electronics and optics so that the signal without any particles present is at zero volts. The detector threshold is the voltage level that is used to determine if a particle is in the laser beam. In Figure 51 each graph was obtained from measurements at a detector threshold setpoint of 250 mV. The only exception is the “250 hPa optimised”. To compensate for the increased stray

light, the detector threshold was increased from 250 mV towards 400 mV. This series of measurements was conducted with the increased 400 mV detector threshold. This method of adjusting the initial laser power setting increased the secure bandwidth of laser power that could be applied, without false counts. A stable counting rate was obtained for the set point at 500 µW for all pressure ranges. For higher pressure levels, the offset must be set to a value of over 300 mV to compensate for the higher threshold of 400 mV at ground pressure levels.

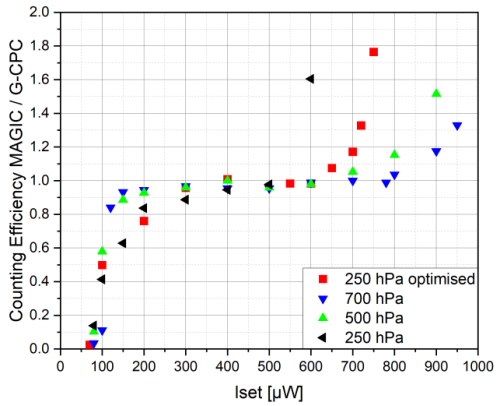

Figure 51. Counting Efficiency response for different initial laser power settings (Lset) and pressure levels for 100 nm particles.

To give an overview of the two particle types we used for the evaluation studies, the aerosol size distribution for the test aerosol is shown in Figure 52.

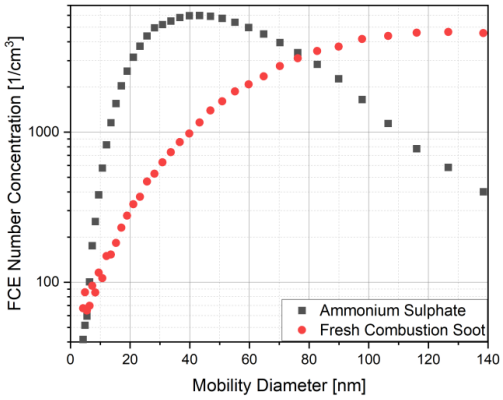

Figure 52. Particle size distributions were measured by Electrometer and sized by DMA for ammonium sulphate and fresh combustion soot. For this work, the particle mobility sizes were measured to 138 nm, so the size resolution at smaller sizes is suitable for the cut-off characterisation. The full particle size distributions are available [42].

To achieve a high resolution for smaller particle sizes, we used the Model M-DMA 55-U. The 8.8 cm DMA tube and a 6 l/min sheath flow as operational parameters determining upper and lower size limits. The upper size limit is at 138 nm mobility particle sizes. This upper size limit sufficient to characterize the ammonium sulphate size distribution, but this size limit covers only parts of the fresh combustion soot size distribution. The ratio of the sample flow to sheath flow rate of 0,12 leads to a narrow mobility size half-width.

The overall counting efficiency, the cut-off diameter and the linearity of the two condensation particle counters are compared to the electrometer used as a reference instrument. This is essential for the instrument validation for IAGOS operation conditions. The measured particle concentrations were compared to the electrometer concentrations corrected for multiple-charged particles. First, we demonstrate the overall efficiency of the instrument by using ammonium sulphate as a particle type. Ammonium sulphate is a common particulate matter compound in the atmosphere. Fresh combustion soot as a second aerosol type is interesting because it may serve as a proxy for anthropogenic aerosol. In particular, the MAGIC should be able to measure non-volatile particle matter emissions from aircraft engines operating on IAGOS. Figure 53 shows the particle size-dependent counting efficiency of the SKY-CPC and the MAGIC 210-LP with respect to the multiple-charge-corrected FCE reference measurements. To offer a clear picture of the cut-off diameter, we do not show detailed data above 50 nm since the instrument reaches a stable plateau of the counting efficiency. In Figure 54, the scatter plot demonstrates the overall linearity between the instruments by using the number concentration distribution visible in Figure 52.

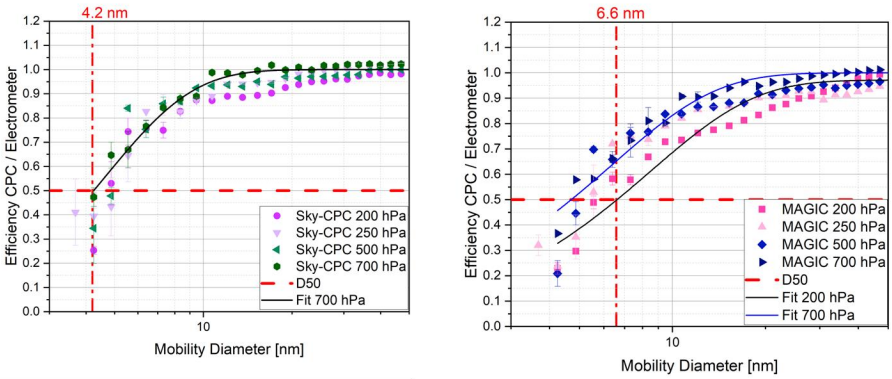

Figure 53. Compilation of the efficiency ratio curves of the Sky-CPC 5.411 (SKY-CPC) (left) and the MAGIC 210-LP CPC (right) to the FCE reference - at different operation pressures as a function of the particle size using ammonium sulphate particles. The variance of the measurement is indicated by vertical bars.

Using ammonium sulphate as a particle material, the instruments respond with an excellent agreement with the FCE reference instrument, with a slope of 1.0 ±0.05 regardless of the inline pressure. The MAGIC 210-LP and the Sky-CPC scatter around the 1:1 line, showing counting linearity for the full spectrum of particle concentrations.

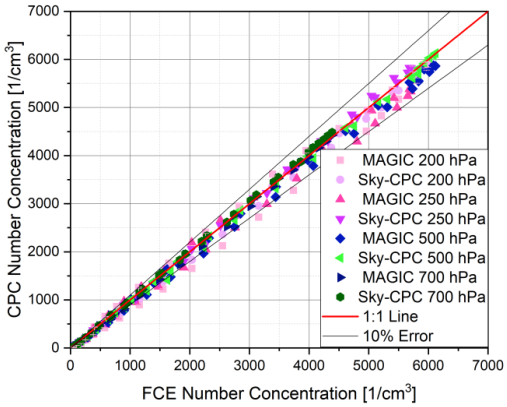

Figure 54. Comparison of the counting linearity between both CPC types and the Electrometer at different pressure levels for nebulised ammonium sulphate.

When looking deeper into the detail at small particle sizes, both CPCs show a D_{50} cut-off diameter of around 5 nm at all pressure levels (see Table 15). The reported D_{50} value is in accordance with previous measurements performed with the standard MAGIC instrument, using ammonium sulphate as aerosol material [113]. When operated at reduced pressures, the SKY-CPC shows no significant change in counting efficiency behaviour. The MAGIC 210-LP counts at least 90% of the particles compared to the electrometer for pressure levels higher than 250 hPa and particle sizes larger than 30 nm. As the operation pressure reaches 200 hPa, the counting efficiency suffers from a small drop to about 80%, but only for particles smaller than 15 nm. The laser power and detector threshold parameters were chosen to cover all pressures down to 200 hPa.

We used combustion soot as a second particle type utilising the Miniature Inverted Flame Soot Generator [95]. We used the second type to show the behaviour of an aerosol that does not dissolve in a liquid. The experimental set-up was therefore adjusted by replacing the nebuliser and its subsequent diffusion dryer with the inverted flame soot generator.

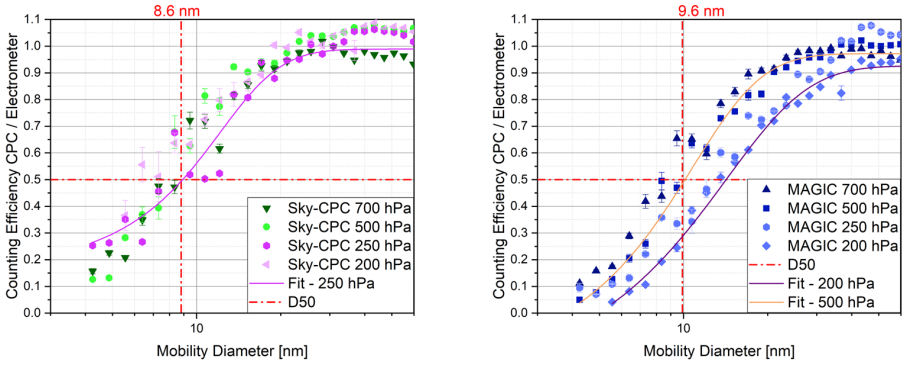

Figure 55. Comparison of the efficiency ratio curves of the Sky-CPC 5.411 (SKY-CPC) (left) and the MAGIC 210-LP CPC (right) to the electrometer reference at different operating pressures as a function of the particle size using fresh combustion soot. The variance of the measurement is indicated by vertical bars.

Figure 55 and Figure 56 show the comparison between the Grimm CPC, MAGIC 210-LP and Electrometer for the freshly generated combustion aerosol at different operating pressure levels. The SKY-CPC and the MAGIC 210-LP show nearly identical behaviour for counting efficiencies at pressures higher than 250 hPa. For lower pressure, the SKY-CPC continues to measure with the same efficiency. As with a gradual shift with decreasing pressure to 200 hPa, the D_{50} cut-off of the MAGIC 210-LP increases to around 15 nm and its D_{90} to about 40 nm.

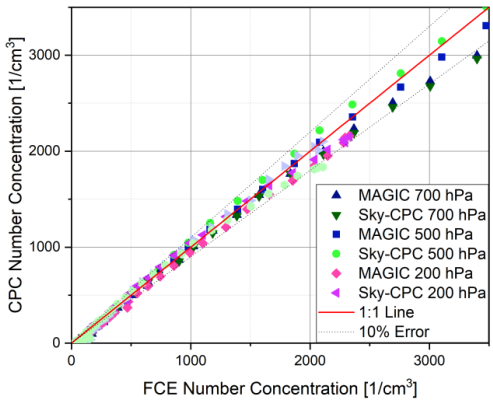

Figure 56. Comparison of the counting linearity between CPC and Electrometer at different pressure levels for fresh combustion soot.

As an insoluble hydrophobic substance, fresh combustion soot is not activated for droplet formation inside a CPC as efficiently as hydrophilic substances [114]. Therefore, soot particles need to be more prominent in diameter for nucleus activation than hydrophilic particles, which explains the increase of the D_{50} compared to our ammonium sulphate experiments. For overall airborne measurements, it is unlikely to encounter fresh combustion soot. The only case where

we have identified fresh soot emissions at these heights are areas of crossing fresh aircraft plume visible as 1-2 second peaks in the timeseries in heavily used flight corridor routes. Furthermore, fresh combustion soot is a good proxy for non-hydrophilic substances.

Table 15 and Table 16 give an overview of the counting linearity of the CPC-type instruments with respect to the FCE reference instrument, for both aerosol types. The Pearson correlation coefficient r^2 never drops below 0.99 for each measurement. Concerning the instrument linearity for soot particles, the MAGIC 210-LP and the Sky-CPC underdetermine particle number concentration compared to the FCE with increasing total number concentrations at 700 hPa. However, this effect was not observed for the other pressure ranges. The average counting efficiency for the 700 hPa trials is still within the overall uncertainty (10%) [115] for all counting efficiency measurements; see parameter A in Table 15 and Table 16 for details.

Looking at the D_{50} value in Table 15 and Table 16, both Instruments show a cut-off diameter close to 5 nm for ammonium sulphate. This agrees with the reported detection limit for both instruments from the manufacturer and publications [107, 116].

The overall trend for the MAGIC 210-LP becomes apparent when looking deeper into the cut-off efficiency measurements. The difference between D_{50} and D_{90} increases with decreasing pressure, resulting in a less steep decrease in the counting efficiency towards smaller particle sizes. This feature then causes a higher uncertainty for measurements of the total number concentration of an aerosol with a strong Aitken mode, particularly for low-pressure surroundings. Whereas the D_{50} value does not change significantly, the D_{90} increases significantly. The overall difference between D_{50} and D_{90} indicates a shallow decrease in counting efficiency over a wide particle size range. Switching the particle type to soot, the lower size detection limits increase because of its less efficient activation.

Table 15. Coefficients of the exponential function of the Counting Efficiency Curves for the Sky-CPC 5.411 (SKY-CPC) and the MAGIC 210-LP CPC and for different line pressure values and ammonium sulphate.

Instrument	Line Pressure	A	B	D_1 [nm]	D_2 [nm]	Equation calculated D_{50} [nm]	Exp. D_{50} [nm]	Equation calculated D_{90} [nm]
SKY-CPC	200	0.96	2	2.8	1.8	4.9	4.8±0.7	9.1
MAGIC 210-LP	200	0.97	2	0.1	5.5	6.6	5.5±0.8	18.2
SKY-CPC	250	1.0	2	1.7	2.6	4.6	5.5±0.8	9.4
MAGIC 210-LP	250	0.97	2	1.6	3.4	5.5	5.5±0.8	12.9
SKY-CPC	500	0.98	2	3.0	1.4	4.6	5.5±0.8	7.5
MAGIC 210-LP	500	0.95	2	2.5	2.2	5.2	5.5±0.8	10.6
SKY-CPC	700	1.0	2	1.5	2.5	4.2	4.3±0.7	8.9
MAGIC 210-LP	700	1.0	2	0.1	4.1	4.6	4.3±0.7	12.3

Table 16. Coefficients of the exponential function of the Counting Efficiency Curves for the Sky-CPC 5.411 (SKY-CPC) and the MAGIC 210-LP CPC for different line pressure values and fresh combustion soot.

Instrument	Line Pressure	A	B	D_1 [nm]	D_2 [nm]	Equation calculated D_{50} [nm]	Exp. D_{50} [nm]	Equation calculated D_{90} [nm]
SKY-CPC	700	0.92	1.2	5.9	3.2	8.0	7±1.0	19.0
MAGIC 210-LP	700	0.93	1.4	5.9	3.6	8.7	9±1.3	19.7
SKY-CPC	500	1.02	2	3.6	3.8	7.6	8±1.0	14.2
MAGIC 210-LP	500	0.97	2	3.6	5.2	9.6	9±1.3	21.0
SKY-CPC	250	0.99	0.94	9.2	4.2	8.6	7±1.0	19.1
MAGIC 210-LP	250	1.03	2	3.3	8.9	11.9	11±1.4	27.6
SKY-CPC	200	1.01	1.03	6.6	4.2	6.7	5.5±0.8	15.9
MAGIC 210-LP	200	0.93	2	3.8	7.6	13.4	13±1.5	35.7

Analysing the behaviour of the fitting parameter A, which represents the plateau of the fit function, and the derived parameter D_{50} of the fitting function in Table 15 and Table 16, no clear trend is visible for the two aerosol types and instruments. The values of D_{50}, deduced from the fitting curves, are close to 5 nm for both condensation particle counters and all pressure levels in the case of ammonium sulphate (Table 15) and fit the experimental data. For fresh combustion soot (Table 16), D_{50} values for the Sky CPC instrument are slightly larger at a value of 8 nm, while for the MAGIC 210-LP, the increase in D_{50} compared to ammonium sulphate is more pronounced. Overall, the agreement between values derived directly from the experiment and values deduced from the fitting procedure is within the error margin of the individual mobility size.

At lower pressures, the particle counting efficiency drops for small particle sizes in the Aitken mode range and below. Because of particle line losses during sampling, the overall efficiency of the measurement system is determined by the instrumental efficiency times the inlet efficiency. Thus, inlet line loss impacts the quality of the measurements directly. In case of the foreseen application of the instrument onboard passenger aircraft equipped with IAGOS instruments using a sampling line of more than 1 meter length line losses are significant: Here 50% (85%) of 5 nm (13 nm) particles will penetrate to the instrument (at 150 hPa, and 2.4 L/min total flow) [55] mostly caused by diffusion losses. We show curves for the expected inlet efficiencies, including losses, in the SI (see Supplementary Information Figure 5). Yet, the overall uncertainties must be determined by modelling MAGIC 210-LP and Sky CPC instrument responses for different aerosol size distributions, mainly with and without a nucleation mode, for IAGOS–characteristic sample line lengths.

8.2.3 MAGIC low-pressure application summary and recommendations

The MAGIC CPC was recently introduced as a new water-based CPC with excellent overall performance compared to a standard Butanol CPC [109, 116]. In this work, we characterised a modified "LP" (Low Pressure; Version: MAGIC- LP 210) model of that water-based CPC design for flight altitude pressure levels as low as 200 hPa. We recommend testing each unit for low-pressure applications and adjusting the manufacturer settings when operating at pressures lower than 500 hPa if necessary. The factory settings were sufficient for operating the instrument at pressures >500 hPa. We briefly examined the performance of five MAGIC-LP 210 units at laboratory pressure and found that the inter instrumental scatter plots follow the 1:1 correlation between unit. However, a side-by-side analysis of the cut-off diameter for different pressures has not been performed yet. For the units we tested, we found that laser power and detector threshold are critical for a high counting efficiency at all tested pressures. It is noted that since this study, the manufacturer has acted on the insights from this work and modified the firmware and design of the MAGIC 210-LP we tested to improve the performance at high altitudes. Automatic adjustments in the laser and detector settings with operating pressure were incorporated in the newest model MAGIC 250-LP. We will apply these new settings as part of the evaluation of the additional MAGIC-LP 210 models planned for the IAGOS payloads and recommend this for all low-pressure applications of the MAGIC 210 LP.

The MAGIC 210-LP operates at all pressure levels tested and reports reliable particle concentrations with overall detection efficiencies close to 100% for particles larger than 40 nm. For the continuous operation on IAGOS aircraft packages, its water recycling mechanism makes the instrument attractive for long-term operation in harsh conditions with limited opportunities for instrument access and maintenance. To evaluate the instrument performance, and in particular, the counting efficiency, as a function of the aerosol type and pressure, an aerosol electrometer and a butanol condensation particle counter were used as established reference instruments. For ammonium sulphate particles, the MAGIC 210-LP CPC shows excellent stability of the D_{50} cut-off diameter and overall linearity with an r^2 of 0.99. Verified by experimental data and shown with parameters of an exponential function, the overall counting efficiency reaches 100% for pressure levels higher than 200 hPa and particles larger than 30 nm, regardless of the particle type. However, at 200 hPa, the counting efficiency for particles smaller than 30 nm drops notably to 90% compared to the electrometer or the butanol CPC. When the MAGIC 210-LP is exposed to a hydrophobic and insoluble particle type like fresh combustion soot, the water condensation particle counter shows similar behaviour for almost all particle sizes down to 30 nm for ambient pressure levels down to 250 hPa with linearity within 95%. This pressure range covers the operational conditions present during IAGOS aircraft flights. For pressures down to 200 hPa, the efficiency of the MAGIC 210-LP reaches 100% linearity towards the reference instrument for an extensive particle range. For particles smaller than 30 nm, the counting efficiency is lower than 90 %, decreasing to 70% (60%) for 20 nm (15nm) particles. Because of the reduction of the counting efficiency for particles smaller than 30 nm for operational pressure levels below 250 hPa, the uncertainty of the reported number concentration is enhanced, particularly when sampling an aerosol with a strong nucleation mode, and the lower counting

efficiency of the MAGIC 210-LP for smaller particle sizes results in a higher uncertainty of the total particle count.

8.3 Particle loss considerations

The final sampling line loss during operation on the aicraft is the product of two settings. Here, the main aerosol sampling line with a flow rate of 4 l/min for the final instrument package and a length of 1 meter till the splitting point, where the MAGIC-LP has a flow rate of 0.3 l/min and 30 cm distance. An aerosol size distribution was folded with the transmission functions for line losses at 1013 and 200 hPa shown in Figure 57.

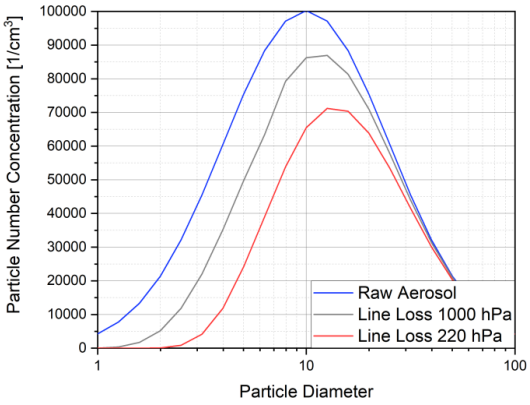

Figure 57. Particle Line Loss calculations for 1000 hPa (Ground) and 220 hPa (Air).

Aerosols tends to impact, sediment or are lost by diffusion with the walls of the tubing. The airflow and the length of the tube are crucial for the sampling line losses. The length of between the instrument package and the aerosol inlet was estimated to 0.7 m and from the aerosol inlet towards the condensation particle counter of around 30 cm. The air flow of the instrument package is around 4 l/min, whereas the MAGIC is limited to 0.3 l/min. Those values were used in the line loss calculation shown in Figure 57.

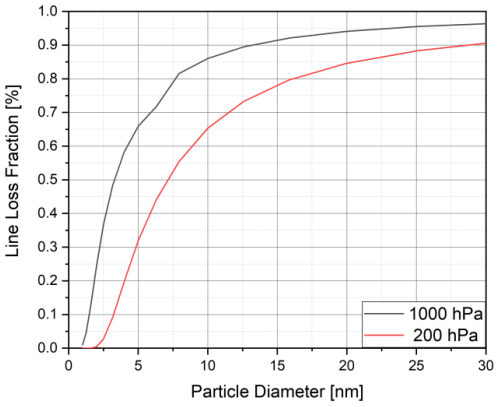

Figure 58. Fraction of the particles that are transmitted through the inlet line for two different pressure levels at ground-level (P=1013 hPa and cruising altitude P=200 hPa considering diffusion losses only.

Figure 58 shows the ratio of the raw aerosol towards the aerosol that can pass the tube without wall impaction in dependence of its particle diameter. Particles with a diameter of 13 nm experience a loss of 10% at a pressure level of 1000 hPa. At 220 hPa, same diffusion loss is enchanted and particles with a diameter of 26 nm are at 90% loss rate.

8.4 Portable Optical Particle Spectrometer

The Portable Optical Particle Spectrometer (POPS) is a light-weighted optical particle sizer designed to measure individual particles in the size range of 140 nm to 3 µm[71]. It was originally developed by Ru-Shan Gao [71]. With our enhancements the instrument has an extended range of 125nm – 4µm and is able to withstand the pressure difference between cabin air and cruising altitude pressure levels onboard an airplane and was custom-built in our laboratory.

This device was chosen to be one essential part of the air quality package 2e. The most convincing characteristics of this instrument are besides of the reliable measurement principle, its small size, weight and power consumption. It is operated with a 405 nm laser diode, which give it an advantage towards the Grimm optical particle counter operated at 655nm. An overview of the instrument can be seen in Figure 59. The Laser beam crosses the sample volume orthogonally and is distinguished in a light trap. A mirror is placed beneath the optical active sampling volume to redirect the scattered light with a scattering light intergrading volume of 30° into the photomultiplier tube (PMT).

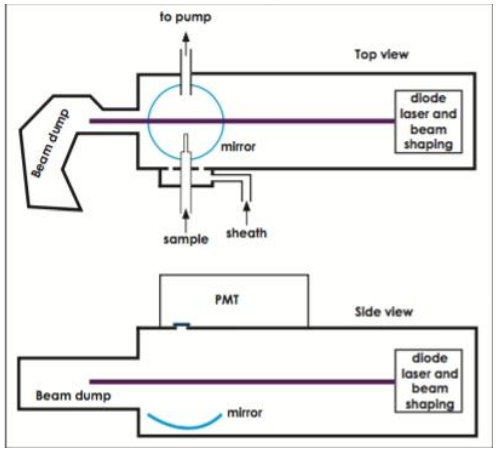

Figure 59. Simplified overview of the core components of the POPS.

In Figure 60 a more detailed picture of the components can be viewed. Between the laser diode and the sample volume, four slits are located, which focus the laser and reduces scattered light, which would perturb the measurements.

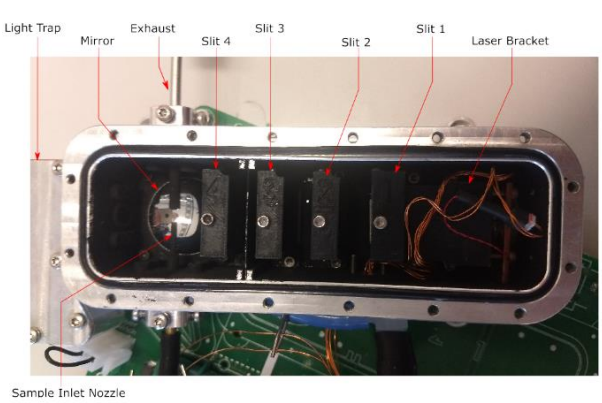

Figure 60. Top view of the POPS components.

The instrument measures the voltage of the PMT. Without particles, this electronic device has still a background level of white noise. This level depends on the gain factor of the PMT adjusted by the driving electronics. An observed voltage peak in the time series of the PMT signal corresponds to a particle passing through the sampling volume and scatter the light of the laser diode. This scattered light is proportional to the intensity of radiation and analysed by the software of the POPS. To be counted as a particle signal, the peak must be higher than 40 arbitrary units above the baseline, indicating the lowest channel boundary. In Figure 61 this mechanism is illustrated with its pressure dependency. While the baseline has a small drift of around 70 a.u. from 1000 hPa to 200 hPa, the lower channel boundary is coupled with this behaviour. This means, there is no effective pressure dependency.

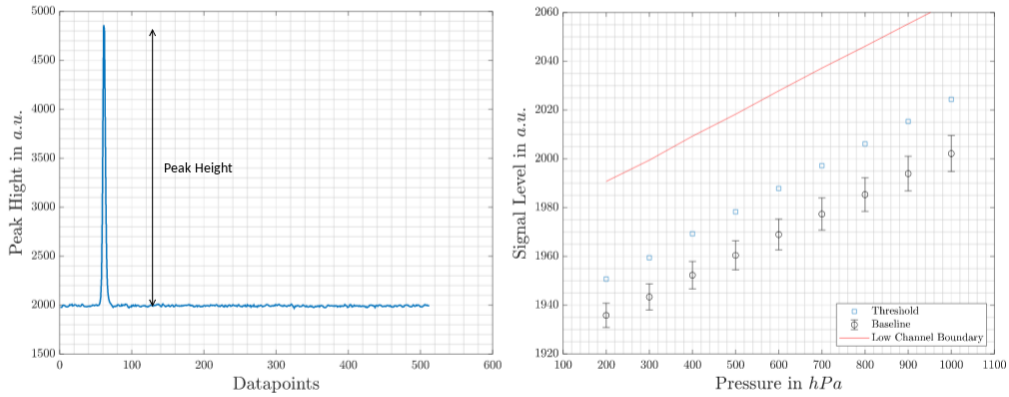

Figure 61. Illustration of raw data of a single particle (left) and the baseline shift at different pressure levels (right).

The Device was calibrated with PSL particles like the CAPS PMex. For this device, the intensity of the signal is equivalent to an optical size. Since the size of the PSL particles are known, those can be related to an instrument response. For a first view, the number of channels is enlarged to 100 to visualise the instrument response in a better way. This is shown in Figure 62 and with a larger PSL size, the particle response is sorted in a higher channel as well.

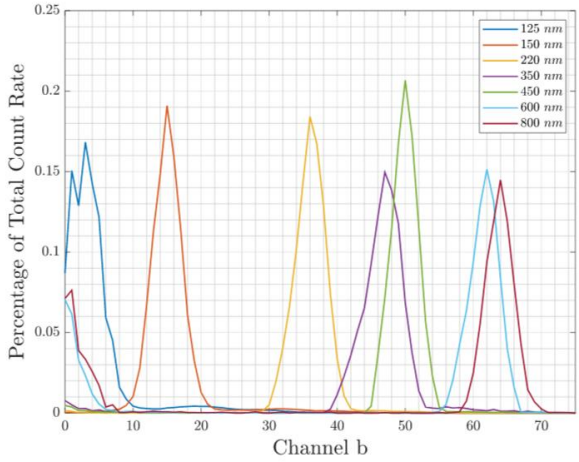

Figure 62. Measurements of different PSL diameters with the POPS channel response.

The raw signal is monitored and can be used for calibration. In a self-written MATLAB code, the raw data can be read, averaged, and calibrated with the PSL particle size. At a last step, the calculated Instrument response curve using the geometry of the optical arrangement using Mie theory to scattering calculation were visualised. With this step it, the calibration curve can be fitted, and it is visible, if parameters for the POPS code or hardware had to be adjusted. Those adjustments include the laser power or thresholds for detection limits. A well fitted curve with reported particle responses and PSL sizes is visible in Figure 63.

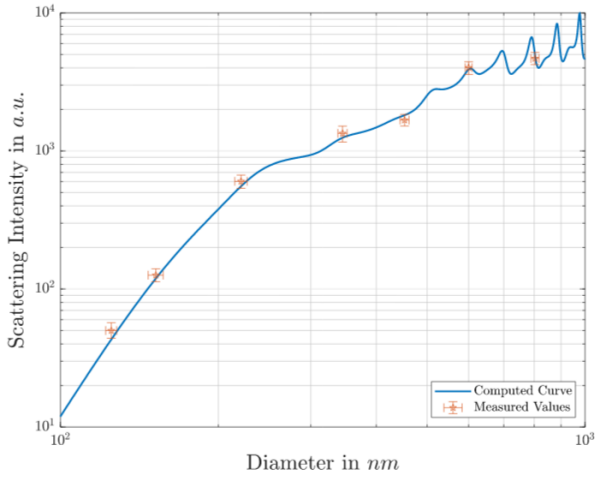

Figure 63. Computed Mie curve with measured raw data.

In a last step, the over a broad angel smoothed calculated instrument response curve is used to assign the measured scattering intensity to a channel. This is done for any number of channels. The procedure outcome can be viewed in Figure 64.

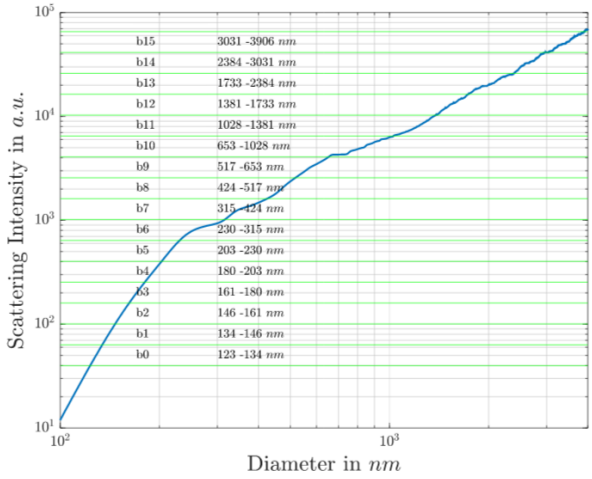

Figure 64. Matched Scattering intensity with 16 channel boundarys.

The final goal of getting a series of POPS operational needs the unification of the data output. Therefore, the configuration file located at the SD-card data storage is used to store individual parameters adjusted during the calibration/initialization process. Three parameters are useful to reach a unification. The laser power can be controlled, as well of the highest and lowest count threshold that particles have to reach to be counted as a particle.

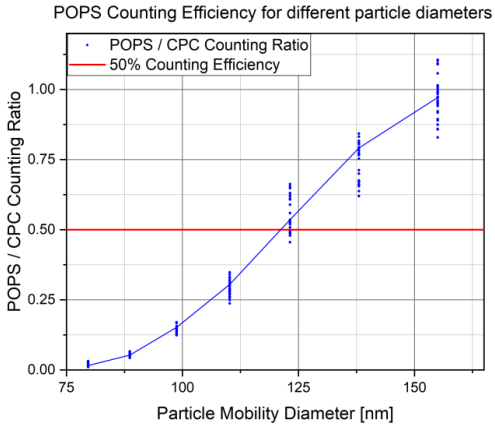

Figure 65. POPS Counting Ratio against the MAGIC-CPC.

The Counting efficiency of the POPS as function of Particle size is shown in Figure 65 in comparison with the MAGIC-CPC. As mentioned earlier, the POPS reaches its $D_{50\%}$ cut-off at a particle diameter of 123 nm and can reach 100% counting efficiency for particles larger than 140 nm.

On the more technical aspects of the individual components of the IAGOS air quality package, the behaviour and reduction of false counts for larger particles has to be explored for measurements for the optical particle sizer POPS. It was observed, that for high scattering intensity, the data output of the POPS is measuring additional smaller particles. Those small particles in the lowest size channels are visible in the raw data but are too close to be real particles. This however is an issue for all optical particle counters and is shown in Figure 66. To meet this problem a software-based step is considered to eliminate close-by peaks, that are misinterpreted as particles, by adding a minimum time distance between peaks.

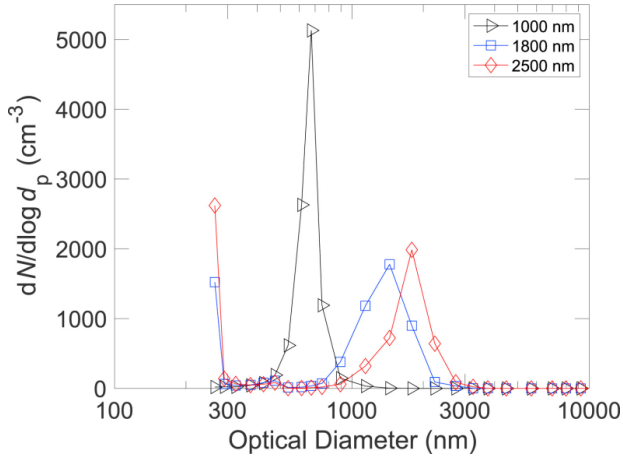

Figure 66. Data output of OPC for monodisperse aerosols measured by Sang-Nourpour (2019) [117].

9 A new Working fluid substituting Butanol

IAGOS operates two instrument packages that are capable of measuring aerosol properties. The first package that was custom designed for this application was designated P2c. The design of P2c allowed it to measure the aerosol number concentration as a volatile and non-volatile fraction as well as the size distribution with some limitations [50]. In-situ aerosol measurements are a necessity for the atmosphere research [118, 119]. The package 2c was developed to cover the gas to particle conversion with the total number concentration. The volatile to non-volatile particle ratio gives hints e.g. about the anthropogenic aerosol contamination of the atmosphere [120]. The aerosol size information is important to cover the number of particles, which are available for condensation growth and cloud formation [121, 122]. P2c was later replaced by the newly developed instrument package P2e.

The requirements to the packages are manifold [50]: The instruments have to operate with no supervision, automatically and with no maintenance over at least three months. The packages have to operate at an altitude equivalent of 170 hPa. The size of the box is limited to 56 x 40 x 28 cm and has to weigh less than 30 kg. All materials that are used inside the boxes have the requirement of zero flammability.

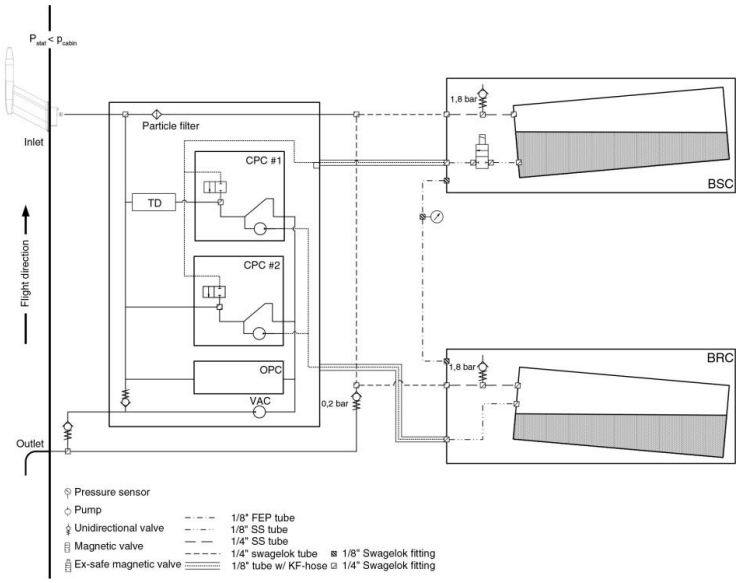

Figure 67. Schematic of the package 2c [50].

Figure 67 shows the flow chart of the aerosol package 2c. It operates with two butanol-based condensation particles counters and an optical particle counter for the size range of 250 nm to 3 µm. The butanol containers (BSC; BRC) are the very reason for the issues occurring with aerosol package 2c certification. The characteristics of butanol make it a great working fluid for the

operation pressure ranges from 1000 hPa down to 200 hPa, but its flammability is the reason, why the package 2c is no longer allowed to operate on passenger aircraft. The day we became aware of this information in mid-2022, my supervisor Ulrich Bundke approached me about what substitute working fluid I would put in a condensation particle counter with similar physicochemical properties. With my background as a chemist, I immediately reported several substances. The following section will report the findings of a small laboratory study.

9.1 Dimethyl Sulfoxide as A New Working Fluid

This chapter is based on the manuscript: Weber, P., Bischof, O. F., Fischer, B., Berg, M., Schmitt, J., Steiner, G., Keck, L., Petzold, A., and Bundke, U.: A new working fluid for condensation particle counters for use in sensitive working environments, Aerosol Research, 1, 1–12, https://doi.org/10.5194/ar-1-1-2023, 2023.

This manuscript proposes a promising substance to substitute butanol in condensation particle counters. The proposed new working fluid is not unknown to the community, since it is an intermediate step of the well-known chemical reaction beginning with DMS (dimethyl sulfide). Its final product is sulphate, which functions as a cloud condensation nuclei [123]. Enhanced DMS emissions are caused by enhanced phytoplankton growth by an increased ocean temperature. The enhanced earth albedo by the DMS induced cloud formation introduce a negative climate feedback stabilizing the Ocean temperature (CLAW-hypothesis of Charlson et al. (1986))[124]; Dimethyl sulfoxide (DMSO) is therefore an omnipresent chemical for atmospheric science.

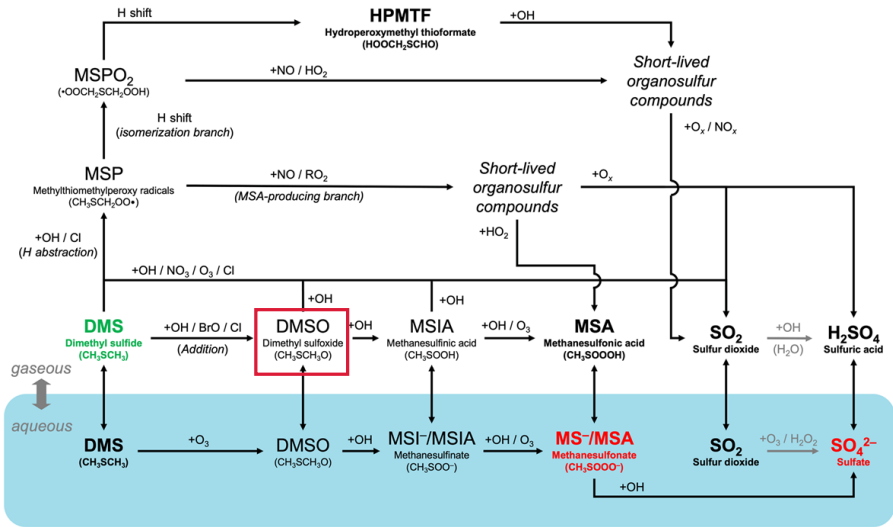

Figure 68. Schematic of the chemical reaction of DMS and DMSO in the atmosphere and aqueous mediums [123].

Our search for a new, non-toxic, non-flammable, odourless working fluid was motivated by the requirements of aviation authorities that severely restrict the use of instrumentation on passenger aircraft. The European research infrastructure “In-Service Aircraft for a Global

Observing System" (IAGOS; www.iagos.org) has been created to monitor essential climate variables of the atmosphere, including aerosol particles [125]. The monitoring takes place through regular and global-scale measurements conducted on board a fleet of commercial passenger aircraft equipped with automated scientific instrumentation. The IAGOS aerosol package "P2c" uses a butanol-based CPC as described in detail by Bundke et al. (2015) and provided two years of measurement onboard the IAGOS CARIBIC flying laboratory. It obtained special permission of German airline Lufthansa and its use included the observation of the Raikoke volcanic ash plume. However, the fact that butanol is a flammable liquid strongly hinders the international certification of this instrument for use aboard passenger aircraft.

This study is part of the ongoing development of the IAGOS aerosol instrument, in response to these flight safety aspects. For the next generation of the IAGOS aerosol package, we will operate two butanol condensation particle counters (model 5411 Sky-CPC; Grimm Aerosol Technik, Ainring, Germany, a variant of Grimm model 5410 CPC using aviation-grade components and materials) alongside an optical particle counter (OPC, model 1.129, Grimm). One CPC is dedicated to measure the total aerosol concentration and the other is equipped with a thermodenuder operated at 250 °C upstream to measure only the non-volatile fraction of aerosol particles.

The new working fluid dimethyl-sulfoxide (DMSO; C_2H_6OS; CAS-Nr. 67-68-5; 99,9%) that we introduce in this study is hitherto unknown for use in a CPC. The principal benefit of DMSO for use on passenger aircraft is that it does not require any safety regulations according to the Globally Harmonized System of Classification and Labelling of Chemicals. According to this internationally agreed-upon standard, it does not have any physical or health hazard characteristics. Therefore, this working fluid does not present an obstacle during the certification process for aviation operation. An effect on measuring stations, that observe DMSO and DMSO products, is considered as minimal as the amount of DMSO released by the CPC exhaust in the environment, compared to the natural background.

9.1.1 Introduction to CPC Working Fluid Characteristics

A working fluid's physical characteristics are important for condensation particle counter performance. For all working fluids, the detection efficiency has been characterised over a specific range of operating pressures [55, 126-128] which demonstrated the applicability of each working fluid for low-pressure operation CPCs. It should be noted that both butanol and isopropanol have a strong, unpleasant odour and adverse effects when inhaled over prolonged periods and that their use is limited by the fact that both are highly flammable liquids. In contrast, water has the advantage of avoiding the health and safety concerns of alcohol. The disadvantages of water are that it has a three times higher mass diffusion coefficient [113, 129] which increases the consumption of the working fluid during operation and the possible growth of organisms during prolonged times of inactivity. Further with water as the operating fluid, the activation of particles can be hindered, e.g. by aerosol properties like water solubility and lipophilicity. In the past, there were several attempts to find an optimal working fluid. A theoretical approach for working fluids was demonstrated by Magnusson et al [130] including mostly alkanes, organic acids, aromatic

compounds and alcohol substances, while sulphuric compounds were not included. Diethylene Glycol (DEG) was discovered by Iida, et al. [131] with great application for sub 3-nm particles, but droplets only grow to very small sizes, so a "booster" CPC is needed. Dibutylsebecat (DOS/DEHS) and more substances were tried by Kupper, et al. [132] with the advantage of not being classified as hazardous by the international Globally Harmonized System (GHS), but those were only applicable for high temperature (above 100°C) in the CPC saturator.

One governing parameter is the maximum saturation ratio which can be achieved in a specific CPC design. Our first objective was to find a substance with similar physical-chemical properties to butanol or water, which are widely used as working fluids in condensation particle counters. The second motivation was to address any safety restrictions that make the working fluid suitable for sensitive working environments such as hospitals, schools, public spaces, industrial manufacturing, but also commercial passenger aircraft. DMSO was eventually identified as a candidate substance based on the authors' experience with organic solvents. Besides the advantages of not having any physical or health hazard characteristics, DSMO is also soluble in water. Therefore, the relatively high freezing point of DMSO of 18°C can be adjusted to -100°C or even below simply by adding a defined amounts of water [133].

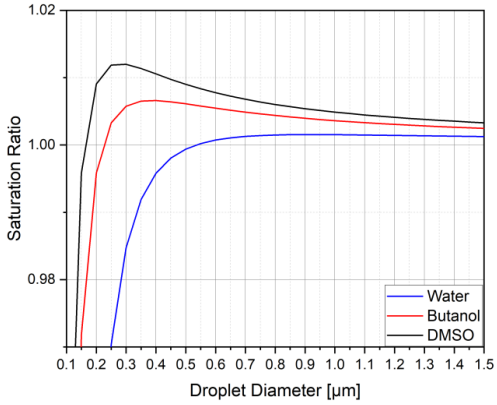

Figure 69. Saturation ratio of three working fluids as a function of the droplet diameter for a sodium chloride particle with an initial diameter of 13 nm [23]. For DMSO, a surface tension of 0.043 N/m, a molecular weight of 0.078 kg/mole and the liquid density of 1100 kg/m^3 is used CRC Handbook, [134].

To understand the influence of the working fluid on the activation process inside a CPC, the process can be summarised as follows. The vapour pressure above the curved particle surface is described by the Kelvin Köhler equation[46] as visualized in Figure 69 and calculated with EQ 22. Here the saturation ratio is defined by the ratio of the actual vapour pressure to the vapour pressure above a flat surface at a given temperature. Particles smaller than the critical diameter grow or shrink in equilibrium with the vapour in their vicinity. If the critical saturation ratio is exceeded in the particle vicinity the particle will grow past the critical diameter. If the saturation ratio is above 1 (i.e., supersaturation) then the particles will experience non-equilibrium growth. This process is known as particle activation. The critical supersaturation depends on the initial

size of the aerosol particles and will be higher for smaller particles [23]. As shown in Figure 69, the saturation ratio necessary to activate a sodium chloride particle of an initial size of d_p = 13 nm is at 1.012 for DMSO, 1.007 for butanol and 1.002 for water. The necessary supersaturation for activation increases with decreasing particle size. For example, for DMSO, particles with diameters 6 nm and 3 nm require saturation ratios of 1.037 and 1.078, respectively. Solving the Antoine equation for two temperatures and taking the ratio of the two results yields the supersaturation for this calculated temperature difference. For DMSO, the component-specific constants are a= 5.23; b= 2239.2; and c= -29.2 [135].

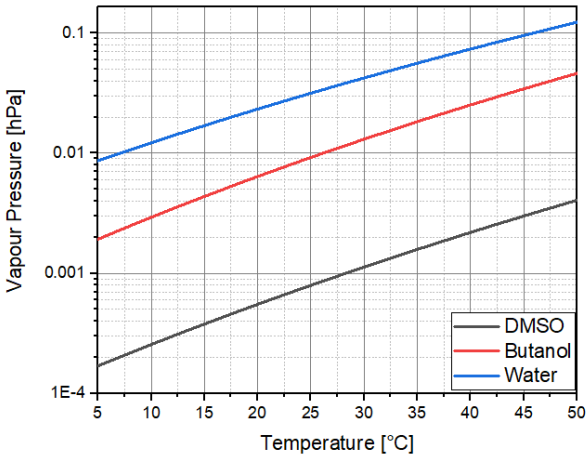

Figure 70. The theoretical saturation vapour pressure of butanol, water and DMSO as calculated by the Antoine equations [47, 136].

As can be seen in Figure 70 and calculated with EQ 23, the saturation vapour pressure of DMSO is far below that of butanol, but with a similar slope of 0.031, while the slope is 0.026 for water. This indicates the same supersaturations could be achieved with the same temperature difference between the saturator and condenser of condensation particle counters, but with a much lower consumption of the working fluid. For DMSO, we achieved a supersaturation of about 10% (saturation ratio of 1.1) with a saturator temperature of 40 °C and a temperature drop to 5 °C in the condenser part of the CPC used. We are not certain if the signal is generated by droplets or solid crystals, because the freezing point of DMSO is below the condenser temperature.

The working fluid was tested on the flight simulation test stand shown in Figure 43, by replacing the working fluid of one CPC unit with DMSO.

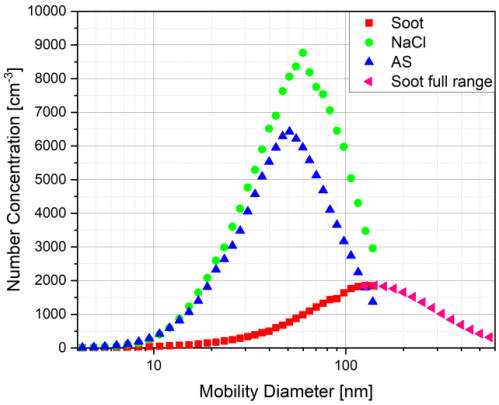

Figure 71. Particle size distributions of ammonium sulphate (AS), sodium chloride (NaCl) and fresh combustion soot as measured by the combination of DMA and electrometer.

As mentioned earlier, the atomiser was used to nebulise salt solutions. Sodium chloride (NaCl) and ammonium sulphate were both used for this purpose. Additionally, fresh combustion soot was measured. In Figure 71, the corresponding size distributions for these aerosol types are shown. The DMA settings were chosen, to provide the greatest possible size resolution at the smallest particle sizes near the range of the expected cut-off diameters. This resulted in a maximum particle mobility size of 138 nm on the upper end for the salts and for the soot. Complete particle size distribution for the soot were taken from previous experiments [42].

9.1.2 DMSO Droplet Size

The SKY CPC 5.411 reports an internal diagnosis of the particle growth which is displayed as the C1/C0 value. The C1/C0 reports the ratio of counts that have a higher and a lower detection threshold, which is used as CPC-internal check for sufficient particle growth (described in Fig 6.). A value below 1 indicates, that the particles give a lower scattering signal due to a smaller particle size or due to overall light scattering behaviour. Only particles reaching and exceeding both signal threshold levels are counted. The C1/C0 correction is implemented simply by dividing the reported number concentration through the C1/C0 value. In Figure 72, signals of different droplet sizes are illustrated, along with detector thresholds C0 and C1. By dividing the reported number concentration by C1/C0, the CPC counts all particles that reach the first detector threshold. DMSO droplets smaller than 2.5 µm will not be counted.

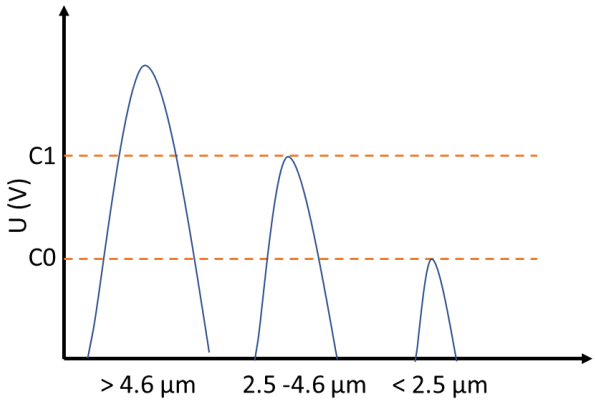

Figure 72. Illustration of the pulse height of DMSO-Droplets of different sizes with corresponding detector threshold levels.

The very need for this correction is due to the low vapour pressure of DMSO. If less material is available for condensation growth, the droplets cannot grow. The diameters of the DMSO droplets, which correspond to the signal heights of C0 and C1, are 2.5 – 2.9 µm and 4.0 – 4.6 µm respectively to the different thresholds. The values were estimated from the signal heights of latex test particles, a model for scattered light intensities as a function of particle diameter for the Grimm measuring cell, assuming spherical homogeneous particles, a wavelength of 660 nm, linear polarization, and refractive indexes of 1.59 + 0.0i for latex and 1.47 + 0.0i for DMSO.

To parameterise the efficiency curves, an exponential fit function [137] was applied

$$\eta = A(1 - \exp\ \frac{(B - Dp)}{(C - B)} ln2) \qquad \text{EQ 57}$$

Here, η is the counting efficiency, D_p is the particle size, and A, B, C are fitting parameters calculated using a multi-parameter fit [110, 111] where C corresponds to the D_{50} cut-off diameter.

The fitted function was then used to robustly calculate the efficiency for the cut-off of D_{90}. This Equation is an updated formular of EQ 56 with the advantage of getting the D_{50} cut-off diameter directly.

9.1.3 Summary and Results of CPC measurements using DMSO

During initial experiments we used DMSO from a bottle of our laboratory stock that was first opened two years prior to these experiments. We started by completely drying a Sky CPC 5411. Prior to filling it with DMSO, we performed a test run in the measurement setup and the dry CPC reported zero counts. The instrument wick was then wetted with DMSO by the refilling valve and worked as intended. The CPC internal fluid controls operated as they do with butanol. We operated this unit, which from now on we refer to as the D-CPC, with the same parameters as the structurally identical B-CPC which was also included in the experimental set-up. For the first run we applied a particle filter to the inlet to check for homogeneous nucleation. No particle

counts were observed during zero particle air measurements, independent of instrument temperatures, humidity, or pressure levels. As we started aerosol measurements with pressure levels below 700 hPa, the C1/C0 value decreased to 0.9 and dropped further down, as soon as the pressure decreased. As a consequence, we increased the saturator temperature from 36°C to 40°C and decreased the condenser temperature from 10°C to 5°C. With this procedure, the C1/C0 value stayed at 1 down to a pressure level of 250 hPa and only decreased slightly to 0.95 at 200 hPa. All values given as number concentration from the D-CPC are corrected by dividing by the C1/C0 value in order to report all particles at the lower counting threshold as explained previously. The initial results were obtained with ammonium sulphate particles. The D_{50} cut-off diameter is used as the primary criterion, as it describes the particle size where only 50% of the particles are detected compared to a reference method. Figure 73 shows that the D-CPC has an identical D_{50} cut-off diameter as the B-CPC.

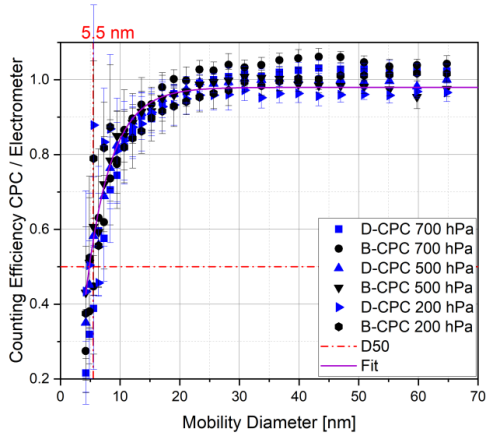

Figure 73. Counting efficiency curves of the Sky CPC 5.411 operated with butanol (B-CPC) and DMSO (D-CPC) at different operation pressures using ammonium sulphate particles.

As second step, we tested DMSO in a CPC of a different kind. For the CPC 3772-CEN the main operating principle is the same, but there are slight differences to the Sky-CPC. The Sky-CPC has a horizontal wick and a continuous draining of condensed water/butanol mixture located downstream of the saturator working fluid reservoir. The 3772-CEN has a vertical wick, where condensed water may flow through before reaching the fluid reservoir. This different design will explain some differences we observed during long-term experiments described later on. To start with, we dried the 3772-CEN for over two days until no particle counts were reported. We then added the DMSO. We changed the temperature parameters to be equivalent to the D-CPC with 40°C at the saturator and 5°C at the condenser. Therefore, the 3772-CEN was not operated as intended by the European Committee for Standardization (CEN). In order to highlight this, we will refer to the 3772-CEN operated with DMSO as the D-CEN. As shown in Figure 74, counting efficiencies for all CPC´s do not significantly differ from each other, regardless of the instrument and applied pressure.

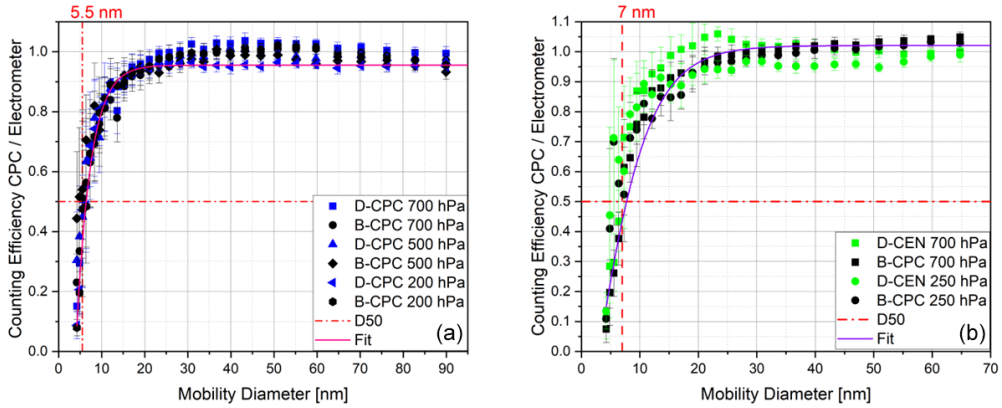

Figure 74. Counting efficiency curves for sodium chloride particles with respect to the electrometer reference instrument and corrected for multiple charge of the Sky CPC 5.411 (a) as well as for the CPC 3772-CEN (b), both operated with butanol (B-CPC) and DMSO (D-CPC; D-CEN) at different operating pressures.

To test another particle type, we chose fresh combustion soot aerosol, as it is a non-soluble substance and is not hydrophilic. As in the previous experiments, the counting efficiencies for the different CPCs do not differ (Figure 75).

We repeated all experiments using a mixture of 10% volumetric water to 90% DMSO in the Sky CPC 5.411 (points labelled as DW-CPC in Figure 75). This mixture does not influence the measurement performances. We observed, that the C1/C0 value decreased to below 0.2 for about a minute as soon we reached pressure levels below 250 hPa, indicating that water is evaporating and influencing the particle growth. After a span of one minute, the C1/C0 value rapidly increased to over 0.98. Using this mixture, the lower range of operating conditions is extended to -10°C.

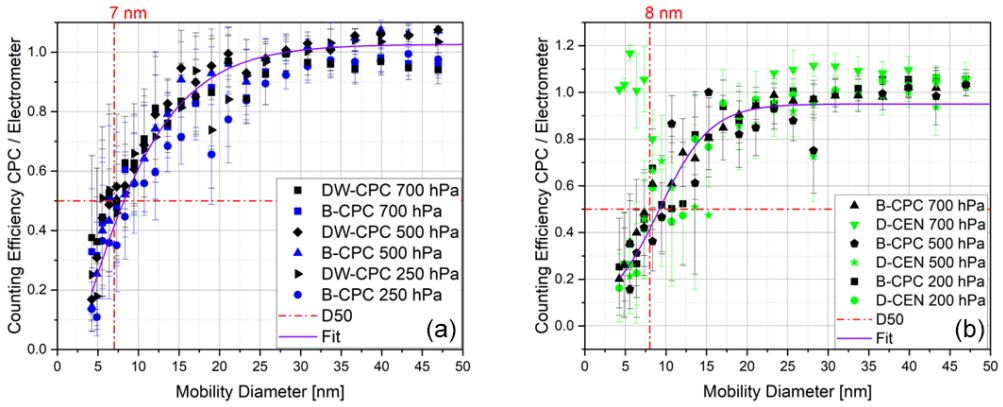

Figure 75. Counting efficiency curves with respect to the electrometer reference instrument and corrected for multiple charges at different operating pressures using fresh combustion soot particles for (a) Sky CPC 5.411 operated with butanol (B-CPC) and mixture of DMSO and water (DW-CPC) and (b) Sky CPC 5.411 operated with butanol (B-CPC) and the CPC 3772-CEN operated with DMSO (D-CEN).

The counting efficiency of the D-CEN for soot particles at 700 hPa exhibits a sudden increase at around 5 nm as shown in Figure 75b. This phenomenon needs further investigation because it could not be explained.

We tested DMSO in our measurement set up at various conditions. For example, we increased the inline humidity (RH) to 30%, although we normally measure at RH below 5%. Even then, the counting efficiencies as well as the overall behaviour did not change. The instrument cut-off diameters for D_{50} and D_{90} do not differ significantly from each other regardless of particle type, operating fluid or pressure level. In Table 17 the fitting parameters and the derived values for the D_{90} cut-off diameter are reported for the lowest pressure level studied (either 200 hPa or 250 hPa, depending on experiment). The significant parameters for the high of the plateau (A; ±0.05) and the cut-off diameter D_{50} (Parameter C; ±1.5) did not change significantly at different pressure levels (200 – 700 hPa) and humidity levels (0-30 % RH).

Table 17. Coefficients of the exponential function of the counting efficiency curves and the D90 cut-off diameter (at either 200 or 250 hPa) for different particle types for the Sky CPC 5.411 operated with Butanol (B-CPC) and DMSO (D-CPC); DMSO-Water mixture (DW-CPC) and CPC 3772-CEN operated with DMSO (D-CEN).

Particle Type	Instrument	A	B	C [nm]	D_{90} [nm]
NaCl	B-CPC	0.99	3.9	6.7	13.6
NaCl	D-CPC	0.96	3.9	6.3	13.5
NaCl	D-CEN	1.02	1	6.7	18.6
AS	B-CPC	0.98	2.1	4.8	11.9
AS	D-CPC	1.02	2.8	6.5	14.2
Soot	B-CPC	0.95	3.4	6.8	17.8
Soot	DW-CPC	1.02	2.7	5.6	11.7
Soot	D-CEN	0.95	3.7	7.5	19.8

After the characterization in the lab we conducted several measurements of outside air at the campus of Forschungszentrum Jülich. The longest measurement lasted 5 consecutive days, both the D-CPC and the B-CPC measured the same particle concentrations (Figure 76a). We observed that the 3772-CEN had issues during the measurements caused by DMSO. Here the valves for draining and priming got blocked by a swollen gasket. First of all, we needed to extract excess fluid from the device manually. Since the overall ambient humidity ranged between 60 and 80%, it is certain that water condensed at the condenser and dropped into the wick of the 3772-CEN, weakening its activation efficiency. This is seen in Figure 76b, where the D-CEN trace is lower than the B-CPC trace starting around minute 45. Because DMSO appears to affect the drain and priming valve gaskets the instrument needed to be manually drained (minute 60 to minute 80 in Figure 76). After that, the 3772-CEN returns to the same concentration levels as the B-CPC.

For the ambient aerosol measurement, we recorded the consumption rate: the Sky-CPC was filled with 5 ml of DMSO, whereas the second Sky-CPC was filled with 20 ml butanol. We ran those measurements overnight. The B-CPC ran dry in the late morning as expected and was refilled, the D-CPC was still running and counting. For the first set of ambient measurements, the C1/C0 value of the D-CPC stayed at 1 and decreased slowly until it oscillated around 0.8. At a second approach we added a Water/DMSO mixture and the C1/C0 value decreased towards 0.6 slowly going up again to 0.8. Anyhow, the D-CPC number concentration was corrected with simultaneously logged data of the C1/C0 value, which was ranging around 0.8 in Figure 76.

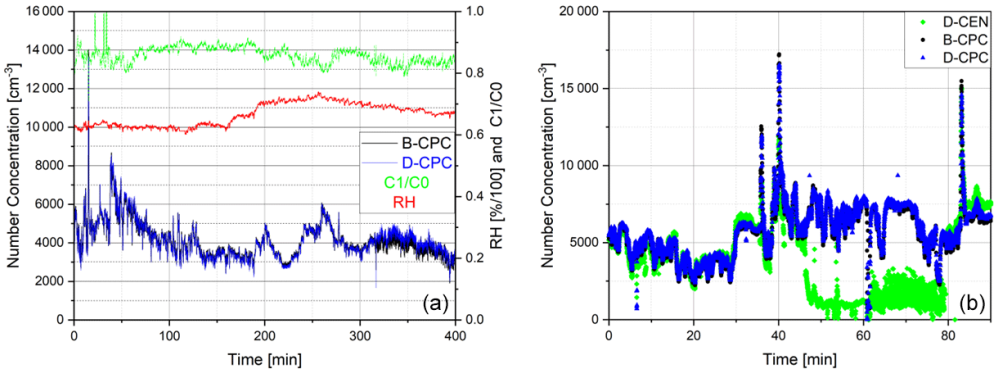

Figure 76. Ambient air as measured by the Sky CPC 5.411 operated with (a) Butanol (B-CPC) and DMSO (D-CPC) as well for the (b) CPC 3772-CEN operated with DMSO (D-CEN), that needed manual extraction of condensed water, which caused the number concentration to drop.

Figure 77 demonstrates that the measurements made using DMSO as the working fluid are not distinguishable from the measurements performed with butanol. The overall linearity for the new working fluid is shown in Figure 77. The slope of the linear correlation is 1.01 ±0.02 (r^2>0.99) for laboratory measurements as well as ambient for air measurements. For atmospheric measurements we used the B-CPC as well-known reference.

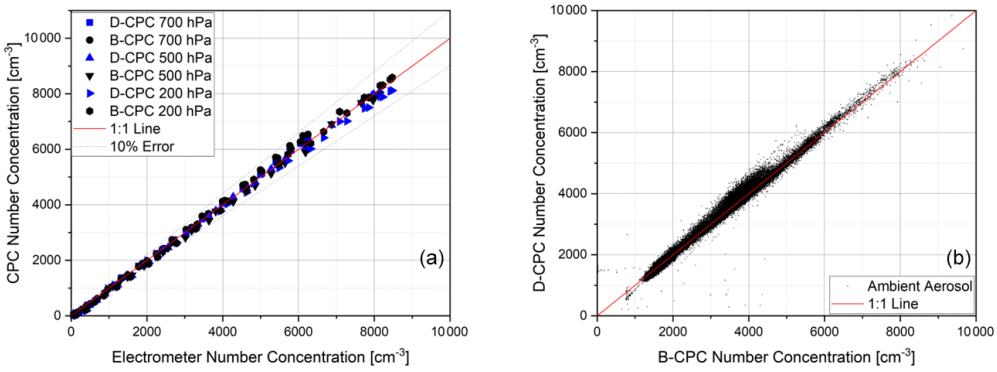

Figure 77. (a) Comparison of the concentration linearity of two Sky CPC 5.411 units to the electrometer reference at different pressure levels for ammonium sulphate and (b) comparison of correlation between B-CPC and D-CPC on ambient air.

9.1.4 Precautions for using DMSO as a Working Fluid

As already mentioned, the CPC 3772-CEN needed manual draining and refilling, and the Sky CPC 5.411 needed manual refilling as well. This is because rubber parts soak themselves with DMSO and swell, so they increase in size. With this behaviour, the o-rings expanded inside the valves for refilling and could no longer perform as intended, although it took several days to weeks before the valves stopped working. In order to address this issue, we exchanged those parts with

silicon o-rings. We operated the instruments for at least three months with the new working fluid and apart from the valves, no essential parts were affected since the device kept working. We repeated the process using DMSO as the operating fluid in a third Sky CPC 5.411 - this unit performed the same as the D-CPC in the first experiments, including agreeing well with the B-CPC and the swollen o-ring. As can be seen in Figure 78, the o-ring, as well as the stamp of the valve, increased by about 1 mm in seen diameter.

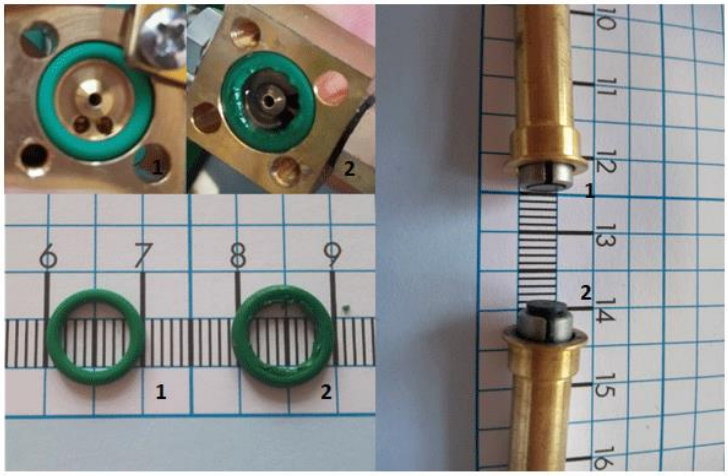

Figure 78. Picture of the CPC o-ring (left, top and bottom), and the stem of the liquid supply valve (right). (1) indicates operating fluid was butanol and (2) indicates operating fluid was DMSO.

With this increase in size, the sealing ring blocked the stamp and prevented the further flow of liquid to the wick. The continuous pump for draining in the Sky CPC 5.411 was still working as intended.

Cross-sensitivities between DMSO and several reactive atmospheric substances were not tested. We measured atmospheric aerosol for several weeks using instruments with DMSO as the operating fluid. We did not observe any significant shift in measured particle number concentrations between the reference B-CPC and the D-CPC. However, higher ozone or nitrogen oxides concentrations could trigger secondary organic aerosol activation within the instrument using DMSO.

In the CPC 3772-CEN, one of the critical orifices in the supply line of the working fluid started leaking and had to be replaced. It is not clear whether this issue can be attributed to the use of DSMO, as the instrument's maintenance state or operational errors could also have been causing factors.

DMSO can bring chemicals into the body by transporting dissolved chemicals through the skin and bacteria can convert DMSO into dimethyl sulphide, DMSO should not be disposed of into the sewer [138].

Another precaution that should be mentioned here is that DMSO should not be heated to temperatures above 150°C, since at that threshold it will lose its thermal stability. When

exceeding 150 °C, DMSO slowly starts to degrade into its by-products, which may have different characteristics.

From an instrument manufacturer's point of view, DMSO seems to be an interesting alternative working fluid to the commonly used butanol. Furthermore, at first glance, the modifications required for the correct and safe operation of a Grimm 5411 Sky-CPC appear to be relatively straightforward. However, as demonstrated in the experiments shown here, there is a need to adapt the CPC design to the specific properties of DMSO, specifically material durability. Also, the detailed condensation process so far remains an open question that needs to be addressed in future studies in order to adapt and optimize the particle detection in upcoming CPC models.

Equally important, the benefits of using DMSO as a substitute working fluid by far exceed the effort needed to prepare a CPC for its use, from a user or an instrument manufacturer's perspective. In TSI's most recent generation of butanol-CPCs, there are only few places where DMSO comes in contact with materials that it could degrade or swell quickly. In practice this means that those o-rings and gaskets that are by default made of polycarbonate (PC), polyvinylidene fluoride (PVDF) like Kynar®, or polyvinyl chloride (PVC), will need to be exchanged by their silicone equivalents. While this is not technically difficult, the exact replacement should be assessed and approved separately for every CPC generation and model by the manufacturer. Also, all modifications will need to be tested over much longer periods of time than the brief test period in this work as components such as the instrument optics might get impacted only after several weeks or months of exposure to DMSO. Of course, this would change with the introduction of a next-generation of alcohol-based CPCs that are designed for use with DMSO from the beginning.

9.1.5 DMSO as a suitable working fluid for low pressure applications

In this work, we have introduced dimethyl sulfoxide (DMSO) as an appropriate new substance to replace butanol as the working fluid in alcohol-based condensation particle counters (CPC). DMSO is an odourless, non-flammable and non-toxic substance. We would like to emphasize that DMSO overcomes the notable health and safety concerns that arise when using butanol in sensitive working environments, and this fact alone makes it a desirable candidate for operation of instruments on aircraft. Secondary benefits include the lower consumption when operating CPCs and its lower cost.

In our experiments we have demonstrated that the two different CPC models that we tested continued to operate as expected under several operational conditions. When changing the operation pressure from ambient level down to 200 hPa, which corresponds to the cruising level of passenger aircraft used within the IAGOS research infrastructure, the DMSO-operated CPC units displayed the same counting efficiencies as the butanol-operated CPCs. Even in very humid environments with a relative humidity of around 80% RH, the CPC operated with DMSO performed equivalent to a butanol CPC. It should be noted that at those high levels of humidity, the CPC 3772-CEN had to be drained frequently, while the Sky CPC 5.411 had to be corrected using its internally recorded C1/C0 value. Nevertheless, for all pressure levels and particle types

investigated, the DMSO-operated CPC performed essentially identical to the equivalent butanol-operated CPC. Further investigations with different temperatures for saturator and condenser are planned.

The introduction of DMSO as the working fluid requires no significant modifications of a CPC's hardware apart from minor changes to its liquid supply valve and a replacement of any gasket that comes in contact with the working fluid. Our initial results also indicate that the lower detection limit of the CPC might even be smaller with the new working fluid as a higher supersaturation can be achieved. This is due to the fact that DMSO has a far higher flaming point than butanol. This will be investigated further in cooperation with CPC manufacturers by using a custom-designed saturator block, heating and reservoir.

10 Conclusions and Outlook

The overarching objective of the work reported in this thesis was the improvement of the experimental foundations of aerosol measurement technology suitable for the conduction of regular aerosol in-situ observations on airborne platforms. Regular observation of aerosol properties on a fleet of passenger aircraft - as scheduled in the research infrastructure IAGOS – would help closing an important gap in the global climate observation system. The specific target of this studies was the optimisation and evaluation of an IAGOS instrument package for air quality related aerosol properties aligned with NO2 measurements, thus covering the key air quality indicators together with ozone measured regularly by IAGOS. The steps necessary for reaching this target included the evaluation of the individual instrument components for measuring aerosol number concentration and size distribution together aerosol light extinction as proxy for the mass concentration of airborne particulate matter.

The evaluation of all components was successfully accomplished for the full range of operation conditions. The instrumentation of the IAGOS air quality package (Package 2e) is shown to be stable and operational at aircraft cruising altitude conditions. With the two CAPS PMex, it is possible to deliver robust aerosol light extinction in-situ measurements at 450 and 630 nm wavelength. Taken this into account, it is possible to calculate the aerosol light extinction Ångström exponent. Together with the total number concentration counted by the water-based condensation particle counter (MAGIG-LP) and the optical size distribution of the accumulation mode down to 125 nm measured by the optical particle counter (POPS), it will become possible to validate satellite- borne aerosol products by means of IAGOS observations. Furthermore, the size information in the accumulation mode covers the range of particles, that are crucial for the formation of clouds[121, 139]. With the derived number concentration of all particles below 125 nm, it is possible to provide information of the number of particles, that have formed by gas-to-particle conversion. As an additional indicator for air quality, the NO_2 measurement as low as 0.1 ppbv gives a solid ground for global air quality assessment. As it was shown, those measurements can be used to observe the long-range transport of particulate matter and as a source identification.

Aerosol observations on board of passenger aircraft fill the gap between ground-based networks and satellite observations, since IAGOS operates in the upper free troposphere and is therefore located in the "middle" of these sensing networks and by providing vertical profiles. This is illustrated in Figure 79.

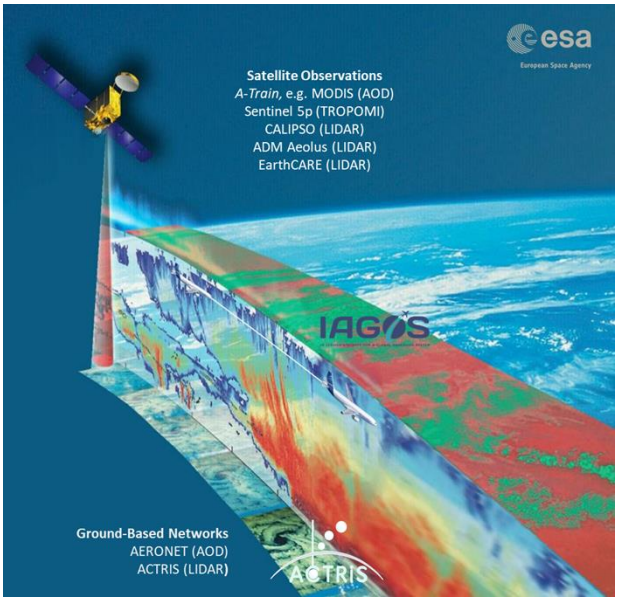

Figure 79. Schematic of the IAGOS satellites validation strategy.

The IAGOS data was already used to validate spacecraft carried active sensing instruments [140] or other forms of remote sensing techniques [141]. A new satellite is about to launch, which is called EarthCARE (earth.esa.int/eogateway/missions/earthcare). As it is promoted as the "largest and most complex earth explorer to date", it is a great opportunity for IAGOS datasets and products of the air quality package, to serve as the ground truth for the remote sensing techniques on this new satellite. In the same direction, the IAGOS air quality package will deliver essential data for the evaluation of the TROPOMI instrument on the SENTINEL-5 Precursor Mission of ESA. This instrument delivers data on the aerosol optical depth, i.e., the vertical integration of the aerosol light extinction coefficient, and the NO2 column load.

As these are important is the future applications for observation data by the IAGOS air quality package, a proof of concept was already performed. A prototype was operated on a research aircraft in August 2015, with the flight pattern shown in Figure 81. During the flight a vertical profile close to the observatory of the German Weather Service at Lindenberg, Germany was of special interest, since the area was highly polluted and it was possible to compare those measurements with Raman-LIDAR remote sensing measurements conducted at Lindenberg. The intercomparison of light extinction data from the air quality package and from the LIDAR showed excellent agreement for the total light extinction coefficients as well as for the closure performing calculations of the extinction coefficient using the measured aerosol size distribution applying Mie-theory calculations of the extinction coefficient. The offset of Mie calculations of light extinction coefficient, visible in Figure 80, compared to the LIDAR data as observed by Bundke

(2016) can easily be explained by the insufficient lower size detection limit of the instrument applied during this test with a minimum diameter of 250 nm. With the lower size limit of the new optical sizing instrument POPS, this gap may vanish since particles below 100 nm are hardly contributing to the light extinction coefficient.

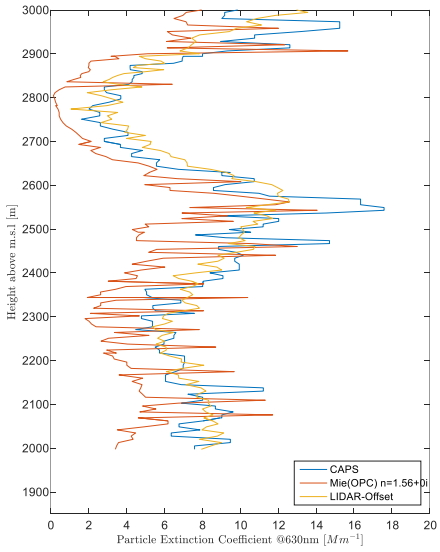

Figure 80. Height profiles of the lidar data are wavelength corrected to 630 nm using an Ångström coefficient of 1.6 measured by a sun photometer in Lindenberg [142].

If those measurement could be done frequently, those high-resolution in-situ measurements can be used to validate remote sensing networks such as Aeronet or the research infrastructure ACTRIS.

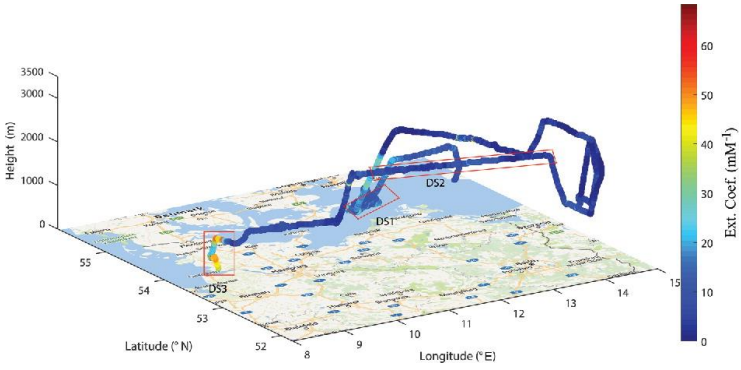

Figure 81. Geographical information of the flight route and measurement data of the CAPS aerosol light extinction coefficient [143].

Based on the results of this thesis, this concept can be further improved by implementing several changes. Those improvements include the addition of two CAPS tubes for measuring light extinction coefficients at multiple wavelenghts. A water-based condensation particle counter (MAGIC CPC [109]) was added as well, and as a last improvement, the original optical particle counter was exchanged with another model with a smaller laser wavelength to reduce the size limitations (POPS [71]).

The new working fluid gives possibilities to continue the operation of butanol-based condensation particle counters, without the need to replace already installed instruments namely at the IAGOS aerosol package. In addition, the use of DMSO in regular alcohol-based condensation particle counters can increase the range of application, since safety restrictions on flammable liquids are avoided. With this, alcohol-based condensation particle counters can be used in sensitive working areas.

The two IAGOS instrument packages suitable for aerosol measurements are essential for a global monitoring of aerosol properties. The importance of in situ aerosol optical properties measurements can be rated as very high, as the increase in global temperature is linked to solar brightening from aerosol reduction[144]. A recent report of the DWD (Deutsche Wetterdienst) accounted this effect to 2 W/m^2 per decade for germany[145].

In the near future, we will deal with the very first flight analysis. Furthermore, additional air quality instrument packages will be built and installed to cover more routes such as in the Canadian air space, since there are a boreal forest fires prominent. Continuous airborne measurements will give deeper insight into the behaviour and long-range atmospheric transport of those aerosols.

Another future project is planned for done with the new working fluid DMSO, as it has to be tested with extended temperature (Delta T >40 – 90 °C) settings for temperature differences between the saturator and condensator temperatures. We expect that this will lower the cut-off diameter below 3nm. The CEN-CPC is operated with specific temperature settings for butanol to fulfil standards and to have a cut-off efficiency around 13 nm. It is yet to be proven if this can be redone with DMSO. These kinds of experiments will also show, if the particle grow is initiated by the formation of droplets or by crystal formation. Another study will be conducted to show, if an expensive and cooled stage condensator is not needed for DMSO, if the saturator temperature is e.g. 80°C or higher.

The pending patent also states another promising chemical for condensation counters. Yet this substance is usually solid but has a relatively high vapour pressure of 5.15 mmHg, whereas butanol has a vapour pressure of around 6 mmHg at 23 °C. Initial tests were already done and passed first quality checks. Those quality checks include zero-counts with a particle filter installed in front of the CPC-inlet and a sudden increase to over 200.000 particles per cubic centimetre, when exposed to an aerosol source (lighter).

To summarise this thesis, it could be shown that the IAGOS air quality instrument is a reliable and accurate instrumentation that is suitable for use on passenger aircraft. It measures all parameters that are necessary to validate spacecraft carried active sensing instruments and operates as a measuring instrument for continuous environmental measurements. As a side product, several improvements and solutions were developed for condensation particle counters that deal with concerns of flammability of alcohol-based condensation particle counters or low-pressure applications of water-based condensation particle counters.

11 List of Tables and Figures

Tables

Table 1. Main Aerosol types in order by their magnitude of emission [17, 18]. 15
Table 2. Overview of aerosol types used 42
Table 3. List of instruments and used properties. 43
Table 4. Overview of the measured intensive optical properties of the pure aerosol types. 46
Table 5. Linear regression results of scattering, σ_{sp} , extinction, σ_{ep}, and absorption, σ_{ap}, for external mixtures of AQ and AS particles, given as slopes (m), Pearson R, and y-axis intercepts (b). 49
Table 6. Ensemble average ratios of σ_{ap} (TAP) / σ_{ap} (CAPS, NEPH) at 630 nm wavelength. N denotes the number of experiments used for the average. 50
Table 7. Ensemble average ratios of σ_{ap} (TAP) / σ_{ap} (CAPS, NEPH) at 450 nm wavelength. N denotes the number of experiments used for the average. 51
Table 8. Linear regression results of scattering, σ_{sp}, extinction, σ_{ep}, and absorption, σ_{ap}, coefficients for external mixtures of BC and AS particles, given as slopes (m), Pearson R, and y-axis intercepts (b). 53
Table 9. Linear regression results of scattering, σ_{sp}, extinction, σ_{ep}, and absorption, σ_{ap}, coefficients for external mixtures of SOOT and AS particles, given as slopes (m), Pearson R, and y-axis intercepts (b). 53
Table 10. Linear regression results of scattering, σ_{sp}, extinction, σ_{ep}, and absorption, σ_{ap}, coefficients for external mixtures of MB and AS particles, given as slopes (m), Pearson R, and y-axis intercepts (b). 54
Table 11. Ensemble instrument-to-instrument measurement ratio averages and standard deviations for different instrument combinations used to derive SSA values at 630 nm wavelength using $SSA(NEPH, CAPS)$ as reference. 56
Table 12. Ensemble instrument-to-instrument measurement ratio averages and standard deviations for different instrument combinations used to derive SSA values at 450 nm wavelength using $SSA(NEPH, CAPS)$ as reference. 57
Table 13. Ensemble averages and standard deviations for the instrument-to-instrument ratios of the Ångström exponents (EAE, SAE, AAE) derived from multiple instruments relative to those derived from single instruments as reference. 63
Table 14. Approximation coefficients [108]. 70
Table 15. Coefficients of the exponential function of the Counting Efficiency Curves for the Sky-CPC 5.411 (SKY-CPC) and the MAGIC 210-LP CPC and for different line pressure values and ammonium sulphate. 82
Table 16. Coefficients of the exponential function of the Counting Efficiency Curves for the Sky-CPC 5.411 (SKY-CPC) and the MAGIC 210-LP CPC for different line pressure values and fresh combustion soot. 83
Table 17. Coefficients of the exponential function of the counting efficiency curves and the D90 cut-off diameter (at either 200 or 250 hPa) for different particle types for the Sky CPC 5.411 operated with Butanol (B-CPC) and DMSO (D-CPC); DMSO-Water mixture (DW-CPC) and CPC 3772-CEN operated with DMSO (D-CEN). 101

Figures

Figure 1. Effective radiative forcing changes from 1750 to 2019 (a) and global mean surface air temperature (GSAT) changes (b) from different climate variables according to CMIP6 model [3, 5]. 12
Figure 2. Overview of the main categories of air quality and their interaction with climate [10]...13
Figure 3. IAGOS Flight routes since 2011; source: iagos.org. 14
Figure 4. Size distributions of naturally occurring aerosols with their relative volumetric number density [19]. 16
Figure 5. Illustration of the size distribution of a single source aerosol. With normal scale (left) and logarithmic scale (right) forming a gaussian distribution. 18
Figure 6. Calculated Single Scattering Albedo of a mono-modal aerosol determined at two different wavelengths. using a complex refractive index of 1.75+i0.63. 22
Figure 7. Illustration of the wavelength dependency of the aerosol Rayleigh scattering coefficients with different Ångström exponents. 23
Figure 8. Schematic of the basic set-up for the alcohol-based condensation particle counter [45]. 24
Figure 9 . Illustration of the functional part of the Differential Mobility Analyzer [51]. 27
Figure 10. The basic principle of optical particle detection and sizing [52]. 28
Figure 11. Principle of optical particle spectrometers superimposed with a typical scattering profile of an aerosol. [54] 28
Figure 12. Calculated scattering intensity curves for different particle types (PSL; polysterene latex, AS; ammonium sulphate and DHES diethylhexylsebecat) [55] 29
Figure 13. Schematic of signal generation of the cavity attenuated phase shift monitor [57]. 30
Figure 14. Illustration of the primary mechanism to derive the light extinction coefficient [58]. The same mechanism applies for the use of nitrogen dioxide as specimen instead of particles. 30
Figure 15. Schematic of an integrating nephelometer (© TSI) 31
Figure 16. Setup for a Particle Soot Absorption Photometer (PSAP) which is also true for the TAP. Particles are deposited on the filter and a second particle free spot is set as a reference spot [62]. 32
Figure 17. First concept of the air quality package [70]. 33
Figure 18. List of instruments and corresponding cooperation partners. 34
Figure 19. Detailed flow chart of P2e for aircraft operation [73]. 35
Figure 20. Picture of the full assembled instrument package. With (1) shielded Main Board and electronics, (2) CAPS boards, (3) Ventilation between the MAGIC CPC and POPS and (4) the main ventilation. 36
Figure 21. Heat development inside the Instrument Package 2e at different locations. 37
Figure 22. Calibration of the CAPS instruments with a high span gas. 38
Figure 23. Intercomparison of aerosol light extinction coefficient measured by the CAPS PMex and Extinction coefficients derived by Mie theory using Size distribution measurements of the OPC. (Closure study) 39
Figure 24. Experimental setup for the measurements. Flame soot measurements were done with a combustion flame source replacing #2 Nebuliser. 41
Figure 25. Measured size distributions by SMPS for the pure aerosol types used, set to an assumed total concentration. 45
Figure 26. Scatter plots of the extinction coefficients for different AQ-AS external mixtures at 630 nm (left) and 450 nm wavelengths (right). The y-axes show the extinction coefficients derived by combining TAP absorption and NEPH scattering coefficients versus the CAPS PM_{SSA} monitor direct extinction coefficient measurements. The colour code represents the SSA of the

analysed mixed aerosol measured at 630 nm wavelength. In addition, an error band of ±10% was added to the 1:1 line. 47
Figure 27. Comparisons of measured light scattering coefficients at 450 nm and 630 nm wavelengths for mixtures of AQ and AS aerosols. The y-axes show the CAPS PM_{SSA} (integrating sphere) or the Differential Method (CAPS extinction minus TAP absorption) scattering versus NEPH scattering measurements at 450 nm and 630 nm wavelengths. The colour code represents the SSA value of the measured aerosol mixture. An error band of ±10% was applied to the 1:1 line. Error bars shown represent instrument precisions (1 σ). 48
Figure 28. Scatter plots of measured 450 nm and 630 nm wavelength absorption coefficients of external mixtures of AQ and AS for different instrument combinations. The colour code represents the SSA value of the respective data point. An error band of ±20% was applied to the 1:1 line, which is required for monitoring systems [102] for light absorption measurements. Error bars shown represent propagated instrument precisions (1 σ). 49
Figure 29. Variance of the measured absorption coefficients [σ_{ap} (CAPS, CAPS)) / σ_{ap} (TAP)] for Differential Method calculations relative to TAP measurements for AQ and AS external mixtures. The ratios are plotted against the aerosol measured SSA values [SSA(CAPS, CAPS)]. The red line represents the calculated relative errors using Gaussian error propagation of the uncertainties of the DM Method with 1 as 100%.. 52
Figure 30. Scatter plots of derived SSA values from various combinations of measurements at 630 nm wavelength obtained for AQ/AS mixtures (y-axis) versus SSA(NEPH, CAPS) as the reference on the x-axis. The colour code indicates σ_{ap}(TAP) values shown in Mm^{-1}. 55
Figure 31. Scatter plots of Differential Method derived SSA values for different instrument combinations at 450 nm wavelength using AQ/AS mixtures versus SSA(NEPH, CAPS). The colour code indicates σ_{ap}(TAP) values shown in Mm^{-1}. 57
Figure 32. Scatter plot of EAE(NEPH, TAP) measurements compared to EAE(CAPS) measurements for AQ/AS mixtures. An error band of 10% is shown. 59
Figure 33. The extinction Ångström exponent EAE(NEPH, TAP) / EAE(CAPS) ratios as a function of 630nm wavelength SSA(NEPH, CAPS) values for AQ/AS mixtures. The 630 nm wavelength light absorption coefficient, σ_{ep}(CAPS), is used as the colour code. 59
Figure 34. Scatter plot of SAE (CAPS, TAP) measurements compared to SAE(NEPH) measurements for AQ/AS mixtures. An error band of 10% is shown. 60
Figure 35. The scattering Ångström exponent ratio, SAE(CAPS, TAP) / SAE(NEPH), as a function of 630nm wavelength SSA(NEPH, CAPS) values for AQ/AS mixtures. The 630 nm wavelength light absorption coefficient, σ_{ap}(TAP), is used as the colour code. 60
Figure 36. Scatter plot of AAE(CAPS, NEPH) measurements compared to AAE(TAP) measurements for pure AQ and AQ/AS external mixtures. Measured precision error bars are shown for individual AQ/AS externally mixed measurements. 62
Figure 37. The absorbing Ångström exponent ratio, AAE(CAPS, NEPH) / AAE(TAP), as a function of 630 nm wavelength SSA(NEPH, CAPS) values for AQ/AS mixtures. The 630 nm wavelength light absorption coefficient, σ_{ap}(TAP), is used as the colour code. Measured precision error bars are shown for individual measurements. 62
Figure 38. Allan Deviation calculations for fresh cleaned mirrors (LOSS=500, green makers) and dusted mirrors (LOSS=1600, red markers) for the CAPS instrument.....65
Figure 39. Allan Variance for CAPS measurements obtained by Massoli [57]. 65
Figure 40. CAPS light extinction measurement compared with Mie Theory as a function of the particle number concentrations separated for 50, 80, 100 nm particles selected by the DMA. .66
Figure 41. Intercomparison of between two CLD instruments and the CAPS. 67
Figure 42. Time Series of the NO_2 intercomparison starting at 10am from the 16th of October 2019. 68

Figure 43. Flight Simulation Test Stand: Flow schematic of the laboratory set-up for the low-pressure characterisation with two aerosol sources. The inline pressure is PID controlled balancing the volumetric in- and out flow via mass flow controllers (MFC) as control elements; the aerosol size classification is ensured with a differential mobility analyser (DMA) and the faraday cup electrometer (FCE) functions as a reference instrument for particle counting). 69
Figure 44. The CMD with the relationship of the concentration of the nebulised salt solution. .69
Figure 45. Multi charge correction function adapted from Bundke et al., (2015)[50].....72
Figure 46. Principle of Operation of the MAGIC-CPC [109]. 73
Figure 47. Flow schematic of the laboratory set-up for the low-pressure characterisation with two aerosol sources. The inline pressure is controlled via mass flow controllers (MFC); the aerosol size classification is ensured with a differential mobility analyser (DMA) and the faraday cup electrometer (FCE) functions as a reference instrument for particle counting). Adapted from Figure 43......74
Figure 48. Ideal signal from one particle passing through the optics detector [112].....76
Figure 49. Effect of imperfections in optics and electronics on the baseline voltage.....77
Figure 50. Detector threshold is increased to compensate for inability of the electronics to completely cancel out the baseline signal at lowest pressure. 77
Figure 51. Counting Efficiency response for different initial laser power settings (Lset) and pressure levels for 100 nm particles. 78
Figure 52. Particle size distributions were measured by Electrometer and sized by DMA for ammonium sulphate and fresh combustion soot. For this work, the particle mobility sizes were measured to 138 nm, so the size resolution at smaller sizes is suitable for the cut-off characterisation. The full particle size distributions are available [42]. 78
Figure 53. Compilation of the efficiency ratio curves of the Sky-CPC 5.411 (SKY-CPC) (left) and the MAGIC 210-LP CPC (right) to the FCE reference - at different operation pressures as a function of the particle size using ammonium sulphate particles. The variance of the measurement is indicated by vertical bars......79
Figure 54. Comparison of the counting linearity between both CPC types and the Electrometer at different pressure levels for nebulised ammonium sulphate. 80
Figure 55. Comparison of the efficiency ratio curves of the Sky-CPC 5.411 (SKY-CPC) (left) and the MAGIC 210-LP CPC (right) to the electrometer reference at different operating pressures as a function of the particle size using fresh combustion soot. The variance of the measurement is indicated by vertical bars. 81
Figure 56. Comparison of the counting linearity between CPC and Electrometer at different pressure levels for fresh combustion soot......81
Figure 57. Particle Line Loss calculations for 1000 hPa (Ground) and 220 hPa (Air).....85
Figure 58. Fraction of the particles that are transmitted through the inlet line for two different pressure levels at ground-level (P=1013 hPa and cruising altitude P=200 hPa considering diffusion losses only. 86
Figure 59. Simplified overview of the core components of the POPS. 87
Figure 60. Top view of the POPS components.....87
Figure 61. Illustration of raw data of a single particle (left) and the baseline shift at different pressure levels (right).....88
Figure 62. Measurements of different PSL diameters with the POPS channel response.....88
Figure 63. Computed Mie curve with measured raw data. 89
Figure 64. Matched Scattering intensity with 16 channel boundarys. 89
Figure 65. POPS Counting Ratio against the MAGIC-CPC.....90
Figure 66. Data output of OPC for monodisperse aerosols measured by Sang-Nourpour (2019) [117].....90
Figure 67. Schematic of the package 2c [50].....91

Figure 68. Schematic of the chemical reaction of DMS and DMSO in the atmosphere and aqueous mediums [123]. 92
Figure 69. Saturation ratio of three working fluids as a function of the droplet diameter for a sodium chloride particle with an initial diameter of 13 nm [23]. For DMSO, a surface tension of 0.043 N/m, a molecular weight of 0.078 kg/mole and the liquid density of 1100 kg/m^3 is used CRC Handbook, [134]. 94
Figure 70. The theoretical saturation vapour pressure of butanol, water and DMSO as calculated by the Antoine equations [47, 136]. 95
Figure 71. Particle size distributions of ammonium sulphate (AS), sodium chloride (NaCl) and fresh combustion soot as measured by the combination of DMA and electrometer. 96
Figure 72. Illustration of the pulse height of DMSO-Droplets of different sizes with corresponding detector threshold levels. 97
Figure 73. Counting efficiency curves of the Sky CPC 5.411 operated with butanol (B-CPC) and DMSO (D-CPC) at different operation pressures using ammonium sulphate particles. 98
Figure 74. Counting efficiency curves for sodium chloride particles with respect to the electrometer reference instrument and corrected for multiple charge of the Sky CPC 5.411 (a) as well as for the CPC 3772-CEN (b), both operated with butanol (B-CPC) and DMSO (D-CPC; D-CEN) at different operating pressures. 99
Figure 75. Counting efficiency curves with respect to the electrometer reference instrument and corrected for multiple charges at different operating pressures using fresh combustion soot particles for (a) Sky CPC 5.411 operated with butanol (B-CPC) and mixture of DMSO and water (DW-CPC) and (b) Sky CPC 5.411 operated with butanol (B-CPC) and the CPC 3772-CEN operated with DMSO (D-CEN). 100
Figure 76. Ambient air as measured by the Sky CPC 5.411 operated with (a) Butanol (B-CPC) and DMSO (D-CPC) as well for the (b) CPC 3772-CEN operated with DMSO (D-CEN), that needed manual extraction of condensed water, which caused the number concentration to drop. 102
Figure 77. (a) Comparison of the concentration linearity of two Sky CPC 5.411 units to the electrometer reference at different pressure levels for ammonium sulphate and (b) comparison of correlation between B-CPC and D-CPC on ambient air. 102
Figure 78. Picture of the CPC o-ring (left, top and bottom), and the stem of the liquid supply valve (right). (1) indicates operating fluid was butanol and (2) indicates operating fluid was DMSO. 103
Figure 79. Schematic of the IAGOS satellites validation strategy. 106
Figure 80. Height profiles of the lidar data are wavelength corrected to 630 nm using an Ångström coefficient of 1.6 measured by a sun photometer in Lindenberg [142]. 107
Figure 81. Geographical information of the flight route and measurement data of the CAPS aerosol light extinction coefficient [143] 107

12 References

1. Li, Y.; Qian, H.; Hang, J.; Chen, X.; Hong, L.; Liang, P.; Li, J.; Xiao, S.; Wei, J.; Liu, L.; Kang, M., Evidence for probable aerosol transmission of SARS-CoV-2 in a poorly ventilated restaurant. *medRxiv* 2020, 2020.04.16.20067728.
2. Gesellschaft Für Aerosolforschung, E. V., Position paper of the Gesellschaft für Aerosolforschung on understanding the role of aerosol particles in SARS-CoV-2 infection. 2020.
3. Szopa, S., V. Naik, B. Adhikary, P. Artaxo, T. Berntsen, W.D. Collins, S. Fuzzi, L. Gallardo, A. Kiendler-Scharr, Z. Klimont, H. Liao, N. Unger, and P. Zanis, Short-Lived Climate Forcers. In Climate Change 2021: The Physical Science Basis. Contribution of Working Group I to the Sixth Assessment Report of the Intergovernmental Panel on Climate Change. Masson-Delmotte, V., P. Zhai, A. Pirani, S.L. Connors, C. Péan, S. Berger, N. Caud, Y. Chen, L. Goldfarb, M.I. Gomis, M. Huang, K. Leitzell, E. Lonnoy, J.B.R. Matthews, T.K. Maycock, T. Waterfield, O. Yelekçi, R. Yu, and B. Zhou, Ed. Cambridge University Press, 2021; pp 817–922.
4. Charlson, R. J.; Heintzenberg, J., Report of the Dahlem Workshop on Aerosol Forcing of Climate, Berlin 1994, April 24-29 - Introduction. *Aerosol Forcing of Climate* 1995, *17*, 1-10.
5. Thornhill, G. D.; Collins, W. J.; Kramer, R. J.; Olivié, D.; Skeie, R. B.; O'Connor, F. M.; Abraham, N. L.; Checa-Garcia, R.; Bauer, S. E.; Deushi, M.; Emmons, L. K.; Forster, P. M.; Horowitz, L. W.; Johnson, B.; Keeble, J.; Lamarque, J. F.; Michou, M.; Mills, M. J.; Mulcahy, J. P.; Myhre, G.; Nabat, P.; Naik, V.; Oshima, N.; Schulz, M.; Smith, C. J.; Takemura, T.; Tilmes, S.; Wu, T.; Zeng, G.; Zhang, J., Effective radiative forcing from emissions of reactive gases and aerosols – a multi-model comparison. *Atmos. Chem. Phys.* 2021, *21* (2), 853-874.
6. Ruckstuhl, C.; Philipona, R.; Behrens, K.; Collaud Coen, M.; Dürr, B.; Heimo, A.; Mätzler, C.; Nyeki, S.; Ohmura, A.; Vuilleumier, L.; Weller, M.; Wehrli, C.; Zelenka, A., Aerosol and cloud effects on solar brightening and the recent rapid warming. *Geophysical Research Letters* 2008, *35* (12).
7. Quaas, J.; Jia, H.; Smith, C.; Albright, A. L.; Aas, W.; Bellouin, N.; Boucher, O.; Doutriaux-Boucher, M.; Forster, P. M.; Grosvenor, D.; Jenkins, S.; Klimont, Z.; Loeb, N. G.; Ma, X.; Naik, V.; Paulot, F.; Stier, P.; Wild, M.; Myhre, G.; Schulz, M., Robust evidence for reversal of the trend in aerosol effective climate forcing. *Atmos. Chem. Phys.* 2022, *22* (18), 12221-12239.
8. Cheng, Y. S., Mechanisms of Pharmaceutical Aerosol Deposition in the Respiratory Tract. *AAPS PharmSciTech* 2014, *15* (3), 630-640.
9. OECD, *OECD Environmental Outlook to 2050*. 2012.
10. von Schneidemesser, E.; Monks, P. S.; Allan, J. D.; Bruhwiler, L.; Forster, P.; Fowler, D.; Lauer, A.; Morgan, W. T.; Paasonen, P.; Righi, M.; Sindelarova, K.; Sutton, M. A., Chemistry and the Linkages between Air Quality and Climate Change. *Chemical Reviews* 2015, *115* (10), 3856-3897.
11. Petzold, A.; Ogren, J. A.; Fiebig, M.; Laj, P.; Li, S. M.; Baltensperger, U.; Holzer-Popp, T.; Kinne, S.; Pappalardo, G.; Sugimoto, N.; Wehrli, C.; Wiedensohler, A.; Zhang, X. Y., Recommendations for reporting "black carbon" measurements. *Atmos. Chem. Phys.* 2013, *13* (16), 8365-8379.
12. Petzold, A.; Bundke, U.; Hienola, A.; Laj, P.; Lund Myhre, C.; Vermeulen, A.; Adamaki, A.; Kutsch, W.; Thouret, V.; Boulanger, D.; Fiebig, M.; Stocker, M.; Zhao, Z.; Asmi, A., Opinion: New directions in atmospheric research offered by research infrastructures combined with open and data-intensive science. *EGUsphere* 2023, *2023*, 1-39.
13. Petzold, A.; Thouret, V.; Gerbig, C.; Zahn, A.; Brenninkmeijer, C. A. M.; Gallagher, M.; Hermann, M.; Pontaud, M.; Ziereis, H.; Boulanger, D.; Marshall, J.; Nedelec, P.; Smit, H. G. J.; Friess, U.; Flaud, J. M.; Wahner, A.; Cammas, J. P.; Volz-Thomas, A.; Team, I., Global-scale

atmosphere monitoring by in-service aircraft - current achievements and future prospects of the European Research Infrastructure IAGOS. *Tellus Series B-Chemical and Physical Meteorology* 2015, *67*, 24.
14. Jaenicke, R., Atmospheric aerosols and global climate. *Journal of Aerosol Science* 1980, *11* (5), 577-588.
15. Fiebig, M. *Das troposphärische Aerosol in mittleren Breiten - Mikrophysik, Optik und Klimaantrieb am Beispiel der Feldstudie LACE 98*; 2001; p 259.
16. Ramanathan, V.; Crutzen, P. J.; Kiehl, J. T.; Rosenfeld, D., Aerosols, climate, and the hydrological cycle. *Science* 2001, *294* (5549), 2119-24.
17. Kokhanovsky, A. A., Aerosol Optics. In *Atmospheric Aerosols*, 2017; pp 223-246.
18. Jaenicke, R. *9.6 Properties of aerosols in general: Datasheet from Landolt-Börnstein - Group V Geophysics · Volume 4B: "Physical and Chemical Properties of the Air" in SpringerMaterials doi.org/10.1007/10333390_77)*, Springer-Verlag Berlin Heidelberg.
19. Wilson, W.; Claiborn, C.; Hemming, B., Air quality criteria for particulate matter (Final Report, Oct 2004) USEPA U.S. Environmental Protection Agency, Washington, DC, EPA 600/P-99/002aF-bF 2004. 2004.
20. Mäkelä, J. M.; Aalto, P.; Jokinen, V.; Pohja, T.; Nissinen, A.; Palmroth, S.; Markkanen, T.; Seitsonen, K.; Lihavainen, H.; Kulmala, M., Observations of ultrafine aerosol particle formation and growth in boreal forest. *Geophysical Research Letters* 1997, *24* (10), 1219-1222.
21. Whitby, K. T., The physical characteristics of sulfur aerosols. *Atmospheric Environment (1967)* 1978, *12* (1), 135-159.
22. Wilson, W. E.; Spider, L. L.; Ellestad, T. G.; Lamothe, P. J.; Dzubay, T. G.; Stevens, R. K.; Macias, E. S.; Fletcher, R. A.; Husar, J. D.; Husar, R. B.; Whitby, K. T.; Kittelson, D. B.; Cantrell, B. K., General Motors Sulfate Dispersion Experiment: Summary of EPA Measurements. *Journal of the Air Pollution Control Association* 1977, *27* (1), 46-51.
23. Hinds, W. C., *Aerosol Technology: Properties, Behavior, and Measurement of Airborne Particles*. Wiley: 1999.
24. Baron, P. A.; Willeke, K., Aerosol measurement: principles, techniques, and applications. 2001.
25. Charlson, R. J.; Schwartz, S. E.; Hales, J. M.; Cess, R. D.; Coakley, J. A.; Hansen, J. E.; Hofmann, D. J., Climate forcing by anthropogenic aerosols. *Science* 1992, *255* (5043), 423-430.
26. Mie, G., Beiträge zur Optik trüber Medien, speziell kollodialer Metallösungen. *Annalen der Physik* 1908, 377-445.
27. Bohren, C. F.; Huffman, D. R., *Absorption and scattering of light by small particles*. 1983.
28. *Model 3563 Integrating Nephelometer Operation and Service Manuel*; 2005.
29. Ångström, A., On the Atmospheric Transmission of Sun Radiation and on Dust in the Air. *Geografiska Annaler* 1929, *11*, 156-166.
30. Foster, K.; Pokhrel, R.; Burkhart, M.; Murphy, S., A novel approach to calibrating a photoacoustic absorption spectrometer using polydisperse absorbing aerosol. *Atmos. Meas. Tech.* 2019, *12* (6), 3351-3363.
31. Russell, P. B.; Bergstrom, R. W.; Shinozuka, Y.; Clarke, A. D.; DeCarlo, P. F.; Jimenez, J. L.; Livingston, J. M.; Redemann, J.; Dubovik, O.; Strawa, A., Absorption Angstrom Exponent in AERONET and related data as an indicator of aerosol composition. *Atmos. Chem. Phys.* 2010, *10* (3), 1155-1169.
32. Petzold, A.; Rasp, K.; Weinzierl, B.; Esselborn, M.; Hamburger, T.; DöRnbrack, A.; Kandler, K.; SchuüTz, L.; Knippertz, P.; Fiebig, M.; Virkkula, A., Saharan dust absorption and refractive index from aircraft-based observations during SAMUM 2006. *Tellus B: Chemical and Physical Meteorology* 2009, *61* (1), 118-130.
33. Kim, J.; Bauer, H.; Dobovičnik, T.; Hitzenberger, R.; Lottin, D.; Ferry, D.; Petzold, A., Assessing Optical Properties and Refractive Index of Combustion Aerosol Particles Through

Combined Experimental and Modeling Studies. *Aerosol Science and Technology* 2015, *49* (5), 340-350.
34. Formenti, P.; Schütz, L.; Balkanski, Y.; Desboeufs, K.; Ebert, M.; Kandler, K.; Petzold, A.; Scheuvens, D.; Weinbruch, S.; Zhang, D., Recent progress in understanding physical and chemical properties of African and Asian mineral dust. *Atmos. Chem. Phys.* 2011, *11* (16), 8231-8256.
35. Kokhanovsky, A., *Aerosol Optics: Light Absorption and Scattering by Particles in the Atmosphere*. 2008.
36. Berry, M. V.; Percival, I. C., Optics of Fractal Clusters Such as Smoke. *Optica Acta: International Journal of Optics* 1986, *33* (5), 577-591.
37. Kirchstetter, T. W.; Thatcher, T. L., Contribution of organic carbon to wood smoke particulate matter absorption of solar radiation. *Atmos. Chem. Phys.* 2012, *12* (14), 6067-6072.
38. Xu, L.; Suresh, S.; Guo, H.; Weber, R. J.; Ng, N. L., Aerosol characterization over the southeastern United States using high-resolution aerosol mass spectrometry: spatial and seasonal variation of aerosol composition and sources with a focus on organic nitrates. *Atmos. Chem. Phys.* 2015, *15* (13), 7307-7336.
39. Veselovskii, I.; Goloub, P.; Podvin, T.; Bovchaliuk, V.; Derimian, Y.; Augustin, P.; Fourmentin, M.; Tanre, D.; Korenskiy, M.; Whiteman, D. N.; Diallo, A.; Ndiaye, T.; Kolgotin, A.; Dubovik, O., Retrieval of optical and physical properties of African dust from multiwavelength Raman lidar measurements during the SHADOW campaign in Senegal. *Atmos. Chem. Phys.* 2016, *16* (11), 7013-7028.
40. Kaskaoutis, D. G.; Kambezidis, H. D.; Hatzianastassiou, N.; Kosmopoulos, P. G.; Badarinath, K. V. S., Aerosol climatology: on the discrimination of aerosol types over four AERONET sites. *Atmos. Chem. Phys. Discuss.* 2007, *2007*, 6357-6411.
41. Penner, J.; Andreae, M.; Annegarn, H.; Barrie, L.; Feichter, J.; Hegg, D.; Achuthan, J.; Leaitch, R.; Murphy, D.; Nganga, J.; Pitari, G., Aerosols, their Direct and Indirect Effects. *Climate Change 2001: The Scientific Basis. Contribution of Working Group I to the Third Assessment Report of the Intergovernmental Panel on Climate Change, 289-348 (2001)* 2001.
42. Weber, P.; Petzold, A.; Bischof, O. F.; Fischer, B.; Berg, M.; Freedman, A.; Onasch, T. B.; Bundke, U., Relative errors in derived multi-wavelength intensive aerosol optical properties using cavity attenuated phase shift single-scattering albedo monitors, a nephelometer, and tricolour absorption photometer measurements. *Atmos. Meas. Tech.* 2022, *15* (11), 3279-3296.
43. *Manuel, Model 3076 Constant Output Atomizer*. 2007.
44. Mobile Condensation Particle Counters. Gerätehandbuch, Model No 5.411: 2007.
45. Giechaskiel, B.; Maricq, M.; Ntziachristos, L.; Dardiotis, C.; Wang, X.; Axmann, H.; Bergmann, A.; Schindler, W., Review of motor vehicle particulate emissions sampling and measurement: From smoke and filter mass to particle number. *Journal of Aerosol Science* 2014, *67*, 48-86.
46. Thomson, W., LX. On the equilibrium of vapour at a curved surface of liquid. *The London, Edinburgh, and Dublin Philosophical Magazine and Journal of Science* 1871, *42* (282), 448-452.
47. Antoine, C., *Comptes Rendus* 1888, *107*, 681.
48. Weber, P.; Bischof, O. F.; Fischer, B.; Berg, M.; Schmitt, J.; Steiner, G.; Keck, L.; Petzold, A.; Bundke, U., A new working fluid for condensation particle counters for use in sensitive working environments. *Aerosol Research* 2023, *1* (1), 1-12.
49. Reischl, G. P.; Mäkelä, J. M.; Necid, J., Performance of Vienna Type Differential Mobility Analyzer at 1.2–20 Nanometer. *Aerosol Science and Technology* 1997, *27* (6), 651-672.
50. Bundke, U., The IAGOS-Core aerosol package: instrument design operation and performance for continuous measurement aboard in-service aircraft. Tellus B, 67,28339: 2015.
51. Intra, A. P. D. P.; Tippayawong, N., An overview of differential mobility analyzers for size classification of nanometer-sized aerosol particles. *Songklanakarin Journal of Science and Technology* 2008, *30*.

52. Konradin, W.; Andreas, V.; Christian, F.; Günther van, H.; Tobias, P. In *Airborne measurements of the Eyjafjallajökull volcanic ash plume over northwestern Germany with a light aircraft and an optical particle counter: first results*, Proc.SPIE, 2010; p 78320P.
53. *Portable Laser Aerosolspectrometer and Dust Monitor, Manuel, Model No 1.108/1.109*. 2010.
54. Czitrovszky, A., 22 - Environmental applications of solid-state lasers. In *Handbook of Solid-State Lasers*, Denker, B.; Shklovsky, E., Eds. Woodhead Publishing: 2013; pp 616-646.
55. Bundke, U.; Berg, M.; Houben, N.; Ibrahim, A.; Fiebig, M.; Tettich, F.; Klaus, C.; Franke, H.; Petzold, A., The IAGOS-CORE aerosol package: instrument design, operation and performance for continuous measurement aboard in-service aircraft. *Tellus B* 2015, *67*, 286-302.
56. Onasch, T. B.; Massoli, P.; Kebabian, P. L.; Hills, F. B.; Bacon, F. W.; Freedman, A., Single Scattering Albedo Monitor for Airborne Particulates. *Aerosol Science and Technology* 2015, *49* (4), 267-279.
57. Massoli, P.; Kebabian, P. L.; Onasch, T. B.; Hills, F. B.; Freedman, A., Aerosol Light Extinction Measurements by Cavity Attenuated Phase Shift (CAPS) Spectroscopy: Laboratory Validation and Field Deployment of a Compact Aerosol Particle Extinction Monitor. *Aerosol Science and Technology* 2010, *44* (6), 428-435.
58. Kebabian, P. L.; Robinson, W. A.; Freedman, A., Optical extinction monitor using cw cavity enhanced detection. *Review of Scientific Instruments* 2007, *78* (6), 063102.
59. Petzold, A.; Onasch, T.; Kebabian, P.; Freedman, A., Intercomparison of a Cavity Attenuated Phase Shift-based extinction monitor (CAPS PMex) with an integrating nephelometer and a filter-based absorption monitor. *Atmospheric Measurement Techniques* 2013, *6* (5), 1141-1151.
60. Modini, R. L.; Corbin, J. C.; Brem, B. T.; Irwin, M.; Bertò, M.; Pileci, R. E.; Fetfatzis, P.; Eleftheriadis, K.; Henzing, B.; Moerman, M. M.; Liu, F.; Müller, T.; Gysel-Beer, M., Detailed characterization of the CAPS single-scattering albedo monitor (CAPS PMssa) as a field-deployable instrument for measuring aerosol light absorption with the extinction-minus-scattering method. *Atmos. Meas. Tech.* 2021, *14* (2), 819-851.
61. Anderson, T. L.; Covert, D. S.; Marshall, S. F.; Laucks, M. L.; Charlson, R. J.; Waggoner, A. P.; Ogren, J. A.; Caldow, R.; Holm, R. L.; Quant, F. R.; Sem, G. J.; Wiedensohler, A.; Ahlquist, N. A.; Bates, T. S., Performance characteristics of a high-sensitivity, three-wavelength, total scatter/backscatter nephelometer. *Journal of Atmospheric and Oceanic Technology* 1996, *13* (5), 967-986.
62. Bond, T. C.; Anderson, T. L.; Campbell, D., Calibration and intercomparison of filter-based measurements of visible light absorption by aerosols. *Aerosol Science and Technology* 1999, *30* (6), 582-600.
63. Sheridan, P. J.; Arnott, W. P.; Ogren, J. A.; Andrews, E.; Atkinson, D. B.; Covert, D. S.; Moosmüller, H.; Petzold, A.; Schmid, B.; Strawa, A. W.; Varma, R.; Virkkula, A., The Reno Aerosol Optics Study: An Evaluation of Aerosol Absorption Measurement Methods. *Aerosol Science and Technology* 2005, *39* (1), 1-16.
64. Drummond, J. W.; Volz, A.; Ehhalt, D. H., An optimized chemiluminescence detector for tropospheric NO measurements. *Journal of Atmospheric Chemistry* 1985, *2* (3), 287-306.
65. Fontijn, A.; Sabadell, A. J.; Ronco, R. J., Homogeneous chemiluminescent measurement of nitric oxide with ozone. Implications for continuous selective monitoring of gaseous air pollutants. *Analytical Chemistry* 1970, *42* (6), 575-579.
66. Clough, P. N.; Thrush, B. A., Mechanism of chemiluminescent reaction between nitric oxide and ozone. *Transactions of the Faraday Society* 1967, *63* (0), 915-925.
67. Jung, K. H.; Lovinsky-Desir, S.; Yan, B.; Torrone, D.; Lawrence, J.; Jezioro, J. R.; Perzanowski, M.; Perera, F. P.; Chillrud, S. N.; Miller, R. L., Effect of personal exposure to black carbon on

changes in allergic asthma gene methylation measured 5 days later in urban children: importance of allergic sensitization. *Clinical Epigenetics* 2017, *9* (1), 61.
68. Villena, G.; Bejan, I.; Kurtenbach, R.; Wiesen, P.; Kleffmann, J., Interferences of commercial NO2 instruments in the urban atmosphere and in a smog chamber. *Atmosheric Measurement Techniques* 2012, *5* (1), 149-159.
69. Reed, C.; Evans, M. J.; Di Carlo, P.; Lee, J. D.; Carpenter, L. J., Interferences in photolytic NO2 measurements: explanation for an apparent missing oxidant? *Atmospheric Chemistry and Physics* 2016, *16* (7), 4707-4724.
70. Perim de Faria, J.; Bundke, U.; Berg, M.; Freedman, A.; Onasch, T. B.; Petzold, A., Airborne and laboratory studies of an IAGOS instrumentation package containing a modified CAPS particle extinction monitor. *Aerosol Science and Technology* 2017, 1-14.
71. Gao, R. S.; Telg, H.; McLaughlin, R. J.; Ciciora, S. J.; Watts, L. A.; Richardson, M. S.; Schwarz, J. P.; Perring, A. E.; Thornberry, T. D.; Rollins, A. W.; Markovic, M. Z.; Bates, T. S.; Johnson, J. E.; Fahey, D. W., A light-weight, high-sensitivity particle spectrometer for PM2.5 aerosol measurements. *Aerosol Science and Technology* 2016, *50* (1).
72. Kebabian, P. L.; Herndon, S. C.; Freedman, A., Detection of nitrogen dioxide by cavity attenuated phase shift spectroscopy. *Analytical Chemistry* 2005, *77* (2), 724-728.
73. Bundke, U., Draft of DDP_75420_IAGOS-P2e; enviscope GmbH, Forschungszentrum Jülich. 2021.
74. Volz-Thomas, A.; Berg, M.; Heil, T.; Houben, N.; Lerner, A.; null, n., *Atmos. Chem. Phys* 2005, *5* (null), 583.
75. Filges, A.; Gerbig, C.; Chen, H.; Franke, H.; Klaus, C.; Jordan, A., The IAGOS-core greenhouse gas package: a measurement system for continuous airborne observations of CO2, CH4, H2O and CO. *Tellus B: Chemical and Physical Meteorology* 2015, *67* (1), 27989.
76. Myhre, G.; Shindell, D.; Bréon, F.-M.; Collins, W.; Fuglestvedt, J.; Huang, J.; Koch, D.; Lamarque, J.-F.; Lee, D.; Mendoza, B.; Nakajima, T.; Robock, A.; Stephens, G.; Takemura, T.; Zhang, H., Anthropogenic and Natural Radiative Forcing. In *Climate Change 2013: The Physical Science Basis. Contribution of Working Group I to the Fifth Assessment Report of the Intergovernmental Panel on Climate Change*, Stocker, T. F.; Qin, D.; Plattner, G.-K.; Tignor, M.; Allen, S. K.; Boschung, J.; Nauels, A.; Xia, Y.; Bex, V.; Midgley, P. M., Eds. Cambridge University Press: Cambridge, United Kingdom and New York, NY, USA, 2013; pp 659–740.
77. Sandradewi, J.; Prévôt, A. S. H.; Szidat, S.; Perron, N.; Alfarra, M. R.; Lanz, V. A.; Weingartner, E.; Baltensperger, U., Using Aerosol Light Absorption Measurements for the Quantitative Determination of Wood Burning and Traffic Emission Contributions to Particulate Matter. *Environmental Science & Technology* 2008, *42* (9), 3316-3323.
78. Rosen, H.; Hansen, A. D. A.; Gundel, L.; Novakov, T., Identification of the optically absorbing component in urban aerosols. *Appl. Opt.* 1978, *17* (24), 3859-3861.
79. Moosmüller, H.; Chakrabarty, R. K.; Arnott, W. P., Aerosol light absorption and its measurement: A review. *Journal of Quantitative Spectroscopy and Radiative Transfer* 2009, *110* (11), 844-878.
80. Ogren, J.; Wendell, J.; Andrews, E.; Sheridan, P., Continuous light absorption photometer for long-Term studies. *Atmospheric Measurement Techniques* 2017, *10*, 4805-4818.
81. Hansen, A. D. A.; Rosen, H.; Novakov, T., The aethalometer — An instrument for the real-time measurement of optical absorption by aerosol particles. *Science of The Total Environment* 1984, *36*, 191-196.
82. Petzold, A.; Schloesser, H.; Sheridan, P.; Arnott, W.; Ogren, J.; Virkkula, A., Evaluation of Multiangle Absorption Photometry for Measuring Aerosol Light Absorption. *Aerosol Science and Technology* 2005, *39*, 40-51.
83. Collaud Coen, M.; Weingartner, E.; Apituley, A.; Ceburnis, D.; Fierz-Schmidhauser, R.; Flentje, H.; Henzing, J. S.; Jennings, S. G.; Moerman, M.; Petzold, A.; Schmid, O.; Baltensperger,

U., Minimizing light absorption measurement artifacts of the Aethalometer: evaluation of five correction algorithms. *Atmos. Meas. Tech.* 2010, *3* (2), 457-474.
84. Virkkula, A., Correction of the Calibration of the 3-wavelength Particle Soot Absorption Photometer (3 PSAP). *Aerosol Science and Technology* 2010, *44* (8), 706-712.
85. Virkkula, A.; Ahlquist, N. C.; Covert, D. S.; Sheridan, P. J.; Arnott, W. P.; Ogren, J. A., A three-wavelength optical extinction cell for measuring aerosol light extinction and its application to determining light absorption coefficient. *Aerosol Science and Technology* 2005, *39* (1), 52-67.
86. Schnaiter, M.; Schmid, O.; Petzold, A.; Fritzsche, L.; Klein, K. F.; Andreae, M. O.; Helas, G.; Thielmann, A.; Gimmler, M.; Mohler, O.; Linke, C.; Schurath, U., Measurement of wavelength-resolved light absorption by aerosols utilizing a UV-VIS extinction cell. *Aerosol Science and Technology* 2005, *39* (3), 249-260.
87. Perim de Faria, J.; Bundke, U.; Freedman, A.; Onasch, T. B.; Petzold, A., Laboratory validation of a compact single-scattering albedo (SSA) monitor. *Atmos. Meas. Tech.* 2021, *14* (2), 1635-1653.
88. Bodhaine, B. A.; Ahlquist, N. C.; Schnell, R. C., Three-wavelength nephelometer suitable for aircraft measurement of background aerosol scattering coefficient. *Atmospheric Environment. Part A. General Topics* 1991, *25* (10), 2267-2276.
89. Onasch, T. B.; Fortner, E. C.; Trimborn, A. M.; Lambe, A. T.; Tiwari, A. J.; Marr, L. C.; Corbin, J. C.; Mensah, A. A.; Williams, L. R.; Davidovits, P., *Aerosol Sci. Technol.* 2015, *49* (null), 409.
90. Ogren, J. A.; Wendell, J.; Andrews, E.; Sheridan, P. J., Continuous light absorption photometer for long-term studies. *Atmospheric Measurement Techniques* 2017, *10* (12), 4805-4818.
91. Müller, T.; Virkkula, A.; Ogren, J. A., Constrained two-stream algorithm for calculating aerosol light absorption coefficient from the Particle Soot Absorption Photometer. *Atmos. Meas. Tech.* 2014, *7* (12), 4049-4070.
92. Anderson, T. L.; Ogren, J. A., Determining aerosol radiative properties using the TSI 3563 integrating nephelometer. *Aerosol Science and Technology* 1998, *29* (1), 57-69.
93. Massoli, P.; Murphy, D. M.; Lack, D. A.; Baynard, T.; Brock, C. A.; Lovejoy, E. R., Uncertainty in Light Scattering Measurements by TSI Nephelometer: Results from Laboratory Studies and Implications for Ambient Measurements. *Aerosol Science and Technology* 2009, *42* (11), 1064-1074.
94. Liu, B. Y. H.; Pui, D. Y. H., On the performance of the electrical aerosol analyzer. *Journal of Aerosol Science* 1975, *6* (3), 249-264.
95. Bischof, O.; Weber, P.; Bundke, U.; Petzold, A.; Kiendler-Scharr, A., Characterization of the Miniaturized Inverted Flame Burner as a Combustion Source to Generate a Nanoparticle Calibration Aerosol. *Aerosol, Emiss. Control Sci. Technol.* 2020, *6*, 37-46.
96. Kazemimanesh, M.; Moallemi, A.; Thomson, K.; Smallwood, G.; Lobo, P.; Olfert, J., A novel miniature inverted-flame burner for the generation of soot nanoparticles. *Aerosol Science and Technology* 2018.
97. Onasch, T.; Massoli, P.; Kebabian, P.; Hills, F. B.; Bacon, F.; Freedman, A., Single Scattering Albedo Monitor for Airborne Particulates. *Aerosol Science and Technology* 2015, *49*, 267 - 279.
98. Faria, J.; Bundke, U.; Freedman, A.; Onasch, T.; Petzold, A., Laboratory Validation and Field Deployment of a Compact Single-Scattering Albedo (SSA) Monitor. *Atmospheric Measurement Techniques Discussions* 2019, 1-18.
99. Virkkula, A.; Ahlquist, N. C.; Covert, D. S.; Arnott, W. P.; Sheridan, P. J.; Quinn, P. K.; Coffman, D. J., Modification, calibration and a field test of an instrument for measuring light absorption by particles. *Aerosol Science and Technology* 2005, *39* (1), 68-83.
100. Sherman, J. P.; Sheridan, P. J.; Ogren, J. A.; Andrews, E.; Hageman, D.; Schmeisser, L.; Jefferson, A.; Sharma, S., A multi-year study of lower tropospheric aerosol variability and

systematic relationships from four North American regions. *Atmos. Chem. Phys.* 2015, *15* (21), 12487-12517.
101. Török, S.; Malmborg, V. B.; Simonsson, J.; Eriksson, A.; Martinsson, J.; Mannazhi, M.; Pagels, J.; Bengtsson, P.-E., Investigation of the absorption Ångström exponent and its relation to physicochemical properties for mini-CAST soot. *Aerosol Science and Technology* 2018, *52* (7), 757-767.
102. Laj, P.; Bigi, A.; Rose, C.; Andrews, E.; Lund Myhre, C.; Collaud Coen, M.; Lin, Y.; Wiedensohler, A.; Schulz, M.; Ogren, J. A.; Fiebig, M.; Gliß, J.; Mortier, A.; Pandolfi, M.; Petäja, T.; Kim, S. W.; Aas, W.; Putaud, J. P.; Mayol-Bracero, O.; Keywood, M.; Labrador, L.; Aalto, P.; Ahlberg, E.; Alados Arboledas, L.; Alastuey, A.; Andrade, M.; Artíñano, B.; Ausmeel, S.; Arsov, T.; Asmi, E.; Backman, J.; Baltensperger, U.; Bastian, S.; Bath, O.; Beukes, J. P.; Brem, B. T.; Bukowiecki, N.; Conil, S.; Couret, C.; Day, D.; Dayantolis, W.; Degorska, A.; Eleftheriadis, K.; Fetfatzis, P.; Favez, O.; Flentje, H.; Gini, M. I.; Gregorič, A.; Gysel-Beer, M.; Hallar, A. G.; Hand, J.; Hoffer, A.; Hueglin, C.; Hooda, R. K.; Hyvärinen, A.; Kalapov, I.; Kalivitis, N.; Kasper-Giebl, A.; Kim, J. E.; Kouvarakis, G.; Kranjc, I.; Krejci, R.; Kulmala, M.; Labuschagne, C.; Lee, H. J.; Lihavainen, H.; Lin, N. H.; Löschau, G.; Luoma, K.; Marinoni, A.; Martins Dos Santos, S.; Meinhardt, F.; Merkel, M.; Metzger, J. M.; Mihalopoulos, N.; Nguyen, N. A.; Ondracek, J.; Pérez, N.; Perrone, M. R.; Petit, J. E.; Picard, D.; Pichon, J. M.; Pont, V.; Prats, N.; Prenni, A.; Reisen, F.; Romano, S.; Sellegri, K.; Sharma, S.; Schauer, G.; Sheridan, P.; Sherman, J. P.; Schütze, M.; Schwerin, A.; Sohmer, R.; Sorribas, M.; Steinbacher, M.; Sun, J.; Titos, G.; Toczko, B.; Tuch, T.; Tulet, P.; Tunved, P.; Vakkari, V.; Velarde, F.; Velasquez, P.; Villani, P.; Vratolis, S.; Wang, S. H.; Weinhold, K.; Weller, R.; Yela, M.; Yus-Diez, J.; Zdimal, V.; Zieger, P.; Zikova, N., A global analysis of climate-relevant aerosol properties retrieved from the network of Global Atmosphere Watch (GAW) near-surface observatories. *Atmos. Meas. Tech.* 2020, *13* (8), 4353-4392.
103. Lack, D. A.; Cappa, C. D.; Covert, D. S.; Baynard, T.; Massoli, P.; Sierau, B.; Bates, T. S.; Quinn, P. K.; Lovejoy, E. R.; Ravishankara, A. R., Bias in Filter-Based Aerosol Light Absorption Measurements Due to Organic Aerosol Loading: Evidence from Ambient Measurements. *Aerosol Science and Technology* 2008, *42* (12), 1033-1041.
104. Wang, X.; Heald, C. L.; Sedlacek, A. J.; de Sá, S. S.; Martin, S. T.; Alexander, M. L.; Watson, T. B.; Aiken, A. C.; Springston, S. R.; Artaxo, P., Deriving brown carbon from multiwavelength absorption measurements: method and application to AERONET and Aethalometer observations. *Atmos. Chem. Phys.* 2016, *16* (19), 12733-12752.
105. Radney, J. G.; You, R.; Ma, X.; Conny, J. M.; Zachariah, M. R.; Hodges, J. T.; Zangmeister, C. D., Dependence of Soot Optical Properties on Particle Morphology: Measurements and Model Comparisons. *Environmental Science & Technology* 2014, *48* (6), 3169-3176.
106. Asmi, E.; Backman, J.; Servomaa, H.; Virkkula, A.; Gini, M. I.; Eleftheriadis, K.; Müller, T.; Ohata, S.; Kondo, Y.; Hyvärinen, A., Absorption instruments inter-comparison campaign at the Arctic Pallas station. *Atmos. Meas. Tech.* 2021, *14* (8), 5397-5413.
107. Bischof, O. F., *Application-Specific Calibration of Condensation Particle Counters under Low Pressure Conditions*. Verlag des Forschungszentrums Jülich, Energie Umwelt, Band 576,: June 2022.
108. Wiedensohler, A., *J. Aerosol Sci* 1988, *19* (3), 387.
109. Hering, S. V.; Lewis, G. S.; Spielman, S. R.; Eiguren-Fernandez, A., A MAGIC concept for self-sustained, water-based, ultrafine particle counting. *Aerosol Science and Technology* 2019, *53* (1), 63-72.
110. Wiedensohler, A.; Orsini, D.; Covert, D. S.; Coffmann, D.; Cantrell, W.; Havlicek, M.; Brechtel, F. J.; Russell, L. M.; Weber, R. J.; Gras, J.; Hudson, J. G.; Litchy, M., Intercomparison Study of the Size-Dependent Counting Efficiency of 26 Condensation Particle Counters. *Aerosol Science and Technology* 1997, *27* (2), 224-242.

111. Banse, D. F.; Esfeld, K.; Hermann, M.; Sierau, B.; Wiedensohler, A., Particle counting efficiency of the TSI CPC 3762 for different operating parameters. *Journal of Aerosol Science* 2001, *32* (1), 157-161.
112. Lewis, G., MAGIC Optics Detector Principle. 2022.
113. Hering, S. V.; Stolzenburg, M. R.; Quant, F. R.; Oberreit, D. R.; Keady, P. B., A Laminar-Flow, Water-Based Condensation Particle Counter (WCPC). *Aerosol Science and Technology* 2005, *39* (7), 659-672.
114. Petzold, A.; Gysel, M.; Vancassel, X.; Hitzenberger, R.; Puxbaum, H.; Vrochticky, S.; Weingartner, E.; Baltensperger, U.; Mirabel, P., On the effects of organic matter and sulphur-containing compounds on the CCN activation of combustion particles. *Atmos. Chem. Phys.* 2005, *5* (12), 3187-3203.
115. Petzold, A.; Marsh, R.; Johnson, M.; Miller, M.; Sevcenco, Y.; Delhaye, D.; Ibrahim, A.; Williams, P.; Bauer, H.; Crayford, A.; Bachalo, W. D.; Raper, D., Evaluation of methods for measuring particulate matter emissions from gas turbines. *Environmental Science & Technology* 2011, *45* (8), 3562-3568.
116. Hering, S. V.; Spielman, S. R.; Lewis, G. S., Moderated, Water-Based, Condensational Particle Growth in a Laminar Flow. *Aerosol Science and Technology* 2014, *48* (4), 401-408.
117. Sang-Nourpour, N.; Olfert, J. S., Calibration of optical particle counters with an aerodynamic aerosol classifier. *Journal of Aerosol Science* 2019, *138*, 105452.
118. Hermann, M.; Heintzenberg, J.; Wiedensohler, A.; Zahn, A.; Heinrich, G.; Brenninkmeijer, C. A. M., Meridional distributions of aerosol particle number concentrations in the upper troposphere and lower stratosphere obtained by Civil Aircraft for Regular Investigation of the Atmosphere Based on an Instrument Container (CARIBIC) flights. *Journal of Geophysical Research: Atmospheres* 2003, *108* (D3).
119. Hermann, M.; Brenninkmeijer, C. A. M.; Slemr, F.; Heintzenberg, J.; Martinsson, B. G.; Schlager, H.; Van Velthoven, P. F. J.; Wiedensohler, A.; Zahn, A.; Ziereis, H., Submicrometer aerosol particle distributions in the upper troposphere over the mid-latitude North Atlantic—results from the third route of 'CARIBIC'. *Tellus B: Chemical and Physical Meteorology* 2008, *60* (1), 106-117.
120. Zhou, C.; Penner, J. E., *J. Geophys. Res. Atmos* 2014, *119* (19), 11303.
121. Lohmann, U.; Feichter, J., *Atmos. Chem. Phys* 2005, *5* (null), 715.
122. Levin, Z.; Cotton, W. R., *Aerosol Pollution Impact on Precipitation: A Scientific Review*. 2009; Vol. null, p null.
123. Fung, K. M.; Heald, C. L.; Kroll, J. H.; Wang, S.; Jo, D. S.; Gettelman, A.; Lu, Z.; Liu, X.; Zaveri, R. A.; Apel, E. C.; Blake, D. R.; Jimenez, J. L.; Campuzano-Jost, P.; Veres, P. R.; Bates, T. S.; Shilling, J. E.; Zawadowicz, M., Exploring dimethyl sulfide (DMS) oxidation and implications for global aerosol radiative forcing. *Atmos. Chem. Phys.* 2022, *22* (2), 1549-1573.
124. Charlson, R. J.; Lovelock, J. E.; Andreae, M. O.; Warren, S. G., Oceanic phytoplankton, atmospheric sulphur, cloud albedo and climate. *Nature* 1987, *326* (6114), 655-661.
125. Bojinski, S.; Verstraete, M.; Peterson, T. C.; Richter, C.; Simmons, A.; Zemp, M., The Concept of Essential Climate Variables in Support of Climate Research, Applications, and Policy. *Bulletin of the American Meteorological Society* 2014, *95* (9), 1431-1443.
126. Brock, C. A.; Schröder, F.; Kärcher, B.; Petzold, A.; Busen, R.; Fiebig, M., Ultrafine particle size distributions measured in aircraft exhaust plumes. *Journal of Geophysical Research: Atmospheres* 2000, *105* (D21), 26555-26567.
127. Gallar, C.; Brock, C. A.; Jimenez, J. L.; Simons, C., A Variable Supersaturation Condensation Particle Sizer. *Aerosol Science and Technology* 2006, *40* (6), 431-436.
128. Hermann, M.; Wehner, B.; Bischof, O. F.; Han, H.-S.; Krinke, T.; Liu, W. S.; Zerrath, A. F.; Wiedensohler, A., Particle counting efficiencies of new TSI condensation particle counters. *Journal of Aerosol Science* 2007, *38*, 674-682.

129. Mei, F.; Spielman, S.; Hering, S.; Wang, J.; Pekour, M. S.; Lewis, G.; Schmid, B.; Tomlinson, J.; Havlicek, M., Simulation-aided characterization of a versatile water-based condensation particle counter for atmospheric airborne research. *Atmos. Meas. Tech.* 2021, *14* (11), 7329-7340.
130. Magnusson, L.-E.; Koropchak, J.; Anisimov, M.; Poznjakovskiy, V.; Fernandez de la Mora, J., Correlations for Vapor Nucleating Critical Embryo Parameters. *Journal of Physical and Chemical Reference Data* 2003, *32*, 1387-1409.
131. Iida, K.; Stolzenburg, M. R.; McMurry, P. H., Effect of Working Fluid on Sub-2 nm Particle Detection with a Laminar Flow Ultrafine Condensation Particle Counter. *Aerosol Science and Technology* 2009, *43* (1), 81-96.
132. Kupper, M.; Kraft, M.; Boies, A.; Bergmann, A., High-temperature condensation particle counter using a systematically selected dedicated working fluid for automotive applications. *Aerosol Science and Technology* 2020, *54* (4), 381-395.
133. Havemeyer, R. N., Freezing Point Curve of Dimethyl Sulfoxide—Water Solutions. *Journal of Pharmaceutical Sciences* 1966, *55* (8), 851-853.
134. Rumble, J. R., *CRC Handbook of Chemistry and Physics*. 103rd Edition ed.; CRC Press/Taylor & Francis, Boca Raton: Internet Version 2022.
135. Domalski, E. S.; Hearing, E. D., Heat Capacities and Entropies of Organic Compounds in the Condensed Phase. Volume III. *Journal of Physical and Chemical Reference Data* 1996, *25* (1), 1-525.
136. Gutmann, F.; Simmons, L. M., A Theoretical Basis for the Antoine Vapor Pressure Equation. *The Journal of Chemical Physics* 1950, *18* (5), 696-697.
137. Wiedensohler, A.; Wiesner, A.; Weinhold, K.; Birmili, W.; Hermann, M.; Merkel, M.; Müller, T.; Pfeifer, S.; Schmidt, A.; Tuch, T.; Velarde, F.; Quincey, P.; Seeger, S.; Nowak, A., Mobility particle size spectrometers: Calibration procedures and measurement uncertainties. *Aerosol Science and Technology* 2018, *52* (2), 146-164.
138. Tucker, S. P., Development, evaluation and comparison of two independent sampling and analytical methods for ortho-phthalaldehyde vapors and condensation aerosols in air. *Analytical Methods* 2014, *6* (8), 2592-2607.
139. DeMott, P. J.; Mohler, O.; Stetzer, O.; Vali, G.; Levin, Z.; null, n., *Bull. Am. Meteorol. Soc* 2011, *92* (null), 1623.
140. de Laat, A. T. J.; Aben, I.; Deeter, M.; Nédélec, P.; Eskes, H.; Attié, J. L.; Ricaud, P.; Abida, R.; El Amraoui, L.; Landgraf, J., Validation of nine years of MOPITT V5 NIR using MOZAIC/IAGOS measurements: biases and long-term stability. *Atmos. Meas. Tech.* 2014, *7* (11), 3783-3799.
141. Petetin, H.; Sauvage, B.; Parrington, M.; Clark, H.; Fontaine, A.; Athier, G.; Blot, R.; Boulanger, D.; Cousin, J. M.; Nédélec, P.; Thouret, V., The role of biomass burning as derived from the tropospheric CO vertical profiles measured by IAGOS aircraft in 2002–2017. *Atmos. Chem. Phys.* 2018, *18* (23), 17277-17306.
142. Bundke, U., Deliverable 1.4 of the FP7 EU project “Envri Plus". 2015.
143. Perim de Faria, J.; Bundke, U.; Berg, M.; Freedman, A.; Onasch, T. B.; Petzold, A., Airborne and laboratory studies of an IAGOS instrumentation package containing a modified CAPS particle extinction monitor. *Aerosol Science and Technology* 2017, *51* (11), 1240-1253.
144. Oikonomakis, E.; Aksoyoglu, S.; Wild, M.; Ciarelli, G.; Baltensperger, U.; Prévôt, A. S. H., Solar “brightening” impact on summer surface ozone between 1990 and 2010 in Europe – a model sensitivity study of the influence of the aerosol–radiation interactions. *Atmos. Chem. Phys.* 2018, *18* (13), 9741-9765.
145. Püschel, A.; Winzig, W.; Theel, M. Entwicklung der Globalstrahlung 1983-2020 in Deutschland; *Deutscher Wetterdienst*, 2023.

Band / Volume 612
Behavior/performance of tungsten as a wall material for fusion reactors
M. Gago (2023), X, 120 pp
ISBN: 978-3-95806-707-3

Band / Volume 613
Strategieentwicklung zur Umsetzung der Klimaschutzziele im Verkehrssektor mit dem Fokus Kraftstoffe
M. Decker (2023), ix, 243 pp
ISBN: 978-3-95806-714-1

Band / Volume 614
Joining of tungsten and steel for the first wall of a future fusion reactor
V. Ganesh (2023), xxx, 142, a-v pp
ISBN: 978-3-95806-715-8

Band / Volume 615
Polluter group specific emission optimisation for regional air quality analyses using four-dimensional variational data assimilation
P. M. Backes (2023), xxi, 115 pp
ISBN: 978-3-95806-717-2

Band / Volume 616
Effect of organic soil amendments on increasing soil N retention and reducing N losses from agricultural soils
Z. Li (2023), XI, 134 pp
ISBN: 978-3-95806-721-9

Band / Volume 617
Radiolytic Stability of BTBP-, BTPhen- and DGA-based Ligands for the Selective Actinide Separation by Solvent Extraction
H. Schmidt (2023), ca. 200 pp
ISBN: 978-3-95806-723-3

Band / Volume 618
$Na_5YSi_4O_{12}$-type Na^+ superionic conductors for solid-state batteries
A. Yang (2023), X, 150 pp
ISBN: 978-3-95806-731-8

Band / Volume 619
Development of industry-scalable processes for nanocrystalline silicon oxide in silicon heterojunction solar cells
D. Qiu (2023), 202 pp
ISBN: 978-3-95806-734-9

Schriften des Forschungszentrums Jülich
Reihe Energie & Umwelt / Energy & Environment

Band / Volume 620
Photonic Sintering of Garnet-Based Solid-State Batteries
W. S. Scheld (2024), XII, 153 pp
ISBN: 978-3-95806-737-0

Band / Volume 621
Ceria-based composites for application in Oxygen transport membranes
L. Fischer (2024), xiii, 216 pp
ISBN: 978-3-95806-739-4

Band / Volume 622
Investigations of Air Quality Aspects with the Urban Climate Model PALM4U
R. Wegener, U. Javed, R. Dubus, and D. Klemp (2024), 93 pp
ISBN: 978-3-95806-741-7

Band / Volume 623
The Chemical Budget of Radicals and Reaction Mechanisms of the Atmospheric Oxidation of Monoterpenes Investigated in the Atmospheric Simulation Chamber SAPHIR
Y. S. Pang (2024), VI, 158 pp
ISBN: 978-3-95806-742-4

Band / Volume 624
Optimizing spectral electrical impedance tomography technology for improved subsurface characterization
H. Wang (2024), xxix, 113 pp
ISBN: 978-3-95806-744-8

Band / Volume 625
On a multi-spectral method for measuring aerosol properties, suitable for operation on iagos passenger aircraft
P. Weber (2024), ca 123 pp
ISBN: 978-3-95806-746-2

Weitere ***Schriften des Verlags im Forschungszentrum Jülich*** unter
http://wwwzb1.fz-juelich.de/verlagextern1/index.asp

Energie & Umwelt / Energy & Environment
Band / Volume 625
ISBN 978-3-95806-746-2

Mitglied der Helmholtz-Gemeinschaft

JÜLICH
Forschungszentrum